Probing Radiative Thermal Transport at the Nanoscale

by

Bai Song

A dissertation submitted in partial fulfillment
of the requirements for the degree of
Doctor of Philosophy
(Mechanical Engineering)
in the University of Michigan
2015

Doctoral Committee:

Associate Professor Pramod Sangi Reddy, Co-Chair
Professor Edgar Meyhofer, Co-Chair
Associate Professor Vikram Gavini
Professor Roberto Merlin

To my parents.

To Dan and Ziyao.

Acknowledgements

Pierre Curie once wrote that it is necessary to make a dream of life and the dream a reality. In the summer of 2010, after spending seven years in Tsinghua University, Beijing, I quoted these very words as I made my decision to come to the United States. I felt simply into science and wanted to further explore, however, I was leaving behind more than I could readily justify: my parents and sister, my advisor, professors, colleagues and friends who had become so dear to me. It was never an easy decision, and I owe every bit of my achievement to the support of my beloved ones in China. In particular, I am forever indebted to Professor Zeng-Yuan Guo, my master's advisor. Being a highly accomplished scientist in his seventies, Prof. Guo treated me with the utmost kindness, respect and trust. Group and individual Meetings were frequently arranged, in the lab, a café or his simple yet warm home, even when he was not feeling well. Professors Xin-Gang Liang, Xing Zhang and many others were also of great help both in research and in life. Together they readied me for the challenges to come.

Further, I am most grateful to Professors Pramod Reddy and Edgar Meyhofer, who served as my doctoral co-advisors in Michigan and suggested a research topic that I have enjoyed tremendously. With lots of passion and expertise for challenging experiments, they are among the most wonderful scientists I have ever known. Treating me as an equal and a friend, they are also among the dearest. Edgar used to solder circuits with me until 9 PM without having dinner, while Pramod would come to rescue at midnight when I locked myself out of the lab. Together they have been great mentors beyond what I could have wished for, and deserve to share every bit of my future success.

Moreover, my deep gratitude goes to the many collaborators, without whom my research would not have been possible. Specifically, in Michigan, Yashar Ganjeh, Seid Sadat, Dakotah Thompson, Anthoy Fiorino, Kyeongtae Kim, Woochul Lee, Wonho Jeong and Longji Cui contributed significantly to the experiments. Some of them helped develop the platform, others fabricated the microdevices and scanning probes, and the rest performed many of the measurements. Further, in Spain,

Victor Fernandez-Hurtado and Johannes Feist under the supervision of Professors Juan Carlos Cuevas and Francisco J. Garcia-Vidal contributed greatly to the numerical simulations and theoretical analysis. Besides, an open source software (SCUFF-EM) written by M. T. Homer Reid from MIT proved truly helpful. I would also like to thank Pilar Herrera-Fierro and Toby Donajkowski for their respective help with microdevices and machined parts. In addition, my committee members Professors Vikram Gavini and Roberto Merlin have proven kind, sharp and helpful. Their attitude towards research has been inspiring, and their questions were always thought-provoking.

When it comes to personal life, both my advsiors, all my labmates and other friends like Xiaoda Sun and Zupan Hu, deserve my hearty appreciation. Your presence, performance and blessings were most essential to our little wedding, yet in return I had you suffer my lengthy and stupid speech.

At last, my love goes to the family: my parents and sister, and most importantly my wife Dan and my newborn Ziyao. I always say research is one of the few things that matter in life, and I certainly have spent much more time in the lab then with you guys. However, please know that there would be no life without you.

Endless is the road ahead, high and low I shall search. Over the years I have learned much with scientific methods, yet I have learned more from scientists as simple women and men, to whom I am forever grateful. I have never been good at making acknowledgments, and am sorry if I have failed to be thorough and fair. However, I have always kept my promise to work hard and do good research. And it is my wish to repay the debt by trying to be as kind and helpful to others as you all have been to me.

Contents

List of Figures

List of Tables

Abstract

Thermal radiative emission from a hot to a cold surface plays an important role in many applications, including energy conversion, thermal management, lithography, data storage, and thermal microscopy. While thermal radiation at length scales larger than the dominant wavelength is well understood in terms of Planck's law and the Stefan-Boltzmann law, near-field thermal radiation is not. With constantly advancing micro- and nanofabrication techniques and ever smaller devices a substantial need for a better and more reliable understanding of the fundamental physics governing nanoscale radiative heat transfer has arisen. Unfortunately, and in stark contrast to the abundance of theoretical and numerical work, there have only been limited experimental efforts and achievements. The central challenge in the field is to accurately and unambiguously characterize radiative heat transport between well-defined surfaces across nanometer distances.

The key scientific and technological questions that I have experimentally addressed during my doctoral study include: How does radiative heat transfer between an emitter and a receiver depend on their spatial separation (gap size), and does the radiative heat flux increase by over five orders of magnitude as the gap size is reduced to a few nanometers, as theoretically predicted? Can polar dielectric and metallic thin films support substantial near-field heat flow enhancement? For single-digit nanometer gaps, is the widely-used theoretical framework of fluctuational electrodynamics (still) applicable? To address these challenging questions in gap sizes as small as tens of nanometers, we developed a nanopositioning platform to precisely control the gap between a microfabricated emitter device and a suspended receiver/calorimeter device which enables simultaneous measurement of the radiative heat flow across the gap. Further, we employed an atomic force microscope (AFM) in conjunction with stiff custom-fabricated scanning thermal microscopy (SThM) probes to explore the extreme near-field characterized by gaps of a few nanometers. In both approaches, high vacuum, vibration isolation and temperature control are implemented for accurate thermal measurements and for maintaining a stable gap. Finally, we performed state-of-the-art fluctuational electrodynamics-based calculations and analysis to compare theoretical predictions with experimental observations.

Using the nanopositioner-based approach we systematically demonstrated a heat flux enhancement at room temperature over 1000-fold for silica surfaces as the gap size decreases from 10 μm to ~20 nm. Our computational modeling of the spectral heat transfer coefficients revealed that such enhancement is due to the coupling of surface phonon polaritons (SPhPs) supported by the silica surfaces which are polar dielectric. We also showed that 50 nm-thick (~1/200 of the dominant wavelength) silica films can enhance near-field radiative heat transfer nearly as much as bulk silica. From the analysis of the mode shape of the SPhPs, we found that the observed radiative near-field transport characteristic of thin films is a result of the gap size-dependent (comparable) penetration depth of the coupled SPhPs. Further, our near-field measurements between a silica and a gold surface showed a negligible increase of heat flow, highlighting the importance of matching the emission spectra of materials in order to achieve desired nanoscale enhancement. With the AFM-based approach, we were able to probe radiative heat transfer between both dielectric (silica, silicon nitride) and metallic surfaces (gold) in gap sizes as small as 2 nm. We did observe about five orders-of-magnitude heat transfer enhancement, and confirm the validity of macroscopic fluctuational electrodynamics and local dielectric functions for modeling near-field radiative heat transfer even in such extreme near-field. Compared to the polar dielectric surfaces, the enhancement between gold surfaces is due to tunneling of frustrated total internal reflection modes. We believe that the techniques and approaches developed in this dissertation will enable experimental analysis of novel near-field thermal phenomena critical for future technological applications. Moreover, our platforms are readily applicable for probing other interesting phenomena including Casimir forces.

Chapter 1

Overview and Outlook

1.1 Overview

Inquiries into the nature of radiant heat and its governing laws spanned hundreds of years, culminating in 1900 in Planck's law of blackbody radiation which has since proven satisfactory in numerous applications. By definition a blackbody absorbs all incident radiation, thus it must possess the maximum absorptive power. Based on Kirchhoff's argument of a detailed balance between absorption and emission, a blackbody must also represent the highest emissive power. As a result, the idea of a blackbody limit was seldom questioned. Later around 1953, Rytov proposed the theory of fluctuational electrodynamics which relates thermal radiation mathematically to its origin in the fluctuations of electric charges, allowing for the first time exact calculations of heat flow using Maxwell's equations, the fluctuation-dissipation theorems and complex dielectric functions of materials. This groundbreaking theory treats in a unified way both propagating (far-field) and evanescent (near-field) electromagnetic (EM) waves, and both large and small length scales. To date it has inspired and enabled hundreds of theoretical and numerical studies of radiative transfer between closely spaced bodies, where wave interference affects heat flow and contributions from evanescent waves dominate (near-field radiative heat transfer, or NFRHT). One universal prediction concerning NFRHT is that as an emitting body approaches a receiving one, the heat flow will depend on their spatial separation (gap) and eventually become orders-of-magnitude larger than the blackbody limit, even for highly reflective materials like gold. The characteristic length concerning such size effect is the Wien's wavelength, which is 10 μm at 300 K. Consequently, a thorough understanding of the thermal properties of progressively smaller micro/nanofabricated devices requires a better and more reliable understanding of the fundamental physics governing radiative heat transfer at the micro- and nanoscale. Such knowledge cannot be obtained without proper experimental validation/invalidation of theories.

Unfortunately, there have only been limited experimental efforts and achievements, in contrast to the abundance of theoretical and numerical work. The central challenge has been to accurately and unambiguously characterize radiative thermal transport between well-defined objects across nanometer distances.

In this chapter I briefly outline the contents of the entire dissertation, and summarize my experimental efforts over the past five years along with a description of my key achievements and conclusions in the study of radiative heat transfer at the nanoscale. As all the research work described below has been peer-reviewed and published, the individual chapters of my dissertation are adapted from the published manuscripts with minimum changes which were necessary for a consistent format. Note that all these studies are highly interdisciplinary and challenging, and would have not been possible without extensive collaboration. Consequently, I highly recommend that interested readers consult the author contributions listed in each paper and my acknowledgements in the beginning of this dissertation for a better assessment of the contributions of my collaborators to the work.

In chapter 2 [1], we present a detailed introduction to and review of the study of near-field radiative heat transfer over the past six decades. After a short historical account of radiative thermal transport, we summarize the basics of fluctuational electrodynamics, a theoretical framework for the study of radiative heat transfer in terms of thermally excited propagating and evanescent electromagnetic waves. Various approaches to modeling near-field thermal transport are briefly discussed, together with key results and proposals for manipulation and utilization of radiative heat flow. Subsequently, we review the experimental advances in the characterization of both near-field heat flow and energy density, and conclude with remarks on the opportunities and challenges for future explorations of radiative heat transfer at the nanoscale.

Chapter 3 [2] explores the thin film effect on near-field radiative heat transfer. Recent studies on bulk materials have confirmed long-standing theoretical predictions indicating that when the gap between the emitting and receiving surfaces is reduced to tens of nanometers, well below the peak wavelength of the blackbody emission spectrum, the radiative heat flux increases by orders of magnitude. However, despite recent attempts, whether such enhancements can be obtained with nanoscale dielectric films thinner than the penetration depth of thermal radiation, as suggested by theory, remains experimentally unknown. In this chapter, using a novel experimental

platform that leverages picowatt resolution heat-flow calorimetry, we experimentally demonstrate a dramatic increase in radiative heat transfer—comparable to that obtained between bulk materials—even for very thin dielectric films (50 - 100 nm) when the spatial separation between the surfaces is comparable to the film thickness. These results were explained by analyzing the spectral characteristics and the mode shapes of surface phonon polaritons, which dominate near-field radiative heat transport in polar dielectric thin films. We note that in this work microfabricated spherical emitters and planar receivers were used.

Further, in chapter 4 [3] an atomic force microscope (AFM)-based approach is employed, in order to probe radiative thermal transport in the extreme near-field, which is characterized by few-nanometer gap sizes. While experimental advances have enabled elucidation of near-field radiative heat transfer in gaps as small as 20 to 30 nm, quantitative analysis in the extreme near-field (<10 nm) has been greatly limited by experimental challenges. Moreover, first pioneering measurements reported results that differ from theoretical predictions by orders of magnitude. In this chapter, we employ custom-fabricated scanning probes with embedded thermocouples, in conjunction with novel microdevices capable of periodic temperature modulation, to quantitatively examine this crucial disagreement. For our experiments we deposited suitably chosen metal or dielectric layers on the scanning probes and microdevices, enabling direct study of extreme near-field radiation between silica–silica, silicon nitride–silicon nitride and gold–gold surfaces to reveal dramatic, gap size-dependent enhancements of radiative heat transfer. Furthermore, our state–of–the–art calculations of radiative heat transfer, performed within the theoretical framework of fluctuational electrodynamics, are in excellent agreement with our experimental results providing unambiguous evidence that confirms the validity of this theory for modeling radiative heat transfer in the extreme near-field. This work lays the foundations required for the rational design of novel technologies that leverage nanoscale radiative heat transfer.

Finally, chapter 5 [4] describes a custom-built nanopositioning platform that enables the study of nanoscale radiative heat transfer between two parallel planar surfaces. The parallel-plane configuration has been extensively used in the theoretical and numerical investigations of a variety of near-field thermal phenomena which have so far defied experimental observation, due to longstanding challenges including alignment difficulties and surface imperfections. The parallel-plate configuration is also the most technologically relevant since planar surfaces are readily amenable to materials processing and device fabrication. In this chapter, we present on a novel

platform, with an integrated reflected light microscope, that is capable of parallelizing two planar surfaces such that the angular deviation is <6 μrad, while simultaneously allowing control of the gap from 15 μm down to contact with ~0.15 nm resolution. The capabilities of this platform were verified by using two custom-fabricated micro-devices with planar surfaces, 60 × 60 μm^2 each, whose flatness and surface roughness were experimentally quantified. We first parallelized the two micro-devices by using the developed platform in conjunction with a simple optical approach that relies on the shallow depth of field (~2 μm) of a long working distance microscope objective. Subsequently, we experimentally tested the parallelism achieved via the optical alignment procedure by taking advantage of electrodes integrated into the micro-devices. Our measurements unambiguously show that the simple depth-of-field based optical approach enables parallelization such that the angular deviation between the two surfaces is within ~500 μrad. This ensures that the separation between any two corresponding points on the parallel surfaces deviate by ~30 nm or less from the expected value. Further, we show that improved parallelization can be achieved using the integrated micro-electrodes which enable surface roughness limited parallelization with deviations of ~5 nm from parallelism.

1.2 Ongoing Work and Outlook

As an ongoing work, I have been conducting measurements of radiative heat transfer across sub-100 nm vacuum gaps between two parallel planar surfaces, using the custom-built nanopositioner described in Chapter 5 and novel microfabricated planar emitter and receiver devices. We have already observed heat currents about two orders of magnitude larger than the corresponding blackbody limit between silica surfaces. We have also systematically studied NFRHT between combinations of gold, silicon and silica surfaces in similar gaps.

Beyond the set of basic NFRHT questions mentioned above, my next series of inquiries concerns the potential of exotic and engineered materials for NFRHT, and the possibility of fast and high-contrast modulation, rectification and amplification of radiative heat transfer . Being still fundamental in nature, questions under this category are also more application-oriented and experimentally more demanding. Specifically, 1) can materials be micro/nanostructured (perforated, layered, wire arrays, gratings, etc.) or doped to further enhance NFRHT? To what extent can an emission spectrum be tailored to achieve selective broad/narrowband emission with widely tunable threshold/peak? Can we observe extra contribution to NFRHT from magnetic materials? Can

hyperbolic metamaterials enable super-Planckian thermal radiation? 2) Can the NFRHT properties of two-dimensional materials (say graphene) be systematically characterized? Can we perform measurements using phase transition (say metal-insulator transition), nonlinear (say ferroelectric) and active (say chiral) materials? Can external electric or magnetic fields, pulsed or continuous laser beams, and mechanical displacement or stress be introduced to modulate NFRHT? How large/fast can the modulation contrast/rate be? 3) Can near-field thermal rectification be experimentally demonstrated? How large can the contrast be? Can thermal diodes suitable for various working temperatures and gaps be designed and optimized? In addition, can radiative thermal transistors and memory devices be prototyped? Results from such work shall greatly enrich the field of NFRHT, both in the amount of experimental data and in its diversity and depth. In order to explore these questions, extensive effort and expertise are required in the preparation and characterization of a variety of materials and surfaces, and their integration into our microdevices.

Moreover, the work presented in this dissertation highlights a number of potential applications of NFRHT. Of particular interest is the near-field thermophotovoltaic energy conversion technology. A typical thermophotovoltaic (TPV) device features a hot (~1000 K to 2000 K) emitter facing a photovoltaic (PV) cell which converts incident thermal radiation into electricity. First appeared in the late 1950s, TPV devices have been considered for their potential in waste heat recycling from high-temperature industries (glass, metal), in solar energy harvesting, in the cogeneration of heat and power (CHP) and as field and space power sources. The flexibility in fuel selection (fossil, solar, nuclear), high power-density outputs (100 times that of PV), in-phase supply and demand, quietness, portability and reliability render TPV an energy technology of particular advantages. However, despite the growing interest there have only been limited prototypes and products with demonstrated heat-to-power conversion efficiencies below or around 20%. Much remains to be explored and understood, both theoretically and experimentally.

One of the exciting recent efforts to make TPV more efficient seeks to leverage NFRHT by establishing micro/nanometer gaps between the emitter and PV cell (near-field TPV, or NTPV). A basic idea is that in the near-field thermal radiation is enhanced by orders-of-magnitude, leading to a comparably higher output power density. Equally important is the prediction that selective and narrowband emission is achievable with engineered emitters. When paired with PV cells of matching bandgaps, such emitters greatly increase efficiencies (temperature and gap depend-

ent, can be >50%) and reduce waste heat. Theoretical and numerical studies of NTPV began in the 1990s and to date cover the general framework for evaluating power generation performance (efficiency, current density, etc.), the design and processing of high temperature-compatible selective emitters (rare-earth doping, photonic crystals of refractory metals, thin-film thermal wells), and the exploration of suitable low bandgap PV cells (compounds of gallium, antimony, indium and arsenic, graphene-on-silicon).

As promising as NTPV appears, there are great technical difficulties and so far little, if any, description of a working prototype has been reported. All proposals have been based on a parallel-plane configuration with the emitter and PV cell separated by sub-100 nm gaps, considering the relative ease of materials processing and numerical modeling. As a result, all challenges preventing the measurement of NFRHT between parallel-planes have to be first overcome to make possible the experimental characterization of a NTPV device. In light of our recent achievement to this end, we are in a unique position to explore/demonstrate the feasibility of NTPV devices.

Chapter 2

Near-Field Radiative Thermal Transport:

From Theory to Experiment

Reproduced with permission from reference [1]:

Bai Song, Anthony Fiorino, Pramod Reddy and Edgar Meyhofer,

AIP Advances 5, 053503, (2015).

2.1 Abstract

Radiative thermal transport via the fluctuating electromagnetic near-field has recently attracted increasing attention due to its fundamental importance and its impact on a range of applications from data storage to thermal management and energy conversion. After a brief historical account of radiative thermal transport, we summarize the basics of fluctuational electrodynamics, a theoretical framework for the study of radiative heat transfer in terms of thermally excited propagating and evanescent electromagnetic waves. Various approaches to modeling near-field thermal transport are briefly discussed, together with key results and proposals for manipulation and utilization of radiative heat flow. Subsequently, we review the experimental advances in the characterization of both near-field heat flow and energy density. We conclude with remarks on the opportunities and challenges for future explorations of radiative heat transfer at the nanoscale.

2.2 Introduction

Thermal radiation is universal to all objects at non-zero absolute temperatures as electromagnetic radiative emissions necessarily accompany thermally driven random motions of electric charges. Historically, rudimentary yet at times intensive inquiries into the nature of radiant heat

transfer between macroscopic bodies and its governing laws spanned hundreds of years [5]. These efforts were greatly boosted by William Hershel's discovery of the infrared in 1800 [6-8] and ultimately culminated in Max Planck's law of blackbody radiation at the turn of the 20th century [9-11]. Quantum physics largely originated from the efforts of Planck and his contemporaries to better understand experimental results on blackbody radiation [12-14], and in return helped in the establishment of a more general and advanced theory of thermal radiation. The quantum mechanical derivation of various fluctuation-dissipation theorems (FDT) [15-18], and more importantly the formulation of Sergei M. Rytov's fluctuational electrodynamics around the early 1950s [19,20], allowed for the first time direct and detailed mathematical descriptions that related thermal radiation to its origin in the random fluctuations of charges, which represented a significant step beyond discussions of equilibrium distribution of radiation from unspecified sources.

Further, the need for better insulation at cryogenic temperatures [21] and the rapid development of technologies at the micrometer scale created an emerging need to understand thermal radiation in systems with length scales comparable to or smaller than the peak radiation wavelength. In this regime, two effects become important [22-31]: First, the interference of electromagnetic waves causes discernible differences in radiative heat transfer. Second, the evanescent contributions to heat transfer become dominant (Figs. 2-1a, b). The near-field outside an object is a natural extension of the electromagnetic field inside, as demanded by the continuity of field amplitudes across an interface [32]. For evanescent waves, the amplitude of the fields decays exponentially with increasing distance from the interface, however, when the spatial separation between surfaces is small (i.e. they are in the near-field of each other) there is a dramatic increase in energy density and flow due to evanescent contributions [22-31]. The description of near-field radiation requires ideas and concepts that go beyond those required for far-field radiation. In terms of applications, near-field radiative heat transfer (NFRHT) is expected to be key to developing novel technologies such as thermal lithography [22], coherent thermal sources [33-40], scanning thermal microscopy [41-43], heat-assisted magnetic recording [44-46], advanced thermal management and thermal logic devices [47-69], as well as thermophotovoltaic [70-82] and other [83-86] energy conversion devices.

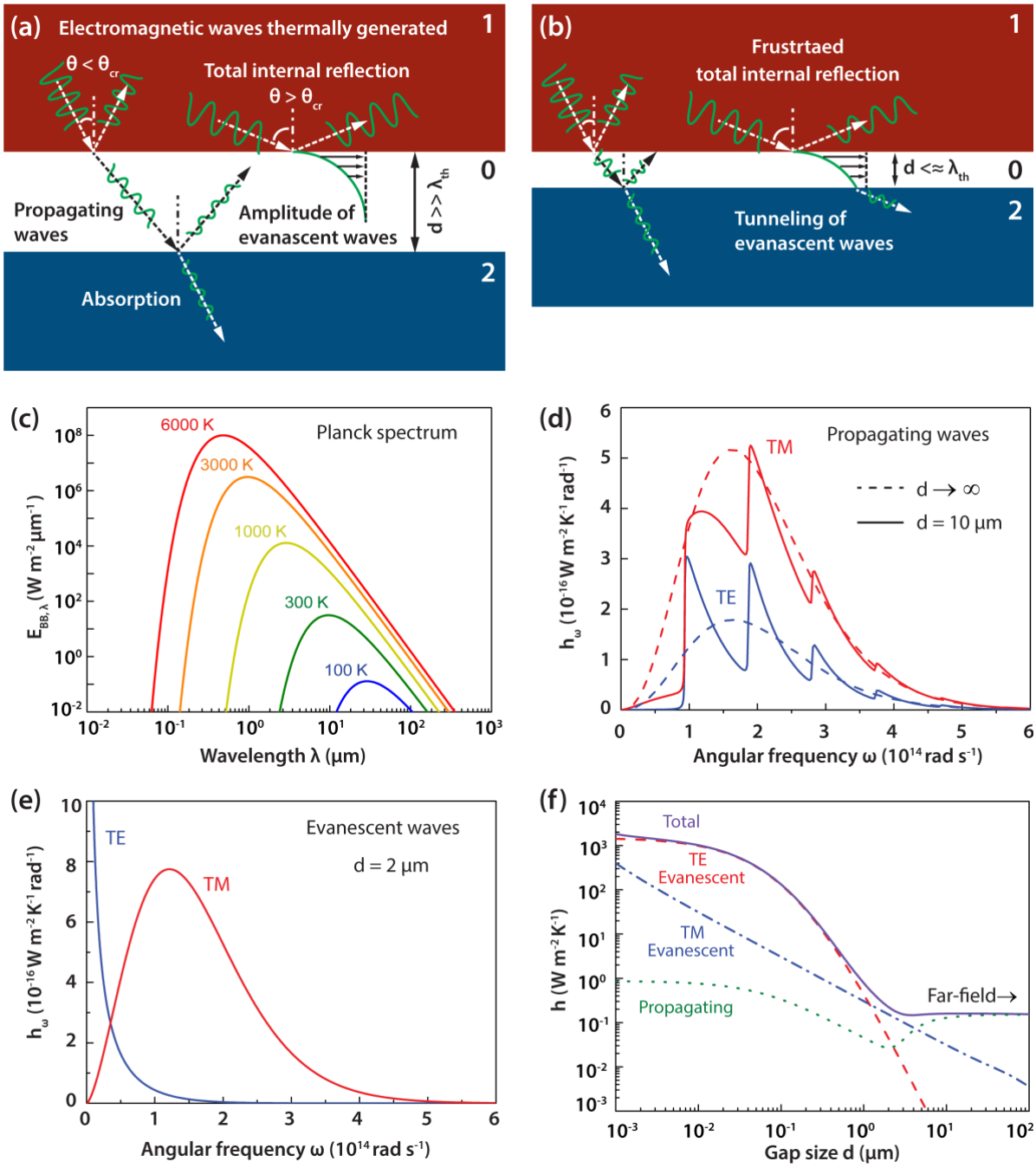

Figure 2-1. Fundamentals of thermal radiation and radiative heat transfer in the far- and near-field. (a) Schematic for far-field radiation between two parallel semi-infinite bodies denoted as "1" and "2", separated by a large vacuum gap denoted by "0". (b) Radiative heat transfer across a vacuum gap comparable to or smaller than the peak thermal wavelength. (c) Blackbody spectral emissive power given by Planck's law. (d) Spectral heat transfer coefficient due to propagating waves calculated for two Cr semi-bodies. (e) Spectral heat transfer coefficient due to evanescent waves. (f) Heat transfer coefficients showing contributions by different modes and polarizations.

In this chapter we begin by providing some historical context (Sec. 2.2). In Sec. 2.4, we briefly summarize the basics of the analytical framework necessary for quantifying NFRHT and describe recent work in theoretical and numerical investigations of NFRHT. In Sec. 2.5 we describe the experimental efforts in probing NFRHT and provide a detailed discussion of various experimental configurations and approaches, including measurements of NFRHT between two parallel plane surfaces, between a scanning probe tip and a plane surface, as well as between a sphere and a plane. Further, we also describe thermal near-field spectroscopy techniques, which give important insights into the local energy density. We conclude in Sec. 2.6 with a brief discussion of the opportunities and challenges in future exploration of radiative heat transfer.

2.3 A Brief History of Radiative Heat Transfer

2.3.1 Planck's law of blackbody radiation

Planck's law of blackbody thermal radiation describes the spectral energy density of electromagnetic radiation $u_{BB,\lambda}(T)$ in a cavity in thermal equilibrium and was first presented by Planck [9] at the German Physical Society meeting in October 1900 as

$$u_{BB,\lambda}(T) = \frac{C_1 \lambda^{-5}}{e^{\frac{C_2}{\lambda T}} - 1}, \tag{2-1}$$

where λ is the free space wavelength, T is the absolute temperature, while C_1 and C_2 denote empirical fitting constants. A large enclosed opaque cavity that features a tiny hole is an excellent practical realization of an all-absorbing blackbody, as light entering the hole is either reflected indefinitely or absorbed in the cavity and is unlikely to re-emerge. Consequently, discussions of blackbody radiation frequently refer to the idea of a cavity. Planck derived the relation given in Eq. (2-1) using his deterministic concept of oscillator entropy, but also considered it "eine glücklich erratene Interpolationsformel", that is, a lucky guessed interpolation. It seamlessly bridges Wien's formula effective at short wavelengths and that of Lord Rayleigh valid only at long wavelengths, and is in excellent agreement with experimental data across the spectrum. Soon afterwards, as a determined effort to go beyond his inspired first guess and reveal more fundamental physics, Planck reluctantly turned to Boltzmann's probabilistic picture of entropy [14]. Only about two months later, in December 1900 and again to the German Physical Society, Planck [10] presented his new derivation and expression:

$$u_{BB,\nu}(T) = \frac{8\pi h_P \nu^3}{c^3} \frac{1}{e^{\frac{h_P \nu}{k_B T}} - 1}, \tag{2-2}$$

where ν is the frequency, and the empirical fitting constants have been superseded by what are now known as three of the most important fundamental physical constants, i.e., the free space speed of light c, the Boltzmann constant k_B and most importantly the constant h_P, which was explicitly introduced for the first time by Planck, with a proposed value of "$6.55\times10^{-27}\,\text{erg}\cdot\text{sec}$". Despite the many and more advanced derivations and interpretations that came about thereafter, Planck's law in the form of Eq. (2-2) has since withstood the test of time. And more profoundly, this seminal work has been widely credited as having initiated the quantum era [12-14].

Planck's law is of fundamental importance to the study of radiative heat transport between many bodies in addition to thermal radiation from isolated objects. It depicts a broadband emission spectrum, which implies temporal incoherence. Also, the spatial coherence of thermal radiation has traditionally been considered poor due to its origin in the random currents distributed throughout the volume of an object. Variations of Eq. (2-2) that express the spectral energy density in terms of wavelength λ or wavenumber η are also used. Apart from the energy density, the closely-related spectral emissive power has been frequently discussed. With respect to the wavelength, the hemispherical spectral emissive power (energy emitted into a half-space per unit time per unit area per unit wavelength at a given wavelength) of a blackbody $E_{BB,\lambda}$ is related to the spectral energy density via $E_{BB,\lambda} = cu_{BB,\lambda}/4$ [13,87], where $u_{BB,\lambda}$ is the wavelength representation of Eq. (2-2). As illustrated in Fig. 2-1c, the Planck spectrum features a maximum spectral emissive power at a temperature-dependent wavelength. One can derive from $E_{BB,\lambda}$ that for any given temperature T, the peak wavelength is given by $\lambda_{BB,\max} \approx 2900/T\,(\mu\text{m})$. This relationship is historically called the Wien's displacement law [87] and at room temperature (300 K), the peak wavelength is about 10 μm. Further, Planck's law naturally leads to the Stefan-Boltzmann law [87] which states that the total emissive power of a blackbody E_{BB} is proportional to T^4, with a proportionality constant σ given by $\sigma = 2\pi^5 k_B^4/15c^2h^3 \approx 5.67\times10^{-8}\,\text{Wm}^{-2}\text{K}^{-4}$. In deriving this equation one simply integrate $E_{BB,\lambda}$ over all wavelengths and show that the total emissive power of a blackbody is indeed $E_{BB} = \sigma T^4$. For a real object the spectral emissive power is usually writ-

ten as $E_\lambda = e_\lambda E_{BB,\lambda}$ where e_λ is its emissivity at a wavelength of λ and $e_\lambda \in [0,1]$. Consequently, the Stefan-Boltzmann law was considered to represent the maximum emissive power (frequently referred to as the blackbody limit) that is possible for any object, at temperature *T*. Also, note that only the object's temperature and material properties are involved, and no dependence on any spatial separation is present. As outlined above the Wien's displacement law and Stefan-Boltzmann law are direct consequences of Planck's law, and together they provide the foundation for far-field radiative heat transfer theories [87,88].

Nevertheless, Planck's law is not without limitations. As pointed out by Planck himself in his book on the Theory of Heat Radiation [11], the spectrum as given by Eq. (2-2) and consequently the Wien's displacement law and Stefan-Boltzmann law, are only valid when all relevant spatial length scales are much larger than the peak wavelengths. The effect of this underlying assumption on thermal radiation seems to have been noted first by Bijl [89] in the context of small cavities at cryogenic temperatures. Specifically, it was highlighted that at very low temperatures, where the characteristic wavelength of thermal radiation becomes comparable to the size of the cavity, classical far-field radiative heat transfer theories would fail to adequately describe heat transfer via radiation. The failure of radiative heat transfer theories at smaller length scales attracted very little attention for many decades, possibly due to lack of theoretical and technical relevance. Indeed, this situation remained true for a good portion of the 20th century, until around the 1950s.

2.3.2 Radiation between closely spaced bodies

One may speculate that the desire and necessity to go beyond Planck's law and to inquire into various size effects in thermal radiation became increasingly tangible on two fronts. Theoretically, progress in the study of proximity forces, especially the closely related Casimir effect (1948) [90], could have inspired similar research on thermal radiation. More importantly, the general framework of fluctuational electrodynamics capable of consistently describing both Casimir effect and thermal radiation was proposed by Rytov [19,20] in 1953, combining Maxwell's equations with the fluctuation-dissipation theorem governing electromagnetic fields. In fact, Rytov even solved an example problem of radiative heat transfer between two closely-spaced parallel plane surfaces, with one being an arbitrary dissipative medium and the other being a mirror of good electrical conductivity. He suggested that the "energy flow density into the mirror"

could increase “without limit” as the spatial separation between the two planes vanishes, due to contribution from the “quasi-stationary field, localized in the layer close to the radiating surface” [19]. This result represents a dramatic deviation from the constant heat flow independent of the separation as predicted by Planck’s (Stefan-Boltzmann) law. However, to the authors’ knowledge, no sequel to this remarkable episode was to be found until the beginning of the 1960s, when the practical need for managing radiative thermal transport across distances comparable to or smaller than the characteristic wavelength appeared.

In 1961, at the AFOSR/ADL Conference on Aerodynamically Heated Structures, A. G. Emslie [21] presented his analysis of radiative heat transfer in the multifoil radiation shields for thermal protection of cryogenic fuels in space. He estimated that at a temperature of 20 K the peak of the Planck radiation distribution corresponds to a wavelength of $\lambda_{BB,\max} = 0.15$ mm, which is of the same order of magnitude as the separation of the foils. The radiation transfer rate between metal foils with constant complex refraction index was predicted to increase with decreasing separation and attains a maximum of over 10 times the large-distance value at a separation of $0.2\lambda_{BB,\max}$ due to constructive interference of propagating waves. For even smaller gaps, however, the heat transfer rate was predicted to reduce to smaller values. Being aware of the evanescent waves, Emslie also noted that “radiation tunneling” could contribute to heat transfer across small gaps, causing further deterioration of the insulation performance of the shields. However, he did not quantitatively estimate the effect of such contribution as he felt that “an exact quantitative analysis of the magnitude of the energy transfer between two metals by the tunneling process is quite difficult to carry out”.

A few years later investigations on radiative thermal transport across small gaps started gaining real momentum, with significant progress made in both theory and experiment. In 1967, Cravalho, Tien and Caren [91], citing Emslie [21], considered wave interference and radiation tunneling between two plane dielectrics of constant real refractive index at cryogenic temperatures. They were able to treat both effects in a unified approach and predicted an increase in heat flow with decreasing gap size as high as an order of magnitude. However, the assumption of lossless and non-dispersive dielectrics renders the work marginally relevant. It should be noted that a similar paper was published by Olivei in 1968, in which the concept of critical angle played a key role [92]. Later in 1970, Boehm and Tien [93] discussed the case of two metals separated by a transparent dielectrics with constant real refractive index, showing that the radiative

heat transfer across small gaps is enhanced by many orders of magnitude, at cryogenic temperatures as well as room temperature. In order to account for nonlocal effects in metals, their use of the anomalous skin effect theory for prediction of the optical properties is noteworthy. Despite yielding many qualitatively sound conclusions, their approach was considered unsatisfactory.

It was not until January 1971 when Polder and Van Hove presented their widely recognized theory of radiative heat transfer between closely spaced bodies [94]. The approach was based on Rytov's fluctuational electrodynamics, but instead of using fluctuating electromagnetic fields in Maxwell's equations as the source terms, they considered the thermally driven fluctuating currents. As a result, the solution was simplified [94]. They focused specifically on the case of two parallel semi-infinite bodies separated by a vacuum gap, where the two bodies are identical with isotropic, nonmagnetic but otherwise arbitrarily dispersive and absorptive properties (Fig. 2-1b). Specifically, radiative heat transfer between two chromium (Cr) half spaces was studied. Contributions to heat transfer across the vacuum gap from both the propagating and evanescent electromagnetic waves, as well as both the transverse electric (TE, or *s*-mode) and transverse magnetic (TM, or *p*-mode) polarizations were consistently considered, with each individual combination (say propagating TE or TM modes) naturally separated from the others (Figs. 2-1d-f). A comparison of the spectrum of radiated power in a small vacuum gap with that in an infinitely large gap clearly demonstrated the effect of constructive and destructive wave interferences (Fig. 2-1d). More importantly, contribution from evanescent TM modes was shown to be dominant for small gaps (Fig. 2-1f). And compared to the constant heat transfer rate given by Planck's law, several orders of magnitude enhancement in heat transfer between two Cr surfaces across nanometer gaps was predicted at room temperature (Fig. 2-1f). Besides, the temperature dependence of various modes contributing to heat flow was analyzed. Note that the general expressions obtained from this work are semi-analytical, in the sense that they are not in a closed-form and involved integrals that require numerical integration.

A few more theoretical papers were published in the following years [18,95-99]. Similar to previous studies these works also focused on the one-dimensional (1D) configuration of two parallel planes separated by a gap (mostly vacuum) due to both the computational ease as well as scope for a clear demonstration of the underlying physics. Of particular interest is a paper published in 1980 by Levin, Polevoi and Rytov [98] in which, expressions for the heat flux were given in terms of generalized surface impedance tensors, in principle covering anisotropic media

with spatial dispersions. Again, a dramatic increase in heat transfer was predicted for small gaps. Please see Hargreaves [100] and Levin *et al.* [98] for detailed comments on these early studies.

Accompanying the early theoretical endeavors around the 1970s were a few carefully designed experiments [100-105]. Utilizing the parallel-plane configuration, all of which demonstrated a definitive dependence of radiative heat transfer on the spatial separations between emitting and receiving bodies from cryogenic to room temperatures, observing mostly few-fold enhancement of heat transfer at small gaps within the micrometer range. A detailed discussion is given in Sec. 2.5.

Relatively few publications are found through the 1980s and 1990s concerning near-field thermal radiation. However, inspired and powered by the ever advancing micro- and nanotechnologies, the dawn of this century has witnessed a rekindled interest, featuring exciting diversity in theoretical and numerical studies as well as unprecedented precision in experimental investigations, which comprise the topics of Sec. 2.4 and Sec. 2.5, respectively.

2.4 Analytical and Numerical Methods

Central to most modern studies of thermal radiation is the intuitive picture of thermally driven fluctuating electromagnetic currents and fields. According to the fluctuation-dissipation theorem (FDT) of Callen and Welton [15], the correlation between random temperature-driven electrical currents is directly related to the dielectric properties of a medium. When the macroscopic Maxwell's equations are solved with the random currents as sources (modeled using the FDT), the thermally excited energy flux (energy flow per unit time per unit area) is obtained from the ensemble-averaged Poynting vector. This basic framework for computing NFRHT is called the fluctuational electrodynamics (FE) formalism [19,20]. Since heat transfer occurs between bodies at different temperatures, a key assumption of FE is that the current fluctuations are solely characterized by the FDT at the corresponding local thermodynamic temperature, and are independent of the incident radiation from the other objects. Several widely available books and reviews [23-31,106-110] describe the theoretical approaches and numerical methods based on FE that are used to study NFRHT, therefore here we provide only a concise summary. However, before we begin, it should be noted that theoretical considerations other than the FE formalism have also been proposed [111-113].

2.4.1 Green function formalism

As an analytical method, the Green function (GF) formalism has distinct advantages and limitations. Expectedly, it has been used almost exclusively for highly symmetric configurations involving infinite planes, dipoles, spheres and cylinders. Whenever applicable, it yields semi-analytical or even closed-from exact solutions, where the contributions from different electromagnetic modes are naturally separated. Further, the GF formalism is amenable to parametric analysis and optimization can be readily applied, allowing opportunities for gaining physical insights. A brief outline of this method is given below, following the existing rich publications.

A. Governing equations and problem solving procedure

Let us consider a system comprising of only two separated bodies, as illustrated in Fig. 2-2. Assuming a time convention of $e^{-i\omega t}$, the frequency domain macroscopic Maxwell's equations [114,115] with random currents as the source [94] of thermal radiation can be written as

$$\nabla \times \mathbf{E}(\mathbf{r},\omega) = i\omega \mathbf{B}(\mathbf{r},\omega), \tag{2-3.1}$$

$$\nabla \times \mathbf{H}(\mathbf{r},\omega) = -i\omega \mathbf{D}(\mathbf{r},\omega) + \mathbf{J}(\mathbf{r},\omega). \tag{2-3.2}$$

Here, **E** and **B** are the complex electric and magnetic field vectors, **r** is the position vector and ω is the angular frequency, **D** and **H** are the electric displacement and magnetic induction, respectively, and are related to **E** and **H** via constitutive relations. For example, in isotropic media $\mathbf{D} = \varepsilon_0 \varepsilon \mathbf{E}$ and $\mathbf{B} = \mu_0 \mu \mathbf{H}$, where ε_0 and μ_0 are the vacuum permittivity and permeability, $\varepsilon(\omega) = \varepsilon'(\omega) + i\varepsilon''(\omega)$ is the frequency-dependent complex dielectric function (relative permittivity) and $\mu(\omega) = \mu'(\omega) + i\mu''(\omega)$ is the relative permeability. All the fields above and below are functions of ω unless otherwise stated. Note that we do not explicitly incorporate any random magnetic current term in the curl equation for the electric field. For more general expressions please see Refs. [109,116,117]. We also assume non-magnetic materials with μ = 1. Equation (2-3) leads to the following vector Helmholtz equations governing the electromagnetic waves:

$$\nabla \times \nabla \times \mathbf{E}(\mathbf{r},\omega) - \varepsilon(\omega)\left(\frac{\omega}{c}\right)^2 \mathbf{E}(\mathbf{r},\omega) = i\omega\mu_0 \mathbf{J}(\mathbf{r},\omega), \tag{2-4.1}$$

$$\nabla\times\nabla\times\mathbf{H}(\mathbf{r},\omega)-\varepsilon(\omega)\left(\frac{\omega}{c}\right)^2\mathbf{H}(\mathbf{r},\omega)=\nabla\times\mathbf{J}(\mathbf{r},\omega). \tag{2-4.2}$$

In practice only one of the two equations needs solved given the relation $\nabla\times\mathbf{E}(\mathbf{r},\omega)=i\omega\mu_0\mathbf{H}(\mathbf{r},\omega)$.

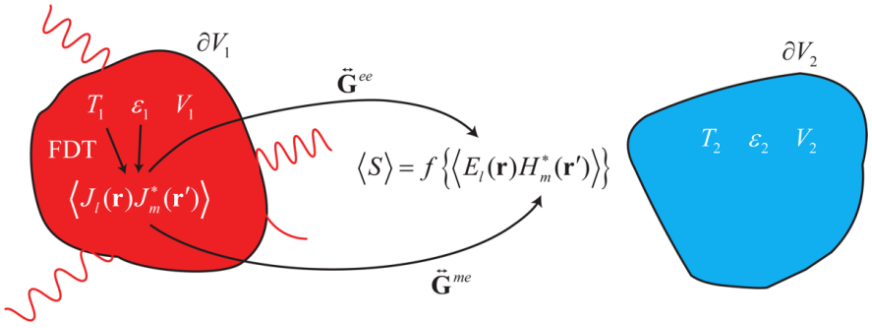

Figure 2-2. Schematic of radiative heat transfer in a two-body system in vacuum. The bodies have uniform temperatures T_1 and T_2 throughout their volumes V_1 and V_2. The material properties are described by the frequency dependent complex dielectric functions ε_1 and ε_2. Electromagnetic fields **E** and **H** are generated by the random currents **J** in the bodies due to their non-vanishing correlations given by the FDT. The field correlations are related to the current correlations via the corresponding Green's dyads, and a linear combination of them yields the Poynting vector, which gives the heat current of interest.

The free electric currents **J** are associated with fluctuating charges in the medium of interest and satisfy the statistical correlation function below given by the fluctuation-dissipation theorem [15]:

$$\left\langle J_l(\mathbf{r},\omega)J_m^*(\mathbf{r}',\omega)\right\rangle=\frac{4}{\pi}\varepsilon_0\varepsilon''(\omega)\omega\Theta_0(\omega,T)\delta_{lm}\delta(\mathbf{r}-\mathbf{r}'), \tag{2-5}$$

where

$$\Theta_0(\omega,T)=\hbar\omega\left(\frac{1}{2}+\frac{1}{e^{\hbar\omega/k_BT}-1}\right) \tag{2-6}$$

is the mean energy of a harmonic oscillator including the zero point contribution; $\hbar=h_P/2\pi$ is the reduced Planck constant; T is the absolute temperature and the superscript * denotes the complex conjugate. The Kronecker delta δ_{lm} indicates no cross coupling between currents in orthogonal directions represented by the subscripts l and m, while the Dirac delta $\delta(\mathbf{r}-\mathbf{r}')$ reflects the assumption of locality, excluding spatial dispersions in the media. Note that a factor of 4 is

included in Eq. (2-5) so only positive frequencies are considered subsequently [26,28,29,110]. Other variations of Eq. (2-5) with differences only in the constant have also been used in existing literatures [24,25,109].

When combined with the proper boundary conditions of a given problem, Eqs. (2-3)-(2-6) allow for calculation of the spectral radiative heat flux as the ensemble-averaged Poynting vector $\left\langle \mathbf{S}\left(\mathbf{r},\omega\right)\right\rangle = \mathrm{Re}\left\langle \mathbf{E}\times\mathbf{H}^{*}\right\rangle /2$. It can be expressed in terms of the known $\left\langle J_l\left(\mathbf{r},\omega\right)J_m^{*}\left(\mathbf{r}',\omega\right)\right\rangle$ by using the dyadic Green functions (also referred to as Green dyads) [118] $\ddot{\mathbf{G}}^{ee}\left(\mathbf{r},\mathbf{r}',\omega\right)$ and $\ddot{\mathbf{G}}^{he}\left(\mathbf{r},\mathbf{r}',\omega\right)$ via the relations [24]

$$\mathbf{E}\left(\mathbf{r},\omega\right) = i\omega\mu_0\int_V d\mathbf{r}'\ddot{\mathbf{G}}^{ee}\left(\mathbf{r},\mathbf{r}',\omega\right)\cdot\mathbf{J}\left(\mathbf{r}',\omega\right), \tag{2-7.1}$$

$$\mathbf{H}\left(\mathbf{r},\omega\right) = \int_V d\mathbf{r}'\ddot{\mathbf{G}}^{me}\left(\mathbf{r},\mathbf{r}',\omega\right)\cdot\mathbf{J}\left(\mathbf{r}',\omega\right). \tag{2-7.2}$$

Key to this approach is then finding analytically the dyadic Green functions which satisfy the wave equations below with Dirac delta sources for a given configuration:

$$\nabla\times\nabla\times\ddot{\mathbf{G}}^{ee}\left(\mathbf{r},\mathbf{r}',\omega\right) - \varepsilon\left(\omega\right)\left(\frac{\omega}{c}\right)^2\ddot{\mathbf{G}}^{ee}\left(\mathbf{r},\mathbf{r}',\omega\right) = \ddot{\mathbf{I}}\delta\left(\mathbf{r}-\mathbf{r}'\right), \tag{2-8.1}$$

$$\nabla\times\nabla\times\ddot{\mathbf{G}}^{me}\left(\mathbf{r},\mathbf{r}',\omega\right) - \varepsilon\left(\omega\right)\left(\frac{\omega}{c}\right)^2\ddot{\mathbf{G}}^{me}\left(\mathbf{r},\mathbf{r}',\omega\right) = \nabla\times\left[\ddot{\mathbf{I}}\delta\left(\mathbf{r}-\mathbf{r}'\right)\right], \tag{2-8.2}$$

where $\ddot{\mathbf{I}}$ is the identity dyad. Similar to Eq. (2-4), only one of the two equations needs solved. Note that the Green dyads for many of the aforementioned simple geometries have long been obtained in the electromagnetism community and can be readily used [118,119]. Below we give the expression of the field correlations in terms of the current correlations and the Green dyads as [24]

$$\left\langle E_i\left(\mathbf{r},\omega\right)H_j^{*}\left(\mathbf{r}',\omega\right)\right\rangle = i\omega\mu_0\left\langle\int_V d\mathbf{r}'G_{il}^{ee}\left(\mathbf{r},\mathbf{r}',\omega\right)G_{jm}^{me*}\left(\mathbf{r},\mathbf{r}'',\omega\right)\int_V d\mathbf{r}''J_l\left(\mathbf{r}',\omega\right)J_m^{*}\left(\mathbf{r}'',\omega\right)\right\rangle, \tag{2-9}$$

where the subscripts *i* and *j* denote spatial directions. Using Eq. (2-5) and the Delta functions therein, Eq. (2-9) can be further written as [24]

$$\left\langle E_i(\mathbf{r},\omega)H_j^*(\mathbf{r}',\omega)\right\rangle = i\frac{4\varepsilon''(\omega)\omega^2}{\pi c^2}\Theta_0(\omega,T)\int_V d\mathbf{r}' G_{il}^{ee}(\mathbf{r},\mathbf{r}',\omega)G_{jl}^{me*}(\mathbf{r},\mathbf{r}',\omega). \tag{2-10}$$

Here the equality $\varepsilon_0\mu_0 c^2 = 1$ has been used. Since the spectral heat flux $\langle \mathbf{S}(\mathbf{r},\omega)\rangle$ is a linear combination of these field correlations, the radiative heat flux can be readily obtained. An integral of $\langle \mathbf{S}(\mathbf{r},\omega)\rangle$ with respect to the angular frequency yields the total heat flux $\langle \mathbf{S}(\mathbf{r})\rangle$; and integration of the normal component of $\langle \mathbf{S}(\mathbf{r})\rangle$ over the entire surface of the object of interest gives the net heat current (energy flow per unit time).

B. Thermal radiation in parallel-plane systems

Based on the concepts and the general procedure outlined above, thermal emission of isolated bodies as well as radiative thermal transport between different objects can be described. We now present as an example the solution of radiative heat transfer between two parallel semi-infinite bodies separated by a vacuum gap (Figs.2-1a, b), making use of the well-known Green function for this geometry [24,119]. Due to its simplicity, the parallel-plane configuration became one of the first NFRHT problems analytically solved. The study of such parallel configurations has since allowed numerous physical insights to be obtained. Written in a Landauer-type expression, the total heat flux across a vacuum gap *d* is given by

$$q(T_1,T_2,d) = \int_0^\infty \frac{d\omega}{4\pi^2}\left[\Theta(\omega,T_1)-\Theta(\omega,T_2)\right]\int_0^\infty dk k\left[\tau_s(\omega,k)+\tau_p(\omega,k)\right], \tag{2-11}$$

where $\Theta(\omega,T) \equiv \hbar\omega/[\exp(\hbar\omega/k_B T)-1]$ is the mean energy of a harmonic oscillator less the zero point contribution; T_i are the absolute temperatures, with subscripts 1 and 2 denoting the emitter and receiver, respectively; the vacuum gap is denoted with subscript 0; *k* is the wave vector component parallel to the planar surfaces, and τ_s and τ_p are the transmission probabilities for the TE and TM modes, respectively. These probabilities can be expressed in terms of the Fresnel coefficients of the interfaces as follows [120],

$$\tau^{12}_{\alpha=s,p}(\omega,k)=\begin{cases}\dfrac{(1-\left|r_\alpha^{01}\right|^2)(1-\left|r_\alpha^{02}\right|^2)}{\left|D_\alpha\right|^2}, & \text{if } k<\omega/c, \text{ propagating waves}\\ \dfrac{4\,\mathrm{Im}\left(r_\alpha^{01}\right)\mathrm{Im}\left(r_\alpha^{02}\right)e^{-2\,\mathrm{Im}(\zeta_2)d}}{\left|D_\alpha\right|^2}, & \text{if } k>\omega/c, \text{ evanascent waves}\end{cases} \tag{2-12}$$

In Eq. (2-12), r_α^{ij} are the Fresnel reflection coefficients at the interfaces between vacuum and the two half spaces, and are given by $r_s^{ij}=\left(\zeta_i-\zeta_j\right)\Big/\left(\zeta_i+\zeta_j\right)$ and $r_p^{ij}=\left(\varepsilon_j\zeta_i-\varepsilon_i\zeta_j\right)\Big/\left(\varepsilon_j\zeta_i+\varepsilon_i\zeta_j\right)$, where $\zeta_i=\sqrt{\varepsilon_i(\omega)\omega^2/c^2-k^2}$ is the transverse component (perpendicular to the planes) of the wave vector in layer i and $\varepsilon_i(\omega)$ is the corresponding frequency-dependent complex dielectric function. $D_\alpha=1-r_\alpha^{01}r_\alpha^{02}e^{2i\zeta_2 d}$ is the Fabre-Pérot-like denominator.

As useful as Eqs. (2-11) and (2-12) are, they have been derived only to calculate radiative heat flux between half spaces (or thick objects in practice) and are not adequate to describe systems featuring thin films and layers which are of significant technical importance. When the emitter and/or receiver are not semi-infinite, but instead are multilayer systems (including thin films) with internal interfaces and finite thicknesses, a direct calculation of the radiative heat flux proves difficult as many emission sources (the layers) and/or multiple reflections at interfaces have to be properly accounted for. Alternatively, one can focus instead only on the field inside the vacuum gap and obtain formally the same expression as given in Eq. (2-11), only that Eq. (2-12) is now replaced with the one below [109,121]:

$$\tau^{12}_{\alpha=s,p}(\omega,k)=\begin{cases}\dfrac{(1-\left|R_\alpha^{1}\right|^2)(1-\left|R_\alpha^{2}\right|^2)}{\left|D_\alpha\right|^2}, & \text{if } k<\omega/c, \text{ propagating waves}\\ \dfrac{4\,\mathrm{Im}\left(R_\alpha^{1}\right)\mathrm{Im}\left(R_\alpha^{2}\right)e^{-2\,\mathrm{Im}(\zeta_2)d}}{\left|D_\alpha\right|^2}, & \text{if } k>\omega/c, \text{ evanascent waves}\end{cases} \tag{2-13}$$

where the Fresnel coefficients r_α^{ij} are replaced by R_α^i, which are the total reflection coefficients of the multilayer systems as seen from inside the vacuum gap, and can be calculated using textbook [115] procedures from all the interface Fresnel coefficients. In the case of half spaces R_α^i reduce to the vacuum interface Fresnel coefficients, thus reproducing Eq. (2-12).

In order to present results in a form that enables direct comparisons with experiments performed under a small temperature differential, the linear thermal conductance (heat current per unit temperature difference) or heat transfer coefficient (thermal conductance per unit area, h) at a mean temperature T can be obtained from:

$$\begin{aligned} h(T,d) &\equiv \lim_{(T_1-T_2)\to 0}\left|\frac{q(T_1,T_2,d)}{T_1-T_2}\right| = \int_0^\infty \frac{d\omega}{4\pi^2}\frac{\partial\Theta(\omega,T)}{\partial T}\int_0^\infty dk k\left[\tau_s(\omega,k)+\tau_p(\omega,k)\right] \\ &\equiv \int_0^\infty d\omega h_\omega(T,d), \end{aligned} \tag{2-14}$$

where the spectral heat transfer coefficient h_ω is also introduced.

The planar configuration as solved above using the GF formalism has proven suitable for analyzing a wide variety of media [49,50,94,98,99,109,116,117,120-173]. Equations (2-11)-(2-14) can even be readily used for structured and composite materials with their dielectric responses modeled using the effective medium theories (EMT) [23]. These are covered in greater detail in Sec. 2.5.3. Apart from computing NFRHT between parallel planes, the GF formalism has also been used for a range of other basic configurations including dipole-plane, dipole-dipole, sphere-sphere, sphere-plane and cylinder-cylinder [22,131,174-184].

In addition to the radiative heat flux and thermal conductance, a few other physical quantities essential for the description of the thermal near-field have been discussed. These include the electromagnetic energy density and the closely-related local density of states (LDOS), the spatial and temporal coherence lengths of thermal radiation, as well as the energy flow path and the penetration depth [33-40,185-195]. All of them can be characterized using the electromagnetic dyadic Green functions, and show strong distance-dependence due to the dominant contributions from evanescent waves in the vicinity of surfaces. Further, some thermodynamic analyses of near-field radiative transport have been performed [196-199]. Expressions of entropy density and entropy flux accompanying near-field thermal radiation were proposed; and implications to the thermodynamic limit of energy conversion efficiencies in the near-field were discussed. We do not discuss these ideas in great detail here as they would take us too far from the focus of this review. However, select results will be briefly introduced in Sec. 2.4.3 and Sec. 2.5.3.

2.4.2 Numerical methods

Although the GF formalism is very useful for studying simple geometries and for obtaining insight into the relevant physical mechanisms it cannot be fruitfully used for exploring NFRHT in complicated geometries. The increasing need to go beyond basic geometries, due to rapid developments in the fabrication of nanoscale devices, has led to the establishment of several numerical approaches. To this end, approximation schemes such as the so-called Derjaguin approximation method were initially used to approximate simple curved surfaces with a set of planes, closely mirroring a similar approach that was developed for studying near-field forces [200]. Although accurate in certain cases, its general validity is questionable and hence should be used with caution [184,201]. For geometries with well-defined periodicities, the semi-analytical method of rigorous coupled-wave analysis has at times been used [30,202].

Most importantly, in light of the above discussions on fluctuational electrodynamics and the GF formalism, it can be seen that the process of radiative heat transfer between various bodies reduces to a consideration of electromagnetic wave scattering problems. Consequently, it is to be expected that existing electromagnetic methodologies could in principle be adapted for NFRHT calculations [203]. Indeed, benefiting from decades of progress in computational classical electrodynamics, the past few years have seen the establishment of quite a few numerical formalisms, many of which are capable of calculating radiative heat transfer between bodies of arbitrary shapes and materials across a range of physically meaningful separations. These formalisms include the scattering matrix approach [106,107,110,201,204-211], the fluctuating surface current formulation [108,110,212,213], the finite difference time domain approach [110,213-217], the Wiener chaos expansion method [218,219] and the thermal discrete-dipole approximation [220]. Although concerned with the same physical problem, these methods differ in how the analysis is conceptually and mathematically formulated. Since significant trade-offs are associated with each of these techniques in terms of the generality, simplicity and efficiency it is not clear if any one technique is superior to others in all circumstances [203]. Therefore, without delving into too many mathematical details, we summarize the ideas underpinning each method, together with the key features and representative results.

A. Derjaguin approximation

In order to handle problems that were not amenable to direct calculations early researchers devised relatively simple procedures to obtain approximate solutions for complex geometries using known solutions for simpler configurations. One such procedure is the Derjaguin approximation (DA) scheme [221,222], which allows calculation of the radiative thermal conductance between simple curved surfaces via solutions of a corresponding parallel-plane system. Examples of problems that were analyzed using this approach include NFRHT between spheres [184] and between a sphere and a plane [221,222], both of which are challenging to analyze using the Green function formalism especially at small gap sizes due to slow numerical convergence. The basic idea of the DA approach can be described by considering how it is used for understanding NFRHT between a sphere and a plane. In this problem the curved surface is approximated by a set of annuli all parallel to the planar system with different gap sizes, and the sphere-plane thermal conductance is calculated as the sum of contributions between individual annulus and the planar surface. Specifically, the sphere-plane conductance is given by

$$G(T,d) = \int_0^R 2\pi r h(T, \bar{d}(r)) dr, \tag{2-15}$$

where R is the radius of the sphere, h is the linear heat transfer coefficient between the planar multilayer systems given by Eq. (2-14), and $\bar{d}(r) = d + R - \sqrt{R^2 - r^2}$ is the local distance between the plane and the annulus with a radius of r.

It has been suggested [184] that to get the correct near-field thermal conductance using this approximation, the far-field contribution has to be accounted for systematically via distance-dependent view factors considered when needed. Although limited in its capacity the DA approach provides the simplest recipe for approximately obtaining the near-field thermal conductance in complicated geometries.

B. Scattering matrix approach

The scattering matrix formalism is arguably the most general method available for calculating both Casimir force and radiative heat transfer between many bodies of arbitrary shapes, materials, temperatures and separations [106,107,110,201,205-211]. As demonstrated by Krüger and coworkers [107], the thermal radiation of an isolated body as well as radiative heat currents between bodies at different temperatures can be written in compact, basis-independent trace formulas that depend on both the scattering operators ($\hat{\mathbf{T}}$) of individual objects and the operator

form ($\hat{\mathbf{G}}_0$) of the free space Green function [118]. The $\hat{\mathbf{T}}$ operator of an object completely characterizes its scattering behavior, encoding in it both the geometric and physical properties of the object. It can be derived by use of the Lippmann-Schwinger equation, and is related to the corresponding dyadic Green function by $\hat{\mathbf{G}} = \hat{\mathbf{G}}_0 + \hat{\mathbf{G}}_0\hat{\mathbf{T}}\hat{\mathbf{G}}_0$ [107,206]. One notable feature of the scattering approach is how it naturally tracks the radiation from each body and its scatterings by the other object, i.e. it is possible to identify how much of the heat flow into one object is contributed by another object of interest [107]. Further, the spatial distribution of the heat flux on the bodies can also be resolved [209]. Moreover, radiation from the environment, which is absent in the GF formalism, can be explicitly included by defining a characteristic temperature [106,107,207,208], and were shown to affect the radiative heat transfer between two bodies via propagating waves [106].

Written in an abstract operator form, the radiation from a single body is given by [107]

$$Q(T) = \frac{2}{\pi}\int_0^\infty d\omega\Theta(\omega,T)\mathrm{Tr}\left\{\mathrm{Im}[\hat{\mathbf{G}}_0]\mathrm{Im}[\hat{\mathbf{T}}] - \mathrm{Im}[\hat{\mathbf{G}}_0]\mathrm{Im}[\hat{\mathbf{T}}]\mathrm{Im}[\hat{\mathbf{G}}_0]\mathrm{Im}[\hat{\mathbf{T}}^*]\right\}, \tag{2-16}$$

where Tr denotes the trace operation. It follows immediately from Eq. (2-16) that thermal radiation from an object is always positive (positivity of thermal radiation). In a two-body system with the environment neglected as usual, the radiative heat current from the first body to the second, $Q_1^2(T)$, is given by [107]

$$Q_1^2(T_1) = \frac{2}{\pi}\int_0^\infty d\omega\Theta(\omega,T_1)\mathrm{Tr}\left\{\begin{array}{l}\left[\mathrm{Im}[\hat{\mathbf{T}}_2] - \hat{\mathbf{T}}_2^*\,\mathrm{Im}[\hat{\mathbf{G}}_0]\hat{\mathbf{T}}_2\right]\dfrac{1}{1-\hat{\mathbf{G}}_0\hat{\mathbf{T}}_1\hat{\mathbf{G}}_0\hat{\mathbf{T}}_2}\cdot \\ \hat{\mathbf{G}}_0\left[\mathrm{Im}[\hat{\mathbf{T}}_1] - \hat{\mathbf{T}}_1^*\,\mathrm{Im}[\hat{\mathbf{G}}_0]\hat{\mathbf{T}}_1^*\right]\hat{\mathbf{G}}_0^*\dfrac{1}{1-\hat{\mathbf{T}}_2^*\hat{\mathbf{G}}_0^*\hat{\mathbf{T}}_1^*\hat{\mathbf{G}}_0^*}\end{array}\right\}. \tag{2-17}$$

When the two bodies are at the same temperature, one expects the net heat flow $Q_{12} = Q_1^2(T) - Q_2^1(T)$ to be 0. This symmetry (reciprocity) of heat transfer can be formally proved using Eq. (2-17) and naturally yields the expression of $Q_2^1(T_2)$. It can further be demonstrated that Eq. (2-17) satisfies the second law of thermodynamics, i.e., that heat is always transferred from a hotter to a colder body [107].

In order to actually compute with Eq. (2-16) or Eq. (2-17), one needs the **T**-matrices, which are the matrix representations of the scattering operators. To this end, one can either choose the partial-wave bases (also called spectral bases) appropriate for the individual objects, or one could calculate the **T**-matrix of each object in other bases using a suitable numerical technique. It should be noted that this calculation only needs to be done once for a given object. Application of the partial-wave expansion approach requires the objects to be properly arranged so each individual can be separated by some high-symmetry shapes, for example, with planes and spheres if a plane wave basis or a spherical basis is desired [107]. When applicable, a spectral basis in general results in faster numerical convergence. And for systems with high symmetry, such as the parallel-plane or the sphere-sphere configuration, the scattering matrix approach can lead to semi-analytical formulas like the ones obtained using the Green function formalism, which also offers a way to check the validity of the scattering matrix approach.

Apart from these general features and results, we note that the numerically exact solution of NFRHT between a sphere and an infinite plane was first performed using the scattering matrix approach [201]. Also, radiative heat transfer between a finite-sized cone and a semi-infinite plane was studied using the scattering matrix formalism [209]. with scattering of the cone treated with the boundary element method (BEM) while the scattering matrix of the plate analytically given. Being the first time a sharp object was studied, it was found that, counterintuitively, the spatial distribution of heat transfer rate exhibits a local minimum (a dip) below the tip of the cone where the two objects are closest. As an explanation, it was suggested that as the cone tip becomes sharper, its radiation pattern approaches that of a point dipole with the axis normal to the plate, which has zero Poynting flux at the center [209].

C. Fluctuating surface current formulation

The fluctuating surface current (FSC) formulation of thermal radiation was introduced by Rodriguez and colleagues [108,212,213] based on the surface-integral-equation (SIE) method of classical electromagnetics [223]. Similar to the scattering matrix approach, it is capable of dealing with systems composed of arbitrary bodies, including bodies enclosed by other objects. Further, it also results in compact trace formulas for key quantities like emission from an isolated body or radiative heat flux between objects. These trace formulas subsequently allow straight-

forward demonstration of the positivity and reciprocity properties of thermal radiation. Also, the contribution from the environment to radiative heat transfer can be included [108].

Although both the scattering approach and the FSC formalism can be expressed in terms of various matrices, their physical meanings usually differ [110]. The key difference between these two formulations lies in how the wave generation and scattering process is conceptually pictured. The scattering matrix approach in general is concerned with a set of incoming and outgoing partial waves related by the scattering matrices, with unknown fields distributed through the volume of the bodies. In comparison, the FSC approach is formulated in terms of unknown electric and magnetic currents existing on the surfaces of the objects. These currents are arbitrary, fictitious vector fields that do not have to satisfy any wave equation, leading to great flexibility in the choice of basis. However, the overall effect of these currents is such that they effectively replace the sources inside the scatterers. The validity of the FSC is found in the well-known equivalence principle of classical electromagnetics [224].

With suitable spectral bases, the FSC trace formulation also results in semi-analytical results for basic geometric configurations as obtained from the GF approach. However, one is not limited to a few spectral bases [108]. Since the currents exist only on the surfaces, it is possible to use BEM which features a surface rather than volume discretization scheme, potentially reducing the number of unknowns to be solved for. This renders the FSC approach particularly appealing for more complex systems. In practice, the so-called RWG (Rao-Wilton-Glisson) basis [225] has been favored with vector-valued polynomial functions defined locally on a mesh of triangular pads. Such a basis allows improved numerical accuracy with increasingly finer meshing. Unlike the well-known finite element and the finite difference methods, BEM usually results in dense matrices which require intensive matrix operations dominating time consumption for large systems. This makes BEM a good choice for systems of moderate complexity, but not as good for very large systems where a huge amount of computer memory is needed, dramatically decreasing the speed of dense-matrix solvers. Still, it can achieve relatively faster convergence using established algorithms like adaptive mesh refinements [108]. We note that interested readers can explore the free, open-source software implementation of BEM offered by Homer Reid [226].

The FSC formulation, has been employed recently to analyze NFRHT in a range of novel configurations involving bodies of various shapes and finite sizes. These include two cylinders of

various relative orientations [108], a cone over a circular plate [108], two cones [108], two rings [212], two circular plates [212] and a sphere or a cylinder over a perforated plate [213]. For the case of a cone and a plate, the former result regarding the spatial distribution of heat transfer from the scattering matrix approach was confirmed [209]. While for the cylinder versus perforated plate system it was found that, contrary to most systems showing monotonic increase of heat transfer with decreasing separation between bodies, there exists a local maximum heat transfer rate at certain separations with both smaller and larger gaps showing lower rates [213]. The FSC results were compared and confirmed with the finite difference time domain method, which is discussed next [213]. Finally, we note that the FSC approach also allows for the surface roughness to be investigated [2].

D. Finite difference time domain method

In classical electromagnetism, the finite element time domain method (FDTD) [227] is widely employed to obtain the broadband frequency response of a system in a single simulation by computing the Fourier transform of the time response of a system to an impulse excitation. Examples of computed quantities include the absorption, reflection or transmission spectra from structures of interest, making it particularly suitable for designing photonic crystals potentially useful in photovoltaic and thermophotovoltaic devices [214,215]. The FDTD method solves the time domain Maxwell's equations by discretizing space and time, and explicitly simulating the evolution of fields. When dealing with thermal emissions, one can either start with the Maxwell's equations, or consider the polarization response $\mathbf{P}(t)$ of a system to a local electric field $\mathbf{E}(t)$ and a random force term $\mathbf{K}(t)$ through a Langevin-type equation of motion [110,214],

$$\frac{d^2\mathbf{P}}{dt^2} + \gamma \frac{d\mathbf{P}}{dt} + \omega_0^2 \mathbf{P} = \sigma_e \mathbf{E} + \mathbf{K}(t), \tag{2-18}$$

where $\mathbf{P}$ is also connected to $\mathbf{E}$ by the constitutive relation $\mathbf{D} = \varepsilon_0 \varepsilon \mathbf{E} = \varepsilon_0 \mathbf{E} + \mathbf{P}$; γ represents dissipation in the system; ω_0 and σ_e are respectively the resonance frequency and strength. Vital to either case is the implementation of the random source term, which although is well-defined in frequency domain by the FDT, is not so obvious to construct in the time domain. To this end, various models have been proposed [110,214,216,217]. For example, an approximation to the source term in Eq. (2-18) is obtained by invoking the FDT, which states that the frequency do-

main correlation $\left\langle K_l(\mathbf{r},\omega)K_m^*(\mathbf{r}',\omega)\right\rangle$ for $\mathbf{K}$ is proportional to $\Theta(\omega,T)$. The time correlation function of $\mathbf{K}$ can be obtained via Fourier transform of the frequency domain correlation, however, a direct Fourier transform would involve temporal convolution. Consequently, one Fourier-transforms instead the spectrum for $\mathbf{K}'(\mathbf{r},\omega)=\sqrt{\mathbf{K}(\mathbf{r},\omega)}\big/\Theta(\omega,T)$ which is white. For FDTD implementations working directly with the Maxwell's equations, sources based on fast Fourier transform [216] and the so-called Ricker wavelet [217] have also been independently used. In addition to the source terms, the dielectric properties of materials which are usually measured and modeled as a function of frequency should also be Fourier-transformed to obtain the corresponding susceptibilities in the time domain. Further, in this technique it is necessary to pay careful attention to correctly modelling the boundary conditions.

Being statistical in nature, results from the FDTD method usually look "noisy" and multiple runs need to be performed to obtain meaningful results with acceptable errors [110,213,215]. In spite of the fact that FDTD is a volumetric method it usually requires much less memory in comparison to BEM, due to the sparse nature of the matrices involved. Further, FDTD may be conceptually the most simple and intuitive method for treating arbitrary geometries and materials.

E. Wiener chaos expansion approach

Maxwell's equations with random thermal current sources are stochastic partial differential equations (SPDE), hence in principle they can be solved via popular approaches like the Monte Carlo method as well. Alternatively, one can exploit the Wiener chaos expansion (WCE, also referred to as the Hermite polynomial chaos expansion) method. Separating the deterministic effects from the probabilistic in the solutions of an SPDE, the WCE and other polynomial expansions have a long history of being used in physics and engineering, including discussion of the Navier-Stokes equations [228]. As to the area of thermal radiation, the WCE method provides in essence a way of modeling the current source terms.

Following the notations of Wen [218], one first assumes that the random current is a separable function of space and time such that

$$J_l(\mathbf{r},t)=dW(\mathbf{r})V(t) \tag{2-19}$$

where $V(t)$ is a deterministic function of time describing the time variation of the current sources, and $dW(\mathbf{r})$ is the derivative of white noise and represents the spatial randomness. And for steady state thermal radiation, $V(t)$ is a constant given by the FDT, capturing the strength of the fluctuation. The key idea in the WCE method lies in the expansion of $dW(\mathbf{r})$ into the linear combination of a set of deterministic, orthonormal current eigenmodes. Subsequently, the effect of $dW(\mathbf{r})$ is obtained as a sum of contributions from these basic current modes. The chief issue then is in identifying the current modes appropriate for a given system [218,219].

Based on the brief discussions above, it is obvious that the WCE can be combined with the FDTD method. However, it is also natural to use WCE in conjunction with the finite difference frequency domain method [218,219]. The validity of the WCE method in treating thermal radiation problems has been verified using the infinite parallel-plane configuration [218]. Further, it has also been used, instead of the effective medium theory, to compute the emission/absorption properties of hyperbolic metamaterials in the form of metal-wire array [219].

F. Thermal discrete dipole approximation

The thermal discrete-dipole approximation (TDDA) was proposed [220] based on the well-known discrete-dipole approximation (DDA) [229] in classical electromagnetism, which aims to solve scattering problems by discretizing material bodies into volumes small enough to be considered as electric point dipoles. Established via the same general procedure, TDDA differs from DDA in having the thermal fluctuation of dipoles being the source, instead of incident fields associated with external illumination. A detailed derivation starting from the stochastic Maxwell's equations was given by Edalatpour and coworkers [220]. Briefly, in this analysis the authors start by separating the electric field into the incident and scattered fields, with the incident field interpreted as the thermally generated field propagating in absence of the scatterers. The various criteria of convergence as well as the oscillatory behavior of the solutions with respect to increasing number of dipoles were also discussed.

Similar to DDA, TDDA is expected to be applicable for arbitrary geometries. In order to verify its validity, NFRHT between two spheres was computed and compared to analytical solutions from the Green function formalism. The method was also subsequently used to calculate the NFRHT between two cubes each with a side length of 500 nm [220].

2.4.3 Results from computational studies

Computational investigations of the electromagnetic near-field have provided deep insights into the novel phenomena that are expected to arise in NFRHT and have highlighted the possibility of coherent, narrowband thermal emissions at emissive powers which are orders-of-magnitude higher than the blackbody radiation limit. These studies have also suggested a range of possibilities where NFRHT can be employed to rectify, amplify and modulate radiative heat flow, and to develop and facilitate a broad range of applications such as energy conversion,[70-86] coherent thermal sources [33-40], thermal management and data storage [44-69], lithography [22], and thermal microscopy [41-43]. Below, we provide a summary of the key computational results and proposals, with a few experimental findings briefly introduced as needed.

A. Heat transfer enhancement and reduction

A large number of computational studies [24-26] have explored the strong gap-size dependence of thermal conductance between semi-infinite parallel plates in the near-field. This is particularly interesting as it is in strong contrast to the gap-independent heat transport predicted by Stefan-Boltzmann law for far-field radiative heat transfer. And this interesting fact about NFRHT was widely noted right from the inception of the field and has since remained one of the most explored characteristics of NFRHT—especially given its great engineering relevance. Recent studies on NFRHT between parallel semi-infinite plates have been concerned with the mechanisms, materials and structures necessary to enhance radiative heat flow beyond what can be readily achieved using metals, which were the focus of early studies [94].

One of the important advancements [158] was the recognition that NFRHT between polar dielectrics can be significantly higher in magnitude than that between metals. This is primarily due to a large contribution from surface phonon polaritons (SPhPs), which are coupled surface modes of electromagnetic waves (photons) and lattice vibrations (phonons). Unlike the evanescent waves generated due to frustrated total internal reflections (Figs.2-1a, b), these resonant surface modes decay exponentially on both sides of the interface. Since the excitation energies of SPhPs of several dielectrics such as silicon dioxide (SiO_2) and silicon carbide (SiC) are comparable to $k_B T$ (25 meV) at room temperature, all these modes are populated and contribute to NFRHT [158]. It is to be noted that although metals support surface plasmon polaritons (SPPs) which are coupled modes between photons and the collective excitations of free electrons (plasmons), the

heat flow in the near-field has no significant enhancements due to these modes as their excitation energies are much larger than $k_B T$ at room temperature. In comparison, doped semiconductors such as Si [160-162] feature higher heat flow than metals as they support SPPs at lower energies. In addition to semiconductors like Si, graphene has received a lot of interest [49,76,80,135-138] in computational studies of NFRHT due to the ability to tune its electronic and optical properties in addition to its excellent mechanical and thermal properties. Further, graphene is noteworthy in its ability to support SPPs over a large frequency range, from terahertz to near-infrared [136].

Another extensively explored configuration is semi-infinite planar bodies featuring either nanostructured surfaces or heterostructuring [121,124,125,127,128,130]. These include 1D gratings [215] and periodic layered photonic crystals [121,124], 2D patterns featuring arrays of holes [125], nanotubes [126] and nanowires [133], as well as metamaterials with chirality [129]. It has been suggested that the creations of surface Bloch modes and additional electric and magnetic resonant modes result in a further increase in NFRHT as they open new channels for heat transfer. Magnetic contribution to heat transfer was demonstrated computationally in a composite of potassium bromide matrix and SiC nanospheres. Further, thin polar dielectric films and coatings can potentially enhance heat transfer beyond their bulk counterparts due to hybridization of the SPhPs on the front and back surfaces [166-170,172]. Finally we note that although the potential of nanostructured hyperbolic metamaterials to greatly enhance heat transfer has been widely discussed [129,140-145,147], a recent paper pointed out that a thin film with optimized thickness can achieve this as well [146].

Apart from computationally probing NFRHT in novel structures and materials, fundamental limits to the magnitude of radiative heat flow have also been obtained, and the maximum heat flow per channel was established [22] to be $3\pi k_B^2 T^2/\hbar$—the quantum of thermal conductance. Further, studies have also focused on parametric optimizations of material dielectric functions aiming to maximize heat currents in the near-field [148-151,153,154]. For example, it was shown that for gaps above 1 nm, materials with dielectric functions in the form of $\varepsilon = -1 + i\alpha$, where $\alpha << 1$ yield the maximum heat flow. Note that configurations with spectrally matched emitters and receivers are desired to accomplish such maximization [148].

Finally, we note that NFRHT could also be used to suppress heat transfer to values below the far-field limit at suitably chosen gap sizes due to interference effects, a phenomenon which was

observed by early researchers [94] in their computational studies of NFRHT between metals. Besides, parametric studies were also performed to suppress radiative heat transfer in order to improve thermal insulation [152]. It is important to emphasize, however, that neither the suppression of heat transfer via near-field nor the predicted enhancement of thermal conductance—by several orders of magnitude—has been experimentally confirmed directly in the plane-plane configuration (Fig. 2-1b) at room temperature. This lack of experimental confirmation is primarily due to major instrumentation challenges as described in Sec. 2.5.

B. Spatial and temporal coherence

Thermal radiation is usually considered to be spatially incoherent, with a coherence length comparable to or smaller than half the wavelength of interest because the emissions are caused by the random fluctuation of charges. As a measure of the spatial correlation of the thermally generated electromagnetic field, the spectrally-resolved spatial coherence length can be characterized using the cross-spectral density tensor $\ddot{\mathbf{E}}\left(\mathbf{r},\mathbf{r}',\omega\right)$, whose components are given by $E_{ij}\left(\mathbf{r},\mathbf{r}',\omega\right)=\left\langle E_i\left(\mathbf{r},\omega\right)E_j^*\left(\mathbf{r}',\omega\right)\right\rangle$ [33]. Mathematical expressions of this tensor for specific systems in terms of the Green dyads can be derived following the discussions and equations in Sec. 2.4.1. Indeed, it was numerically shown for tungsten (W, commonly used in incandescent lamps) that the correlation length at a wavelength λ = 500 nm can be as small as ~0.06λ [33]. However, recent computational inquiries [33-40] into the thermal near-field has shown the possibility of having large partial spatial coherence in thermal emissions. Actually, for materials supporting SPPs and SPhPs, it has been shown that the correlation lengths at the respective frequencies can reach many times the resonant wavelength [33]. It is suggested that in the vicinity of the surfaces, the delocalized surface modes (SPPs and SPhPs) which can propagate along the surfaces for tens of wavelength, could pass their spatial coherence to the near-field [33]. At a distance of z = 0.05λ away from a plane material surface, both gold (Au) and silver (Ag) exhibit large correlation length at λ = 620 nm as they support SPPs of this wavelength, as compared to the short correlation for W which do not. For polar dielectrics supporting SPhPs such as SiC, the dominant effect of SPhPs on the spatial coherence is confirmed by comparing the correlation lengths on and off resonance. Apart from revealing spatial coherent thermal emissions in the near-field, Greffet *et al.* [34] have even designed and experimentally tested a highly directional (as compared to Lambertian emission [87]) thermal source working in the far-field in the form of a SiC grating. The

origin of this coherent emission is considered to lie in the diffraction of SPhPs by the grating into the far-field.

The temporal coherence properties of the thermal near-field are indicated by the spectral energy density or density of states [24]. with a broad spectrum implying poor temporal coherence and a narrow one representing better coherence. Similar to the spatial coherence, they have been widely discussed. It is now a well-established fact that in the presence of surface resonant modes like SPhPs, thermal radiation very close to the surface and heat transfer across extremely small gaps can be confined to a very narrow frequency window(s), approaching monochromatic emission for nanoscale distances [24]. This characteristic is of key importance to the development of novel thermophotovoltaic devices where the emission peak can be properly matched to the bandgap of the photovoltaic cells—reducing waste heat and increasing device energy conversion efficiency.

C. Gap-dependent penetration depth

A question that received attention recently is regarding the effect of thin films on NFRHT. For example, Francouer *et al.* studied [168] the effect of film thickness on NFRHT and computationally showed considerable enhancement in NFRHT due to contributions from SPhPs. Specifically, they studied NFRHT in two scenarios: 1) between two bulk SiC surfaces and 2) between a 10 nm thick SiC emitter and a bulk SiC receiver. They showed that the total radiative flux is 2.2 times larger in the latter scenario due to coupling of SPhPs in the film. Further, Fu *et al.* studied the effect of film thickness on NFRHT by computationally studying NFRHT between a bulk SiC substrate and an aluminum (Al) metal surface coated with SiO_2 films of different thicknesses (10 nm, 100 nm, 1 μm, 10 μm and infinite thickness). They concluded that the NFRHT enhancement by the thinner films is significantly smaller than that of thicker films at large gap sizes but becomes almost identical to the thicker film at very small gap sizes (~10 nm). They argued that at small gaps NFRHT is dominated by the SPhPs and hence even a film as thin as 10 nm can act like a bulk film. Moreover, Basu *et al.* computationally studied [188] the penetration depth of evanescent waves between two semi-infinite SiC surfaces and doped Si surfaces. From their studies they concluded that extremely small skin depths can exist and argued that the skin depth is proportional to the spatial separation between the surfaces. More recently, Song *et al.* experimentally and computationally studied [2] the effect of both film thickness and gap size on

NFRHT and demonstrated that NFRHT between a thin SiO_2 film and a thick SiO_2 substrate becomes identical to that between two thick SiO_2 surfaces when the gap size becomes smaller than the film thickness. They explained these results in terms of the mode shapes of cavity surface phonon polaritons and how the transmission properties of these modes are affected upon varying the gap size. More details of the experiments and the analysis is presented in Chapter 3.

D. Modulation of heat flow

Proposals to modulate radiative heat flow have been made based on various mechanisms [47-55]. One theoretically trivial idea is modulation of the gap size. Beyond that, the first and most straightforward scheme exploits the dependence of NFRHT on the geometric asymmetry of the surfaces or objects. For example, since NFRHT between two gratings [139] or two cylinders [108,212] depends on their angular alignment, NFRHT can be controlled by changing the relative orientation. Further, translational alignment can also be used to affect the NFRHT between two-grating configurations without changing the gap size. It was also shown that NFRHT between anisotropic nanoparticles can be modulated by controlling their orientations [55]. Another computational approach leverages phase change materials [47,48], as a change of phase inevitably leads to dramatic change in material dielectric properties. These include a material called AIST (an alloy of silver, indium, antimony, and tellurium, already commercially used for memory cells) [48]. and materials which experience metal-insulator transitions (MIT, for example VO_2) [47]. Phase change of AIST can be easily achieved by applying external electric field, while MIT occurs when a critical temperature (T_C) is crossed. We note that MIT of VO_2 (T_C = 340 K) leads to a much more significant increase of heat flow due to contribution from the SPhPs supported in its insulating (dielectric) phase. Further, computations suggest [129] that NFRHT in chiral materials with magnetoelectric coupling can potentially be tuned by ultrafast optical pulses. It has also been suggested that NFRHT between ferroelectric materials can be tuned [52] with external electric field. At last, we note that very few of these proposals have actually been experimentally realized.

E. Thermal diodes

Rectification of heat flow refers to the situation where the magnitude of heat current depends on the direction of applied thermal bias [230,231]. A device that rectifies heat flow is often referred to as a thermal diode in analogy to an electrical diode. The defining characteristic of a

thermal diode is the degree of asymmetry in the forward (Q_f) and reverse (Q_r) heat currents when an identical temperature differential is applied in two different directions, where forward typically corresponds to the direction that results in a larger Q_f than Q_r. Slightly different definitions of the rectification capacity have been used by different research groups in the past. Below, we follow the commonly used definition of thermal rectification ratio $R_{fr} = (Q_f - Q_r)/Q_r$ [232]. Although thermal diodes based on heat conduction and convection have long been proposed and studied, radiative thermal diodes were only proposed in recent years, exploring both near-field [56-58,60-62,64] and far-field thermal radiation [59,63,65].

The first proposal and many subsequent ones are based on the temperature dependence of material dielectric functions, which causes spectral mismatch between the peak wavelengths of the emitter and the receiver [56,57,61]. Specifically, Otey *et al.* [56] investigated rectification between 3C-SiC and 6H-SiC half spaces, considering the temperature dependence of the SPhPs supported by SiC. A maximum rectification of $R_{fr} = 0.41$ was obtained for gaps from ~10 nm to ~200 nm, with the high and low temperatures being T_h = 600 K and T_l = 300 K, respectively [56]. Recent computational studies of NFRHT between a lightly (10^{18} cm^{-3}) doped-Si film and a heavily (10^{21} cm^{-3}) doped-Si half space have demonstrated that for small gaps (1 nm to 50 nm), rectification ratios greater than 0.5 can be achieved [57]. In this study, the thin film was chosen to take advantage of hybridization of SPPs on the front and back surfaces. In another study by Wang and Zhang [61], NFRHT between intrinsic Si and doped-Si and between intrinsic Si and SiO_2 (T_h = 1000 K and T_l = 300 K) was studied and rectification ratios of 9.9 and 2.7, respectively, were reported when the gap size was 5 nm. In the same work NFRHT was studied between intrinsic Si and Au and a smaller rectification $R_{fr} = 0.8$ was obtained, albeit for a much larger gap size range (10 nm - 500 nm) with T_h = 600 K and T_l = 300 K.

Apart from near-field thermal diodes, far-field rectification schemes have also been proposed [59,63,65]. One such scheme is based on two 1D periodic layered structures each featuring one Fabre-Perot cavity which function as selective emitters with sharp emission peaks [65]. The temperature dependence of the dielectric properties of the Au mirror layers and the highly-doped Si mirror layers is key to the obtained thermal rectification. Specifically, for a T_h = 670 K and T_l = 300 K, a rectification of ~0.23 was reported. One benefit of this design is in its potential for optimization depending on the temperature of the emitter and receiver as the spectral characteristics

of the selective emitters can be tuned via suitable choice of the materials and dimensions of parameters of the composing layers. Further, rectification based on MIT materials was also investigated [59,60]. In one case [59], VO_2 and SiO_2 were used. For far-field radiation, a rectification greater than 0.7 was obtained with emitter and receiver temperatures near the critical temperature T_C of VO_2. In another case, NFRHT between VO_2 and a second MIT material, $La_{0.7}Ca_{0.15}Sr_{0.15}MnO_3$ (LCSMO, T_C = ~301 K), was exploited and a rectification ratio of 7.7 was obtained at a gap of 10 nm, with T_h = 80 K and T_l = 26 K [60].

Finally, ultrahigh-contrast and large-bandwidth thermal rectification between a large and a small nanosphere was suggested, exploiting the scale invariance properties of the resonance modes of the spheres, which result in a large difference in the coupling constants between relevant modes in the forward and reverse scenarios [62]. Rectification ratios greater than 10 were reported for two 3C-SiC nanospheres.

F. Thermal transistors and passive amplification of heat flow

Thermal transistors were also computationally proposed and were suggested to control the flow of heat in a fashion analogous to electronic transistors. Ben-Abdallah and Biehs[67] proposed a three-body system that can function as a radiative thermal transistor based on the MIT of VO_2. In their proposal a VO_2 nanofilm is sandwiched by two SiO_2 plates, one SiO_2 plate serves as the source terminal of the transistor and is held at 360 K, which is 20 K above the critical temperature of VO_2, while the other one is held at room temperature (300 K) and serves as the drain terminal. The VO_2 film serves as the gate. The heat flux out of the source and into the drain drops dramatically as the temperature of the gate film T_G increases beyond T_C, which leads to an insulator-to-metal phase transition. The reason lies in the reduced coupling between a metal (metallic phase) and dielectrics (SiO_2), as compared to between two dielectrics (insulating phase and SiO_2). By varying T_G such that it crosses the critical temperature, it was suggested that one can effectively switch the heat flow on or off between the source and drain. Further, by modulating the external heat supply (say using Joule heating) to the gate by a small amplitude, one can modulate the source and drain heat flow by an order of magnitude if operated around T_C. An amplification factor of ~4, as defined by the relative change of drain current to gate current, was obtained using an effective medium theory to account for the effective dielectric function of the

gate film around the transition temperature, when both metallic and insulating phases are present [233].

Apart from active amplification of heat flow, passive measures by insertion of a third film in a parallel-plate system has also been discussed [66]. It was shown that the insertion of a thin film in the middle can induce an effective heat flow between two plates separated by a gap of 2*d* higher than the heat flow between the same two plates separated by *d* without the film.

G. Thermal memory devices

Thermal memory devices are essential for the construction of the thermal analog of an electronic computer [231]. The two states in a thermal memory device operating between a hot and a cold thermal reservoir (as compared to a high and low electric potential) are defined by two distinct equilibrium temperatures corresponding to vanishing heat fluxes within the device [231]. Although phononic thermal memory designs were introduced a few years ago, photonic memory devices based on thermal radiation have only recently been proposed [68,69]. In all cases negative differential thermal conductance (NDTC)[234] was found to be a necessary mechanism for creating thermal memory devices. While the second necessary component is the existence of bistability, which is only present in many-body systems. The design proposed by Kubytskyi *et al*.[69] for thermal memory takes advantage of the MIT of VO_2 and can be created by just utilizing far-field radiative effects, although taking advantage of near-field effects can improve the time constants. The design of Elzouka *et al*.[68] exploits the effect of thermal expansion and the nonlinearity of NFRHT.

H. Potential of near-field thermal radiation in energy conversion and other applications

A variety of near-field thermal radiation based devices for energy conversion have been proposed by many researchers [70-86]. For example, Park *et al*.[73] have suggested that near-field radiation could be employed to enhance the power output of thermophotovoltaic (TPV) devices. Recent computational studies have also discussed the possibility of using graphene based near-field thermophotovoltaic (NTPV) devices to achieve extremely large efficiencies. We note that while advances[79] in TPV devices have demonstrated the feasibility of using nanostructured surfaces for improved thermophotovoltaic energy conversion, to date there has not been any experimental demonstration of a highly-efficient NTPV device despite the many appealing computational proposals. Apart from thermophotovoltaic energy conversion, Yang *et al*.[83] have com-

putationally explored the potential of a thermoelectric device where the hot side of the device is coupled to a hot thermal reservoir across a vacuum gap via near-field thermal radiation. The authors suggested that in such a device it is possible to establish a higher non-equilibrium temperature for the electrons than for the phonons thus effectively attenuating the deleterious contributions of phonons to thermoelectric performance. The effect of NFRHT on thermionic energy conversion devices was also discussed [85,86]. In addition to the possibility of creating novel energy conversion devices, Pendry[22] has suggested that near-field radiation could potentially be employed for achieving high-resolution thermal lithography. Finally, it also seems that understanding NFRHT, especially in the 1-10 nm gap regime, may be important for optimizing the performance of heat-assisted magnetic recording (HAMR) technologies[44-46] where a plasmonic antenna (which localizes the electric fields) is used to heat a magnetic recording medium[45] so as to lower the magnetic coercivities in localized regions. In these devices, it is expected that NFRHT can play an important role in the steady-state temperature achieved in the magnetic medium and hence understanding NFRHT could help optimize the performance of HAMR technologies.

2.5 Experiments

In comparison to the considerable number of theoretical and computational studies, experimental studies on near-field thermal radiation are rather limited in number due to a variety of challenges. Here, we review the experimental techniques currently available for NFRHT studies and describe their strengths and limitations. We first note that almost all the theoretical calculations available for near-field radiative transport focus on the parallel-plate configuration, and in almost all cases dramatic effects arise only at nanoscale gaps. However, this is one of the most difficult geometries to experimentally realize because it is extremely hard to achieve and maintain good parallelism between macroscopic plates at nanometer separations. Therefore, to date all the quantitative measurements [102,103,235-238] of near-field heat transfer between parallel plates have been limited to micrometer-sized gaps, including recent measurements of NFRHT between sapphire plates published within the last few years [235]. Some of the challenges in performing near-field measurements can be circumvented by use of the tip-plate and sphere-plate configurations. The latter configuration has in particular been extensively leveraged lately for

performing a variety of quantitative NFRHT studies. Below, we provide a brief summary of these experimental efforts.

2.5.1 Plate-plate

The first plate-plate measurements were, to our knowledge, reported by Cravalho, Domoto and Tien in an AIAA conference [101] and in a subsequent paper [103]. Their apparatus consisted of two parallel copper disks with a diameter of 85 mm that were located in an ultra-high vacuum chamber (10^{-12} torr), which was cooled to ~4.2 K by complete immersion in a bath of liquid helium (see Fig. 2-3a). The top disk serves as a radiative emitter with its temperature raised by a few Kelvin via Joule heating by attached carbon resistors. The radiative heat currents received by the bottom disk (receiver) were estimated by measuring the increase of the receiver's temperature. The spatial separation between the disks was changed from as large as 2 mm to as small as 10 μm by displacing the emitter disk using an external micrometer adjuster. Mechanical contact between the disks was detected by monitoring the electrical conductance between the disks. However, a controlled approach for tuning the parallelism or quantitatively estimating it seems to be lacking. Their experimental data (Fig. 2-3b) showed "definite gap-size dependence of radiative transfer" with as large as a factor of five increase in radiative heat flow at small gaps (~10 μm). The overall enhancement in the measured heat flow was an order of magnitude larger than what they computationally predicted by accounting for wave interference and tunneling [91]. They attributed this discrepancy to the deviation from parallelism and to uncertainties in both the surface conditions of the copper disks in the experiments and in the optical properties used in their calculations.

A similar experiment with copper disks (107 mm diameter) was also carried out later by Kutateladze, Rubtsov and Baltsevich [104] where the spatial separation between the disks was varied from ~250 μm to ~10 μm and a range of temperature differentials and absolute temperatures were investigated at about 2×10^{-7} torr. These measurements confirmed the strong distance dependence of NFRHT in all cases, demonstrating a five-fold enhancement at small gaps, although no comparison with theory was provided. Their results also showed that the threshold gap size beyond which heat transfer enhancements are observed is $\sim 3\lambda_{BB,\max}$, where the peak wavelength was estimated from Wien's displacement law and the known temperature of the emitter.

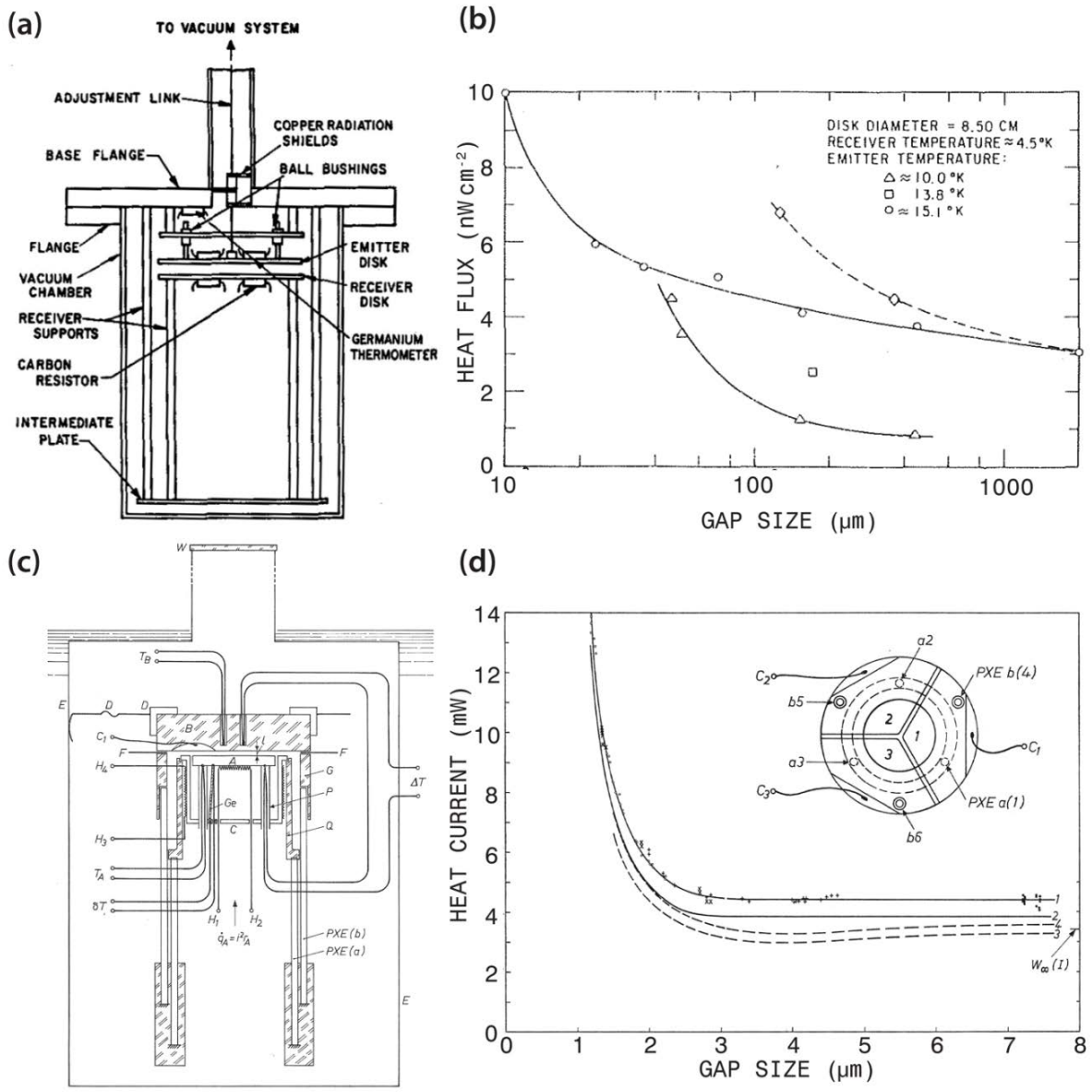

Figure 2-3. Early experimental investigations of NFRHT between parallel planes. (a) Schematic of the plate-plate setup used by Cravalho *et al.* [101] (b) Results[103] for radiative heat flux versus the spacing between copper disks using the setup in (a) for temperature differences ΔT of 10.0 K, 13.8 K and 15.1 K. (c) Schematic of the plate-plate setup used by Hargreaves [100]. (d) Results [100] for heat current versus gap size between Cr-coated surfaces near room temperature. Curves (solid lines) have been fit to the experimental data before (1) and after (2) accounting for heat losses. Theoretical curves calculated using Drude model values from the literature [94] (3) and empirically fitted values (4) are also shown. Inset: Schematic top view of the pyrex disk with its three sectors of evaporated Cr. The entire surface serves as the receiver, while the three sectors form three independent capacitors with the Cr coating on the emitter. Panels (c) and (d) were adapted from the Ph.D. thesis of Hargreaves [100].

The first plate-plate NFRHT studies at room temperature were reported by Hargreaves in 1969 [102]. The experimental setup as reported in his thesis [100] features a chamber, which is pumped to about 10^{-5} torr (see Fig. 2-3c), and can be immersed in liquid baths of different temperatures. In this setup both the macroscopic emitter and receiver plates (25 mm diameter) were each supported by three independent piezoelectric ceramic tubes, enabling precise tuning of the gap size as well as the parallelism between the plates. The parallelism of the plates was evaluated using both optical interferometry and by measuring the electrical capacitance of three individual capacitors created by three pairs of metallic plates integrated into the emitter and receiver disks (Fig. 2-3d inset). Specifically, the differences in the three capacitances indicated the level of parallelism, whereas the sum signal served as a measure of the absolute gap size. Mechanical contact between the plates could also be detected by monitoring the electrical conductance between the plates. Chromium was selected as the surface coating (100 nm thick) for both plates as it features a relatively low reflectivity and high hardness, with the former property contributing to higher heat currents and the latter providing robustness against surface damage during the parallelization of the plates, for which inadvertent contacts occur. Individual plate temperatures were measured with embedded thermistors, while their difference was measured using copper-constantan thermocouples. With the emitter heated resistively, the radiative heat flow to the receiver was estimated as the additional heat input required to maintain the temperature of the emitter at a constant value as the gap size was varied from ~8 μm - 1 μm.

Preliminary results reported [102] by Hargreaves in 1969 clearly showed a strong distance dependence of radiative heat transfer at room temperature (emitter temperature 323 K and receiver temperature 306 K), with a noticeable increase starting at a gap size of ~2.5 μm (the figure in the original paper mislabeled the range in the x-axis [100]). However, computational results permitting a comparison were only obtained later in 1971 by Polder and van Hove [94]. And despite the broad agreement, the measured heat currents at bigger gaps were a factor of three larger than the predicted value. This discrepancy was attributed to errors in the optical properties of Cr used in the computational analysis, and challenges in making accurate thermal measurements [100]. Hargreaves reported refined measurements (emitter at 313 K and receiver at 295 K) later in his thesis [100], which showed much better agreement with theory as well as a large enhancement in heat transfer (~4 fold) at the smallest gaps (see Fig. 2-3d). In addition to the room temperature measurements, studies were also performed at low temperatures, for example with

the emitter at 160 K and the receiver at 132 K, and larger enhancements were observed. Temperature dependence of the threshold gap size, as well as that of radiative heat transfer at various gap sizes was also discussed. A quantitative comparison of these improved measurements [100] with Polder and van Hove's theory showed that the predicted results were consistently smaller than the measured ones (Fig. 2-3d); nevertheless, the overall agreement was improved. The discrepancy was again largely attributed to the optical properties of the Cr layers.

Following these pioneering measurements no new experimental results on heat flow between closely-spaced parallel planes were published until the early 2000s when the growing field of micro- and nanotechnology necessitated that heat transfer between closely-spaced bodies be better understood. In 2008, Hu *et al.* [236] revisited the topic by measuring NFRHT between parallel glass optical flats (127 mm diameter) which support SPhPs in the mid-infrared as discussed in previous sections. They observed much larger enhancements in radiative heat flow than had been measured between metal surfaces in the past. Hu's experimental platform consisted of a hot glass emitter separated from a room temperature glass receiver located underneath by means of dispersed polystyrene microspheres as spacers. The emitter temperature was elevated to tens of Kelvin above room temperature and controlled to within 1 K using a heating pad attached atop it, while a 1×1 in^2 heat flux meter was placed beneath the receiver so that the radiative heat current could be measured. The vacuum gap (~6×10^{-5} torr) paired with the low thermal conductivity of the polystyrene spacers was expected to ensure that radiative heat transport dominated the total heat flux. Using spheres with a nominal diameter of 1 μm, Hu *et al.* were able to measure heat flow consistent with theoretical predictions for glass plates separated by a 1.6 μm gap. They observed that the heat flow across the micrometer gap is about twice as large as the far-field data recorded at 2 mm separation, and is about 50% larger than the blackbody limit. However, measurement with systematically varied gap size was not possible with this platform.

Subsequently, two different studies [235,238] sought to investigate NFRHT for varying gap size. The first study [235] reported NFRHT between two 50×50 mm^2 sapphire plates near room temperature as a function of vacuum (~2×10^{-7} torr) gap size and temperature difference. The experimental apparatus used in this study is illustrated schematically in Fig. 2-4a. In this experiment the gap size and parallelism were measured by monitoring the capacitance of four pairs of copper plates located in the corners of the sapphire plates. The orientation of the emitter as well as the spacing between the plates were controlled via three stepper motors. The temperature of

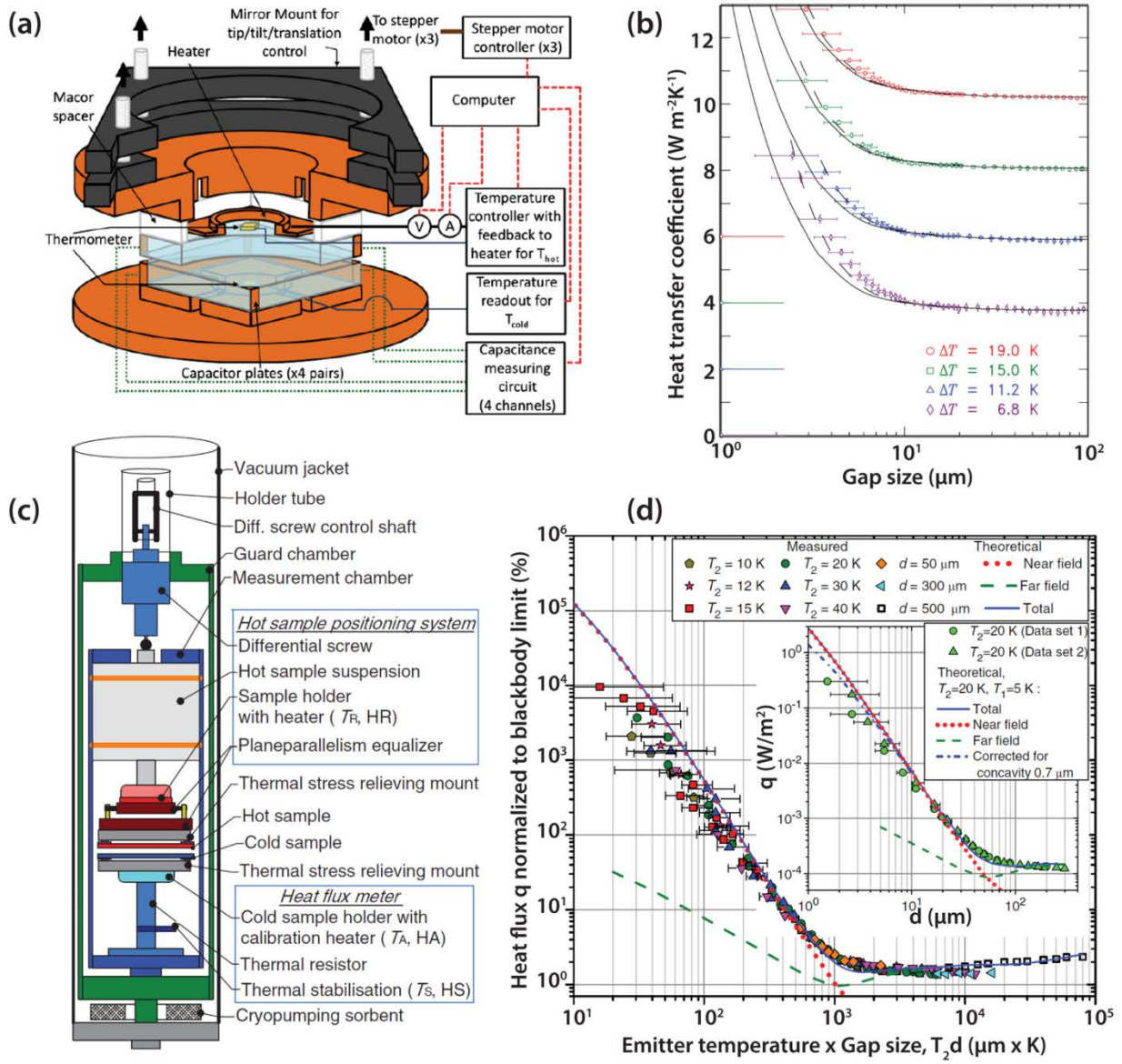

Figure 2-4. Recent experimental investigations of NFRHT between parallel planes. (a) Schematic of the experimental apparatus used by Ottens *et al.* [235] to measure NFRHT between sapphire plates. (b) Results [235] for heat transfer coefficient versus vacuum gap size between the sapphire plates for four temperature differences. Each curve is offset by 2 $Wm^{-2}K^{-1}$ from the last for clarity. Experimental data (points) is plotted alongside theory for planar (solid lines) and slightly curved (dashed lines) surfaces. (c) Schematic of the experimental setup used by Kralik *et al.* [237] (d) Their [238] measured heat flux normalized to the blackbody limit. Theoretical curves were calculated for receiver temperature T_1 = 5 K and emitter temperature T_2 = 20 K. Open squares represent far field data taken at higher temperatures with a nominally black surface. Inset: Heat flux versus gap size for the experimental conditions indicated in the legend.

the hot sapphire plate was controlled by a feedback loop, and the cold plate was attached to a thermal bath. The heat flow was estimated by monitoring the electric current and voltage across the heater and computing the power input required to maintain the desired temperature difference. Heat transfer data for temperature differences ranging from 6.8 K to 19 K were reported as a function of gap size (~2 μm - 100 μm), as shown in Fig. 2-4b. The threshold gap size beyond which appreciable heat transfer enhancements are observed was ~10 μm. And the total heat transfer coefficients monotonically increased with decreasing gap size, reaching a maximum relative enhancement of about two fold. A fairly good agreement was found between the measured and the theoretically predicted heat transfer coefficients. The measured values were found to be slightly higher than the predictions at smaller gaps while having good agreement at larger gaps. This was attributed to the slight curvature (convexity) of the macroscopic sapphire plates, which were measured using Newton rings to have a deviation from flatness of 170 ± 30 nm across the square sapphire plate. Once this curvature was considered in theoretical predictions (dashed lines in Fig. 2-4b), the agreement with experiments improved.

Another study [238] reported NFRHT between parallel W layers at cryogenic temperatures (receiver temperature at 5 K) as the vacuum (~10^{-10} torr) gap size varies from 1 μm to 500 μm for several temperature differences (ΔT = 5 K – 35 K). Their setup [237] is illustrated in Fig. 2-4c. In these experiments, a 35 mm-diameter W emitter was placed in close proximity to a W receiver via a differential screw (resolution 100 μm/rev). Parallelization between the emitter and receiver plate was achieved by bringing the two into contact with each other and then maintained after they were separated using a so-called parallelism equalizer which mechanically locks the orientation of the emitter plate by friction [237]. The receiver was mounted on a heat flux meter, which consists of two temperature sensors separated by a calibrated thermal resistance, so that the heat flow could be estimated. The results from this work [238] are shown in Fig. 2-4d, where the measured heat flow is normalized to that expected from blackbodies and is plotted with respect to the product of the emitter temperature and gap size. A threshold gap size of ~50 μm was observed when the emitter temperature was 20 K. The data is seen to agree well with the theoretical prediction except at the smallest gaps for which the measured values are noticeably lower than the theoretical lines. Similar to the sapphire-plate work discussed above, this discrepancy was attributed to the reported concavity of 700 nm across the W plates (see inset of Fig. 2-4d for corrected theoretical prediction). Remarkably, the measured heat flow at a gap size of 2 μm still

exceeded that of a blackbody by two orders of magnitude despite the concavity. This factor of 100 represents the largest near-field enhancement observed to date in parallel-plane geometry. As to relative heat flow increase from large to small gaps, about three to four orders of magnitude enhancement was demonstrated.

In addition to experimental schemes featuring independent, macroscopic emitter and receiver plates, several recent studies [239-241] have reported MEMS-based approaches to studying NFRHT between suspended microstructures that are part of a monolithic device. In one group of studies [239,240], a small gap of fixed size (550 nm [239] and 1 μm [240]) was formed between two nominally parallel SiO_2 membranes (say 200 nm and 400 nm thick, size is ~80 × 80 μm^2) [240] via etching of a sacrificial Al layer in between. The thermal measurement was performed in high vacuum (~10^{-6} torr) by resistively (poly-Si [239] or Pt [240] resistor) heating and monitoring the temperature of the emitter SiO_2 surface, both in the presence of the receiver SiO_2 surface and when it is removed with a microprobe. For the same known electric heating current, the emitter reaches different steady-state temperatures with or without the receiver; and this temperature difference is then used to evaluate the near-field thermal conductance between the two membranes. It was concluded [240] that for a gap size of 1 μm the near-field conductance was ~10 times larger than the blackbody limit when the emitter temperature was within 300 - 400 K. Although no comparison with any near-field calculation was given, the observed enhancement seems to be much higher than available theoretical predictions for bulk materials [158]. Another recent MEMS-enabled experiment [241] explored NFRHT between parallel nanobeams (1.1 μm wide, 500 nm thick, 200 μm long) coated with 100 nm-thick SiO_2. With one beam fixed and the other controlled using electrostatic actuation, they were able to cover nominal vacuum (1.5×10^{-4} torr) gap sizes between 250 nm and 750 nm with a single device. The observed near-field conductance exceeded the blackbody limit as the gap size became smaller than ~600 nm and reached a maximum of ~7 times the limit. This approach could have potential for detailed NFRHT studies if it can be adapted to study NFRHT between parallel planes instead of beams which have relatively small and poorly-defined surfaces. Note that the absolute size of the emitter and receiver could have a large impact on NFRHT considering the dominant role of surface modes and their long wavelength and propagation distance along the surfaces [120].

As shown above, the experimental investigation of parallel-plane NFRHT boasts a long history of almost half a century and a range of ingenious instrumentation efforts and achievements.

Nonetheless, many challenges remain in order to explore and exploit the rich physics in the thermal near-field. All the existing macroscopic approaches have been limited to micrometer gaps due to imperfect parallelism, surface curvature and inevitable particulate contaminations. Taking advantage of the ever maturing microfabrication technology, the MEMS-based studies represent an important experimental advancement especially since they allow the creation of nanoscale gaps and have no need for complex precision positioning and control platform. Nevertheless, the smallest gap size observed still remains in the hundreds of nanometer range; and further improvements are required to evaluate the parallelism, the surface roughness and curvature, as well as to enable measurements between a wider variety of materials/structures and across controllable gap size. At last, we note that the sub- micrometer film thickness could potentially complicate the numerical modeling process especially for larger gaps.

2.5.2 Tip-plate

The invention of the scanning tunneling microscope (STM) and atomic force microscope (AFM) by Binnig, Rohrer and colleagues at IBM Zurich in the early 1980s revolutionized the area of nanoscience and nanotechnology. Soon after the first demonstrations of these scanning probe microscopy techniques, Williams and Wickramasinghe [242], who were also at IBM (T. J. Watson center), presented the scanning thermal profiler (STP) in 1986. Similar to a STM or AFM probe, their scanning probe has a sharp (~100 nm) conical tip which features a tiny thermocouple formed by the junction of two (inner and outer) dissimilar metals. Operated in air, their probe allowed high-resolution (100 nm lateral and 3 nm vertical) surface profiling based on heat currents between the heated tip and the cold sample as compared to electric currents in a STM, eliminating the need for a conductive layer. An increased signal-to-noise ratio was observed as the tip approaches the sample [242]. Dransfeld and Xu [243] noticed that the high vertical resolution of STP implied that the heat currents must be very sensitive to the tip-sample distance. They then offered an alternative explanation for the heat flow between the tip and sample via near-field radiation [243], as compared to conduction/convection through air. Subsequently, Xu *et al.* [244,245] developed a platform similar to that used by Williams *et al.* [242] to measure the NFRHT between a scanning probe and a sample in high vacuum ($< 10^{-5}$ torr). Specifically, Xu *et al.* [244,245] devised an approach to probe NFRHT between an indium (In) needle and a planar Ag(90%)Cu(10%)-Cr thermocouple (~160×160 μm^2). The tip of the relatively soft In needle was made flat and parallel to the planar thermocouple by simply squeezing the tip onto

the thermocouple. Despite their creative and careful experimental efforts, their results were inconclusive as the thermocouple lacked the sensitivity to resolve any temperature changes until the tip physically contacted the plate. However, their work inspired the study of NFRHT in the early days by providing a new direction. The configuration of a sharp scanning tip and a planar sample makes it possible to achieve tip-sample spacing of ~1 nm without having to perform technically challenging alignment procedures, and thus allows researchers to delve orders-of-magnitude deeper into the thermal near-field than has ever been possible in the parallel-plane configuration. Conversely, the very small heat transfer areas associated with sharp tips also result in extremely small heat flows, so very high-resolution calorimetry techniques are required to measure NFRHT in this configuration.

A few years later, Müller-Hirsch *et al.* [246] reported two tip-plate experiments performed in ultra-high vacuum (UHV, ~10^{-10} torr). The first one (called the STM setup) is schematically similar to that of Xu *et al.* [245], which involved a metallic probe and a planar thermocouple. While the second experiment (called the SThM setup) involved a SThM (scanning thermal microscope) probe and a planar metallic surface. Both setups used sharp tips as compared to the flat ones used by previous researchers [244,245]. In the STM setup, a planar nickel-gold (Ni-Au, Ni on top) thermocouple with two 200 × 200 μm^2 junctions was fabricated on a glass substrate. The substrate was cooled to 100 K and a W probe tip at 300 K was brought in close proximity to one of the thermocouple junctions with the other serving as a reference. Tunneling current and thermovoltage were measured simultaneously to monitor gap size and heat flow, respectively. A noticeable temperature increase in the thermocouple was found as the gap size decreased below about 10 nm, indicating increased heat transfer from the room temperature tip to the cold sample. For the SThM setup, the authors fabricated a scanning probe with an integrated thermocouple tip (radius of curvature ~1 - 2 μm) similar to the one first presented by Williams and Wickramasinghe [242]. To prepare the tip a Ni wire was sharpened, coated with photoresist (PR), exposed to light at the tip to remove the PR, and coated again with Au, resulting in a sharp probe with a Au (30 nm thick) -Ni thermocouple formed at the tip. A sample consisting of 100 nm-thick Au deposited on freshly cleaved mica was cooled to 100 K while the probe remained at about 300 K. The probe was positioned in the near-field of the sample by establishing a tunneling current. The large temperature difference (ΔT = 200 K) between the tip and the sample yielded a detectable tip temperature drop as the gap size was reduced below 10 nm before saturating near 1 nm.

However, uncertainty in the thermal resistances of the different components within the experimental apparatuses (in both the STM and SThM setups) prevented these researchers from quantifying the heat flow for a direct comparison with theory [246].

In 2005, NFRHT between a SThM probe tip and planar surfaces of Au and gallium nitride (GaN) was investigated by the same research group [247]. The experimental setup in this work was functionally similar to that employed by Müller-Hirsch *et al*. [246], but the design of the probe was somewhat different. The redesigned probe, an illustration of which appears in Fig. 2-5a [248], was fabricated by inserting a Pt/Ir (iridium) wire into a glass micropipette and drawing the pipette until it fractured [247]. The protruding wire was electrochemically etched into a sharp (unspecified size) tip, after which the entire probe was coated with a 25 nm Au film to form a thermocouple at the junction with the Pt/Ir wire. NFRHT was studied by positioning the room temperature tip near a cold substrate (100 K) and measuring the thermovoltage that developed across the thermocouple. The tip temperature change was related to the radiative heat current between the tip and the sample via the thermal resistance (probe resistance R_{th}) between the probe tip and its thermal reservoir. The probe resistance was estimated to be 54000 K/W using independent experiments involving heating of the tip with a laser beam [247]. The authors reported ~3 orders of magnitude enhancement in heat flow as the gap size between the Au tip and a Au surface was reduced from ~200 nm to 1 nm, although the measured heat flow was less than the theoretically expected value (estimated by modeling the tip as a point-like dipole) for gap sizes less than 10 nm, as can be seen in Fig. 2-5b (dotted line). The heat flow measurements performed using a GaN substrate were also reported to be qualitatively similar. The authors proposed that non-local effects become important at extremely small gap-sizes for the geometries explored by them. By modelling the spatial dispersion of the material dielectric functions, they reported a better agreement in the trend between experiment and their dipole calculation (Fig. 2-5b, solid line).

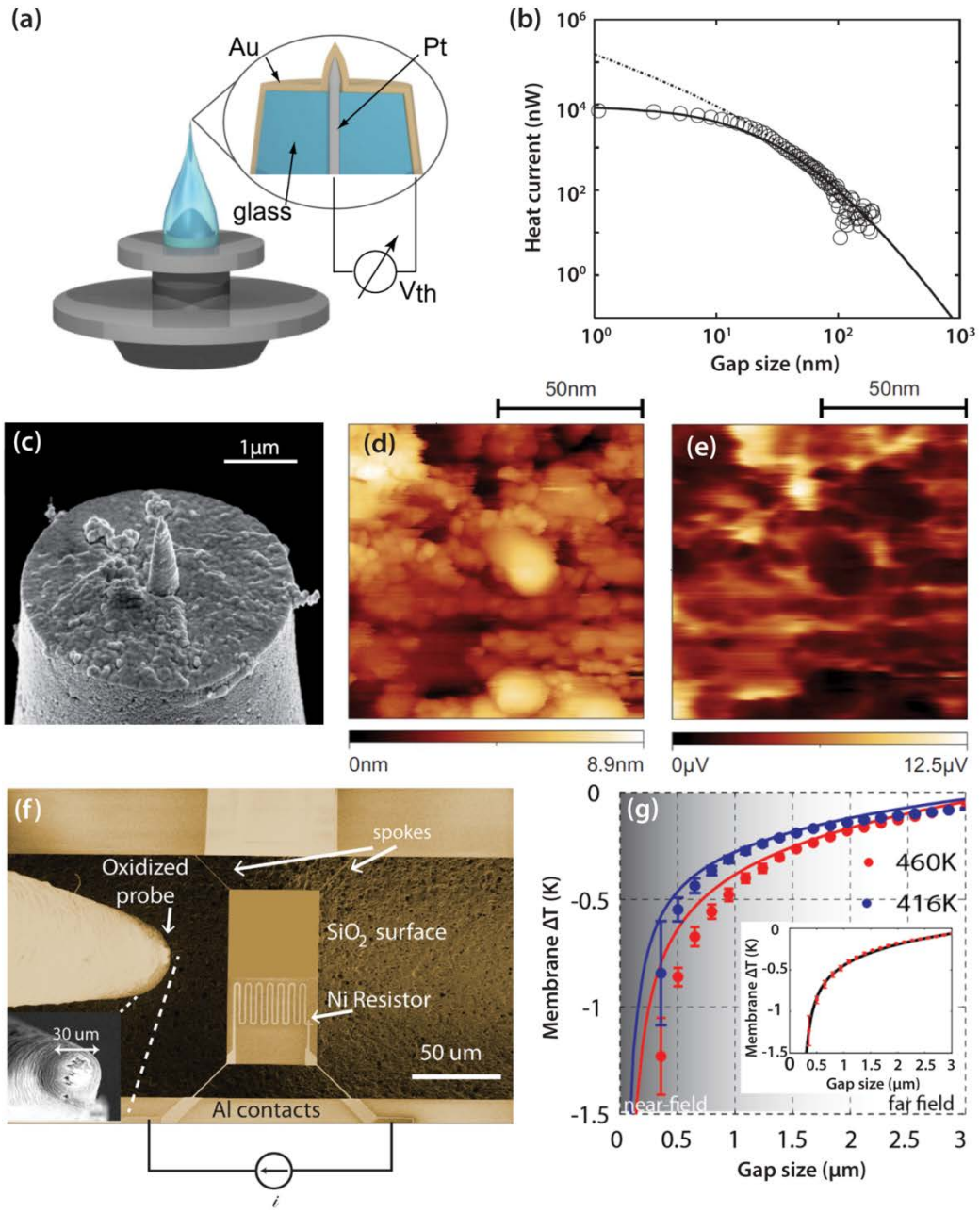

Figure 2-5. Measurement of NFRHT between a tip and a planar sample. (a) Illustration of the SThM probe used by Worbes *et al.* [248]. (b) Heat current versus gap size for Au tip and sample [247], including measured data (open circles), modelling result with local (dashed line) and non-local (solid line) dielectric response. (c) SEM image of the tip [248]. (d) Image of a Au surface obtained via STM [42]. (e) Thermal image of the same Au surface [42]. (f) SEM images of the suspended SiO_2 membrane and the SiO_2-coated probe used by Guha *et al.* [249]. (g) Membrane temperature drop versus tip-plane distance for two initial temperatures: experimental data (dots) and theoretical curves (lines). Inset: Shifting the data by 160 nm improves agreement between theory and experiment.

Further, researchers were able to use the SThM probe to perform non-contact thermal microscopy in UHV [42,43]. Specifically, operating in the constant current STM mode, Kittel *et al.* [42] scanned a room temperature SThM probe (tip radius ~50 nm, Fig. 2-5c [248]) over a cooled (100 K) Au substrate while simultaneously recording the tip thermovoltage. A comparison between the STM topography (Fig. 2-5d) and the thermovoltage (Fig. 2-5e) images reveal that this thermal microscopy technique does indeed give information about the topography of the surface. Moreover, by modeling the tip as a spherical dipole they were able to show that the thermovoltage map (Fig. 2-5d) agrees qualitatively well with the calculated electromagnetic LDOS above the Au sample using a perturbative approach. However, the authors expressed some concerns including the use of a dipole approximation for calculations across a gap size smaller than the tip dimension [42].

More recently, the same group performed some experiments [248] in which NFRHT between a tip (Fig. 2-5c) and a dielectric monolayer of salt (NaCl) deposited on an atomically flat Au substrate was investigated. Significant near-field heat transfer enhancement was observed only when the gap size was smaller than ~6 nm. No probe resistance was explicitly reported so no heat flow was quantified. In terms of tip temperature change, the NFRHT between the Au tip and the monolayer NaCl was measured to be about twice as large as that between the Au tip and Au sample. By using another Cr-coated probe, they checked the material dependence of the measurement and again observed a larger enhancement when the tip is over the NaCl monolayer. The absolute temperature change for the Cr tip in the presence of the NaCl was about 6 times larger than the Au tip. A theoretical explanation of these results remained elusive and the authors suggested that that current theories based on FE may be inadequate to describe the observed phenomena in extremely small gap sizes (1 nm - 10 nm).

A recent tip-plate NFRHT measurement [249] reported heat flow from a planar heated island to a probe. The experimental setup in this work (Fig. 2-5f) was quite different from previous investigations. The probe had a microscale tip made by coating a 30 μm diameter W probe with 2 μm-thick SiO_2 and was maintained at room temperature during the experiment. While the sample was a MEMS device featuring a 840 nm-thick SiO_2 membrane (100×50 μm^2) suspended over a cavity by 600 nm wide, 30 μm long beams. A 2 kΩ Ni resistor was deposited onto the membrane to serve both as a resistive thermometer and a heater capable of heating the membrane to 460 K. When the probe was brought into close proximity to the heated membrane, the membrane tem-

perature decreased as quantified by measuring the resistance change of the thermometer. Measured data of the membrane temperature (Fig. 2-5g) agreed fairly well with the theoretical expectation. A horizontal offset of 160 nm in the data could bring the experiment and theory into better agreement (Fig. 2-5g, inset) and was attributed to the gap size uncertainty. The minimum gap size in this experiment was limited to ~300 nm due to the probe's large radius of curvature, leaving the sub-100 nm range unexplored.

From the above descriptions it is clear that the tip-plate experimental setup, as compared to the plate-plate configuration, offers significant potential in the study and utilization of NFRHT, especially in the extreme near-field with gap sizes around or below 10 nm. However, further work is required to achieve a better understanding of the reported experimental observations and to validate/invalidate the current theories in modeling NFRHT in gap sizes as small as a few nanometers. At last, the NFRHT between dielectric materials in the extreme near-field remains unexplored as the SThM-based technique is inevitably limited to electrically conductive materials.

2.5.3 Thermal near-field spectroscopy

Near-field heat transfer measurements provide insight into the integral effect of the near-field on radiative heat flow. However, heat flow measurements alone cannot lead to direct characterization of the surface modes or the spectral properties of the evanescent field in general. The ability to experimentally probe the spectral nature of thermal radiation in the near-field is critical to understanding and tuning the near-field radiative properties. Such investigations require different experimental techniques than those described previously.

One of the first techniques that enabled probing the thermal near-field was reported by De Wilde *et al.* [41] In this work, the authors described a "thermal radiation scanning tunneling microscope" (TRSTM) that enabled high-resolution imaging of surfaces by using the near-field thermal radiation as an intrinsic source of illumination. The name of the setup emphasizes its analogy to a STM: while a STM measures the electronic LDOS, a TRSTM characterizes the electromagnetic LDOS. The authors placed a sharp W tip in close proximity to the sample of interest (Fig. 2-6a [250]). When the tip was lowered to within several hundred nanometers from the sample (Au patterned on SiC), the evanescent electromagnetic field normally confined near the sample surface was scattered into the far-field. The scattered radiation was then collected using a Cassegrain-type objective and focused onto a low-bandgap mercury-cadmium-telluride

(HgCdTe, or MCT) detector with a spectral range of 6.5 μm - 11.5 μm. A heater positioned beneath the sample enabled raising its temperature by up to ~440 K, resulting in increased intensity of the LDOS which is then encoded in the TRSTM signal. In order to increase the signal-to-noise ratio, the tip was modulated vertically at a frequency of Ω_{tip} (unspecified) around an average distance and the collected signal was later demodulated at Ω_{tip} or $2\Omega_{tip}$. The authors noted a key difference between these two demodulation frequencies, with the Ω_{tip} signal characterizing the averaged LDOS over a larger vertical distance while the $2\Omega_{tip}$ signal capturing the LDOS at a smaller gap. A series of images obtained by TRSTM are shown in Figs. 2-6c to h. The first three (Figs. 2-6c-e) were acquired by scanning the tip over a Au stripe (deposited either on a SiC or SiO_2 substrate) and filtering the signal at 10.9 μm (1 μm bandwidth) in order to improve its temporal coherence [41]. With a demodulation frequency of Ω_{tip}, fringe patterns were observed along the direction of the stripe (Figs.2-6c-d), with the number of fringes being dependent on the stripe width (10 - 30 μm). A more complicated interference pattern was observed at the end of the stripe (Fig. 2-6e) due to the altered boundary condition. These cavity fringes were in good agreement with calculations of the LDOS 3 μm above the Au stripe. Attributed to the SPPs on Au, they were considered to be the first direct evidence of long decay length, spatially coherent thermal radiation in the near-field [41]. Further, the bright and dark portions of Figs. 2-6f-h (demodulated at $2\Omega_{tip}$ to detect the LDOS at ~200 nm distance to the sample) demonstrate the temporal coherence of the thermal emission over the SiC substrate. When an 18 μm wide Au stripe patterned on a SiC substrate was imaged with a 10.9 μm band-pass filter (band size 1 μm), the SiC substrate appeared bright and the stripe appeared dark (Fig. 2-6f). This is expected because theory predicts that SiC supports SPhPs with a wavelength of 10.6 μm (~117 meV, Fig. 2-6b). Changing the band-pass filter to 8 μm (Fig. 2-6g) or imaging the Au stripe on a SiO_2 substrate with the same 10.9 μm filter (Fig. 2-6h) both attenuated the bright signal originally observed from the SiC substrate, suggesting that the contribution to the signal is primarily from the signature SPhPs of SiC. These images thus appear to demonstrate a direct observation of SPhPs on the surface of SiC.

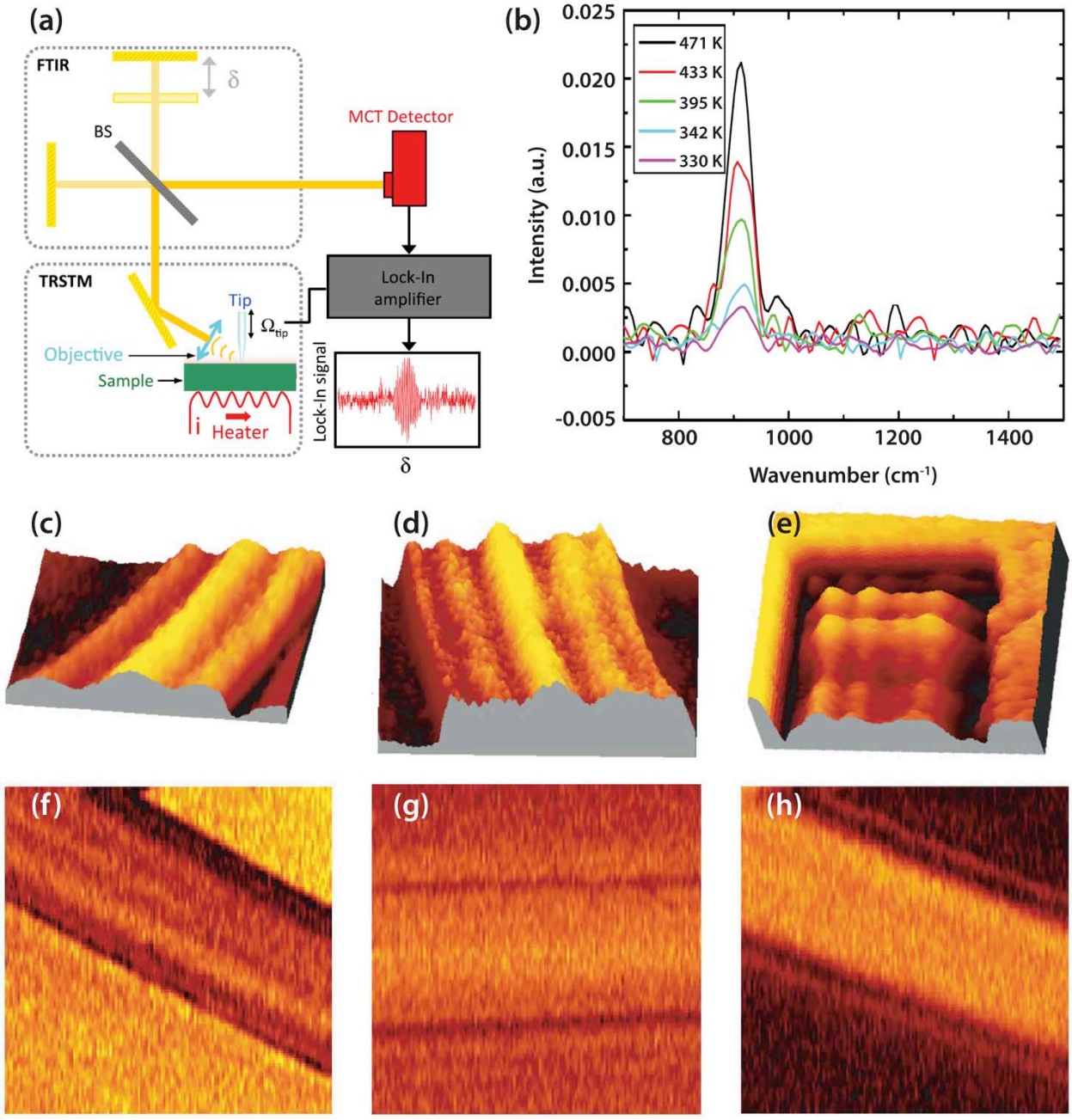

Figure 2-6. Experimental demonstration of temporal and spatial coherence of thermal near-field based on TRSTM. (a) Schematic of the TRSTM and FTIR-based near-field spectroscopy setup [250] with heated sample. (b) Measured near-field thermal emission spectra above SiC at various temperatures [250]. (c)-(h) TRSTM images [41]. (c-e) Images of a Au stripe on SiC substrate obtained at an estimated effective tip-sample distance of 3 μm by scanning over a (c) 16 μm wide segment, (d) 25 μm wide segment, and (e) 30 μm wide end of the stripe. (f)-(h) Images of a Au stripe on a SiC substrate measured with an effective distance of 200 nm. (f) Image for which the signal was band-pass filtered at 10.9 μm (1 μm bandwidth). (g) Image filtered at 8 μm. (h) Image differs from (f) only in the use of SiO_2 as substrate.

The technique described above represents a pioneering first step in the characterization of thermal near-field and the use of it for nanoscale imaging. However, a complete spectroscopic study of near-field thermal radiation was not possible. In order to enable such characterization, Babuty *et al*. [250] recently combined a Fourier transform infrared spectrometer (FTIR) with the previously mentioned TRSTM setup (Fig. 2-6a). A modulated W tip which hits the sample intermittently is used to scatter the thermal near-field into the far field. With a modulation frequency of Ω_{tip} = ~32 Hz and an amplitude of ~100 nm, the near-field spectra of SiC (Fig. 2-6b, demodulation at Ω_{tip}) and SiO_2 were measured with a resolution of 6 cm^{-1} and resonant peaks were observed near 913 cm^{-1} and 1110 cm^{-1}, respectively. No peaks were found when the tip was retracted to ~1 μm above the sample. This is again direct experimental demonstration of the temporal coherence due to surface electromagnetic modes (see also Fig. 7c). Comparing to the theoretically predicted values of 948 cm^{-1} and 1156 cm^{-1}, there is a redshift of ~40 cm^{-1}. Both resonances were also observed to be broader than expected.

However, we note that a similar spectroscopic technique referred to as the thermal infrared near-field spectroscopy (TINS, Fig. 2-7a) was presented by Jones, Raschke and coworkers [251,252] before the work of Babuty *et al*. [250] In TINS, the thermal near-field is also coupled into the far-field by the sharp tip (Si, tip radius measured to be ~50 nm, see Figs. 2-7c-f [252]) of a scanning (AFM) probe, which is then collected by an off-axis parabolic mirror and subsequently analyzed with a FTIR spectrometer (see Fig. 2-7b for the raw and filtered interferograms). However, an important difference from the TRSTM setup is that in TINS the probe tip is heated (resistively, Fig. 2-7c) instead of using a heated sample. Consequently, the tip serves not just as a scatter of the sample near-field, but also a heater (with a temperature up to ~700 K) to locally heat the sample to ~550 K via ballistic conduction through air molecules. In order to improve the sensitivity of this technique, the authors oscillated the AFM probe close to its resonance frequency, enabling the use of a lock-in detection scheme. The near-field of various substrate materials (SiC, SiO_2, and PTFE) were investigated. With a spectral resolution of 25 - 11 cm^{-1}, the TINS spectrum for the SiC sample (Fig. 2-7g) exhibits a strong but broadened resonance near 950 cm^{-1}, the region in which SiC is expected to support SPhPs [252]. Further, redshifts of 5 - 50 cm^{-1} were observed using different probes.

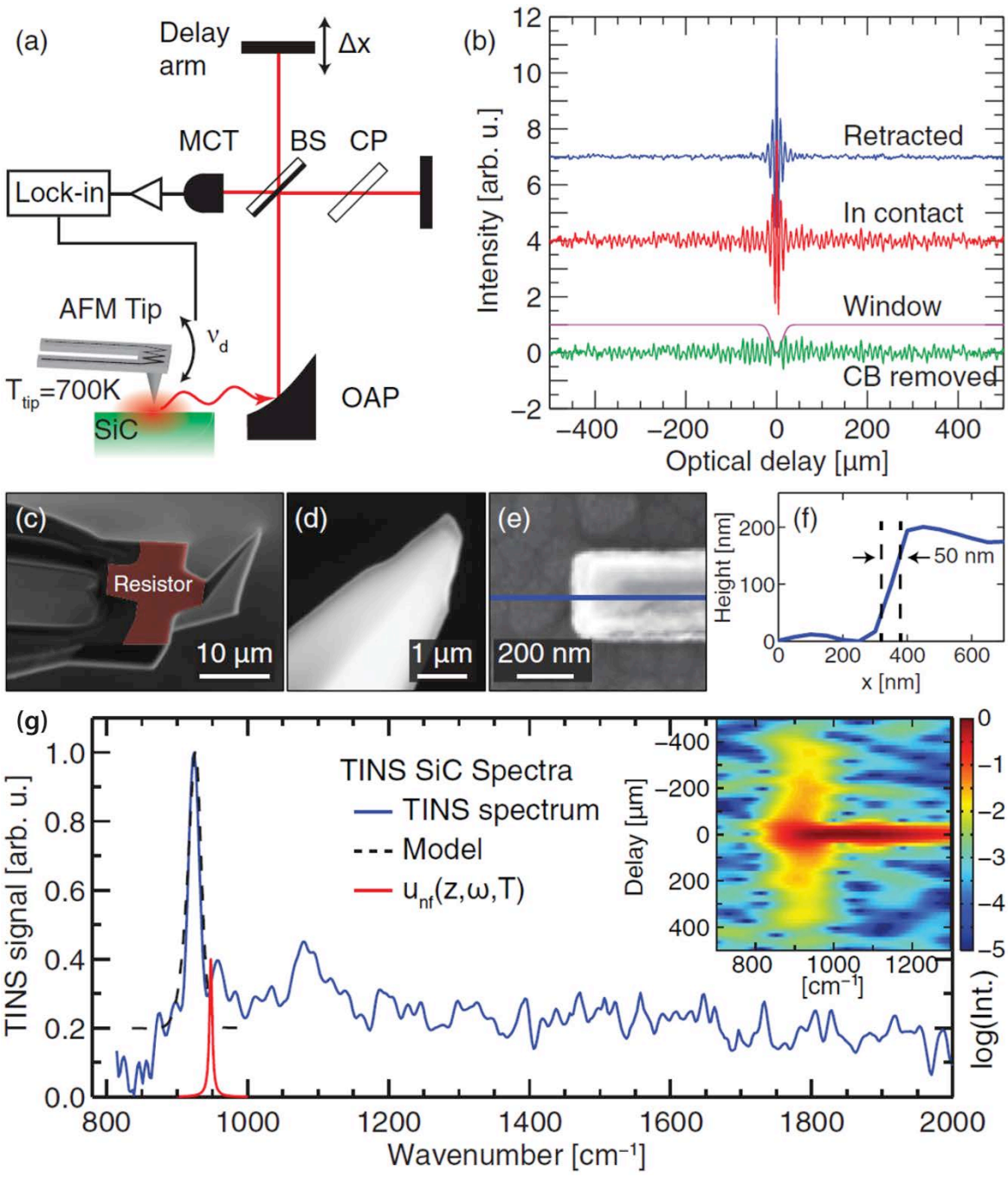

Figure 2-7. Characterization of temporal coherence of thermal near-field using TINS [252]. (a) Schematic of TINS setup featuring heated tip. (b) Interferograms with tip retracted and tip in contact with SiC, and with the center burst removed by a window function. Long-range interference in contact indicates coherent contribution due to the SPhP resonance. (c)-(d) SEM images of the Si cantilever and tip. (e) AFM image of a test structure and a line profile (blue) shown in (f) indicating the tip radius is ~50 nm. (g) Fourier transformed TINS spectra of SiC (solid blue). Fits (dashed black) using finite dipole model. Calculated spectral energy density (solid red, arbitrary unit). Inset:Spectrogram of the in-contact interferogram in (b).

The consistent observations of redshifts [250-254] of the resonant peaks in the measured near-field spectra as compared to the calculated spectral energy density represent a recent topic of concern. Various models have been proposed by the aforementioned research groups. It was suggested that multiple reflections between the sample and tip leads to an effective tip (dipole model) polarizability which can be accounted for with an effective tip radius [250,253]. The disturbance of the sample near-field by the tip was also considered, which was modelled by surrounding the sample with an effective medium whose dielectric function differs from that in air [252]. Further, the contribution of phonon softening in the sample was discussed [251,252].

Apart from TRSTM and TINS which uses heated samples or tips as intrinsic illumination sources, the scattering scanning near-field optical microscopy (s-SNOM) was also used to study the near-field. In order to do so, Zhang *et al.* [255] used an external infrared source to illuminate the system. The authors studied the sample thickness-dependence of the LDOS by measuring with a Si tip over a set of amorphous SiO_2 thin films (thickness 2 - 300 nm) thermally grown on Si. They observed a clear maximum in the spectroscopic signal at 1130 cm^{-1}, which is red shifted by about 20 cm^{-1} from the expected resonance for SiO_2. Further, the amplitude of the maximum noticeably decreased for thinner films. A theoretical calculation modeling the tip as a spherical dipole failed to describe the experimental results accurately. A more robust spheroid model capable of describing the antenna effect better described the data, capturing both the red shifted resonance and the amplitude changes for different film thicknesses.

2.5.4 Sphere-plate

Studying NFRHT between a sphere and a plane represents a compromise between the parallel-plane and tip-plane geometries. The sphere-plane geometry permits relatively larger heat flows than those associated with the tip-plane configuration because of the increased heat transfer area. Further, the use of even modestly large spheres (diameter ~1 μm) enables the use of macroscopic material properties (e.g., dielectric function) when making predictions about NFRHT. Unlike the parallel-plane geometry, measurements using the sphere-plane geometry do not require technically challenging alignment and parallelization of the heat transfer surfaces, so smaller gaps (~10 nm) can be achieved with relative ease. For these reasons, recent experimental work [2,221,222,256-261] exploring some of the more striking predictions of NFRHT theory has focused on the sphere-plane geometry.

An experimental technique for measuring NFRHT between a sphere and a plane was developed in 2008 by Narayanaswamy *et al.* [256] and is illustrated schematically in Fig. 2-8a [222]. In this AFM-based technique, a SiO_2 microsphere (~50 μm diameter) is glued to the tip of a silicon nitride (SiN_x) -Au bimaterial cantilever, which deflects as its temperature changes because of mismatched coefficients of thermal expansion for the SiN_x and Au layers. A low power laser (few mW) was focused on the cantilever to optically heat the cantilever-sphere assembly so a temperature difference can be established between the sphere and a sample (glass microscope slide). Simultaneously, the reflected laser beam from the cantilever surface was monitored using photo-sensitive diodes (PSD) to measure the deflection of the cantilever arising due to temperature changes and/or mechanical forces. When the warm sphere is brought into close proximity to a planar sample at ambient temperature in a vacuum environment (~5×10^{-5} torr), there is a net radiative transfer of heat from the sphere to the sample, resulting in a temperature drop of the cantilever which in turn reduces the bimaterial deflection. This cantilever deflection as a result of the temperature change is then measured using the PSD. The deflection of the cantilever in response to heat flows was independently calibrated [256]. The near-field thermal conductance was reported for gap sizes from 10 μm down to 100 nm, with all the measured values exceeding predictions by the Derjaguin approximation (DA). The authors proposed that for DA to be valid, the near-field contribution has to dominate over that of the far-field which they estimated was true only when the diameter of the sphere is less than ~2 μm, while the sphere they used was much larger in size [256]. In these experiments the gap size was reduced by bringing the substrate towards the sphere in a stepwise fashion with a smallest step size of 100 nm, which represents a limit for the smallest gap size and the gap size uncertainty. The gap size was measured by referencing the displacement of the substrate to the location where the sphere and the substrate make contact, which was indicated by a sudden change in the PSD signal [256].

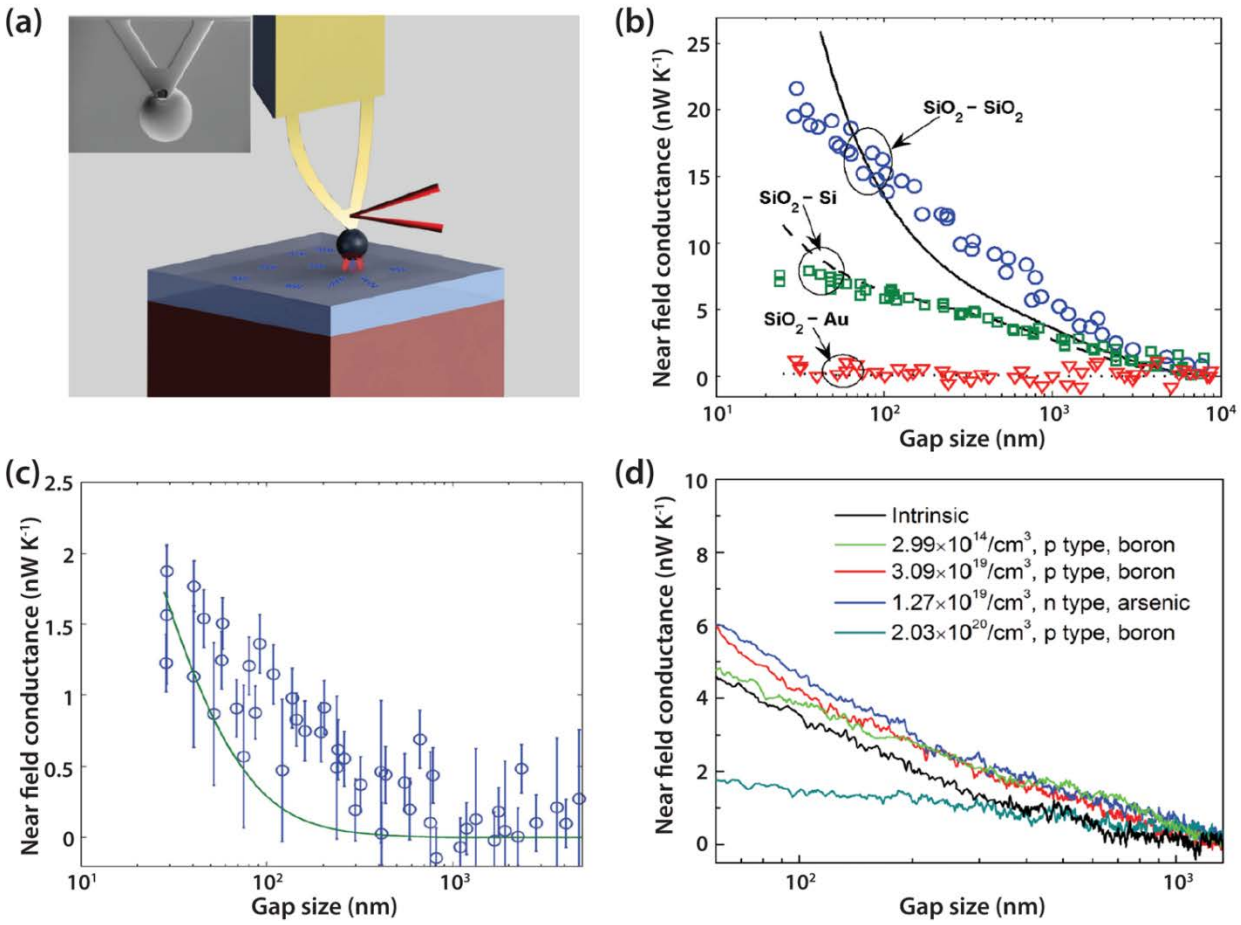

Figure 2-8. Measurements of NFRHT between a sphere and a plane using the bimaterial cantilever-based approach. (a) Schematic of the experimental setup [222]. The same principle was used in other works [256,257,260]. (b) Experimental results[222] for near-field vacuum gap thermal conductance versus gap size measured between a 100 μm diameter silica sphere and a glass slide (blue circles), doped Si surface (green squares), and Au surface (red triangles). Theoretical curves produced using DA are represented for SiO_2-SiO_2 (solid line), SiO_2-Si (dashed line), and SiO_2-Au (dotted line). (c) Experimental results [257] for near-field conductance measured between a 50 μm Au-coated silica sphere and a 100 nm-thick Au film. Experimental data (circles) are plotted alongside a theoretical curve (solid line) obtained using DA. (d) Experimental results [260] for near-field conductance measured between a 100 μm glass sphere and Si substrates of various doping types and concentrations.

Later Shen, Narayanaswamy, and Chen [222] leveraged the same approach to systematically explore the role of SPhPs in mediating the enhanced heat transfer in dielectrics. In these experiments they report a high-resolution (~5 nm) piezoelectric control of the sample position (thus the gap) and presented near-field heat transfer data in a sphere-plane configuration for gap sizes as small as 30 nm. From these NFRHT experiments they inferred (in terms of equivalent heat transfer coefficient based on the DA approach) enhancements as large as three orders of magnitude as

compared to estimates using far-field radiation theory for blackbodies. Specifically, they reported NFRHT measurements between a SiO_2 sphere (50 or 100 μm diameter) and planar surfaces. The planar samples include a glass (nominally SiO_2) slide, a Si ($2.6x10^{19}$ cm^{-3} arsenic-doped) wafer, and Au (1 μm-thick gold on glass slide). The roughness of all three samples was reported to be ~3 – 4 nm. Their results for a 100 μm diameter sphere are shown in Fig. 2-8b. As expected from previous discussions, the near-field conductance between the SiO_2 spheres and the planar SiO_2 substrate is the larger than for all other configurations due to the presence of SPhPs supported by SiO_2. Similar to their previous work, the measured gap-dependence of the near-field conductance does not agree with the DA prediction, which is smaller for gaps over 100 nm but exceeds the measured values for the smallest (tens of nanometers) gaps. The authors again noted that DA may not be always valid. Some near-field enhancement was also observed between the SiO_2 sphere and the Si sample, and the data appears to agree well with the proximity approximation except for gap sizes smaller than ~50 nm. No measurable enhancements in heat transfer between the SiO_2 sphere and the Au plane were observed, which is consistent with theory due to the large mismatch in the near-field spectra of these materials. The gap size was again measured as described above. At last we note that the authors performed a control experiment with very weak laser beam (<1 K temperature difference between the sphere and sample) to determine the effect of proximity forces on the cantilever deflection. More recently, Shen *et al.* [257] explored NFRHT between gold-coated sphere and substrates and the measured results (Fig. 2-8c) compared well with the modified Derjaguin approximation proposed by Sasihithlu and Narayanaswamy [184]. Also, Shi *et al.* [260] demonstrated that the near-field conductance between a SiO_2 sphere and doped Si substrates of different doping types (boron and arsenic) and levels (10^{14} to 10^{20} cm^{-3}) can vary from 2 nW/K to 6 nW/K at a gap of ~60 nm (Fig. 2-8d).

Apart from the above sphere-plate experiments performed in the USA, similar work were conducted in France. In 2009, Rousseau *et al.* [221] performed an experiment between a SiO_2 microsphere (sodalime glass) and a heated SiO_2 (borosilicate) substrate. Their technique is outlined schematically in Fig. 2-9a and differed from that of Shen *et al.* [222] in two important ways. First, the cantilever deflection was measured interferometrically as opposed to using the deflection of a laser beam. Secondly, the substrate was heated to serve as the emitter instead of using a heated sphere. They attached 40 and 22 μm diameter SiO_2 spheres to SiN_x-Au bimaterial cantilevers and measured the total gap thermal conductance as the distance between the spheres and the

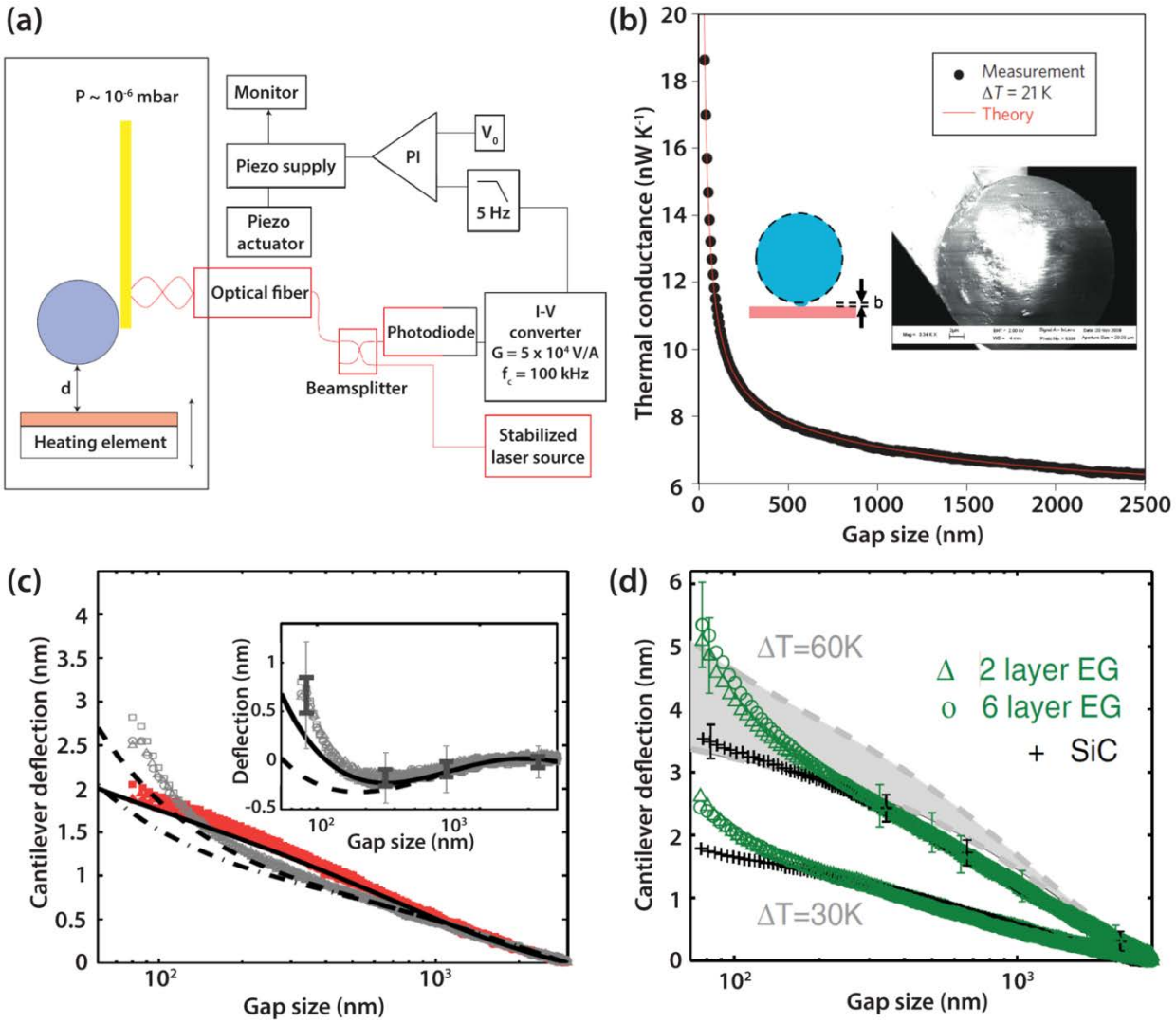

Figure 2-9. Bimaterial cantilever-based measurements of sphere-plane NFRHT using interferometric detection of deflection. (a) Schematic of the setup [221]. The same principle was used in other works [258,259]. (b) Results [221] for vacuum gap thermal conductance versus gap size between a 40 μm diameter sodalime glass sphere and a borosilicate glass substrate. Experimental data (dots) compared to theory (red line). (c) Results[258] for measured cantilever deflection versus gap size for a 40 μm diameter sodalime glass sphere and a VO_2 substrate. Open gray (closed red) symbols correspond to experimental data for VO_2 in the insulating (metallic) phase, obtained as the difference between raw data for ΔT = 30 K and ΔT = 0 K (ΔT = 75 K and ΔT = 50 K). Calculations for the metallic (insulating) phases are plotted as a solid (dashed) black line. Inset: Shows the difference between the insulating and metallic phases. (d) Results [259] for measured beam deflection between a SiO_2 sphere and 2-layer or 6-layer graphene on SiC, and bare SiC. Theory is shown (gray area) for NFRHT between a SiO_2 sphere and a SiC substrate.

planar sample was varied via piezoelectric control of the sample. Their results for the 40 μm sphere are shown in Fig. 2-9b and demonstrate near-field enhancements similar to the results by Shen *et al.* [222] Distinct from the previous work is the observation that their experimental data

agree remarkably well with theoretical expectations based on the Derjaguin approximation. In performing this comparison, a data fitting process was used based on a model with the far-field thermal conductance, the cantilever sensitivity and a gap size shift (which indicates the uncertainty in gap size due to surface roughness) as the parameters. Specifically, the far-field conductance between the glass sphere and sample was estimated via the Stefan-Boltzmann law, with the emissivity of glass taken to be 0.354. The gap size shift was used to account for the large roughness of the spheres (inset of Fig. 2-9b) and was fitted to be ~32 nm, close to the SEM measured roughness of 40 nm for the 40 μm diameter sphere. For the 22 μm diameter sphere, the roughness was as large as 150 nm.Successive papers from Chevrier's group [258,259] demonstrated tunability of NFRHT. In the first publication [258], NFRHT between a 40 μm diameter sodalime glass sphere and a heated VO_2 substrate was investigated. In this study VO_2 was selected for its MIT transition at a critical temperature of ~340 K. In low temperature insulating phase VO_2 substrate supports SPhPs and is expected to enhance heat transfer to the SiO_2 sphere. Indeed, the experiment data confirmed the prediction for gap sizes smaller than 150 nm. Further experiments [259] by the same group investigated additional tuning mechanisms by measuring NFRHT between a SiO_2 sphere and SiC substrates with or without a graphene top layer. They observed an increase in NFRHT in the presence of graphene (Fig. 2-9d) and attributed the enhancement to thermally-excited SPPs on graphene. In both work the proper characterization and subtraction of the gap-dependent force effect from the total cantilever deflection is critical.

The bimaterial cantilever-based approach described above represents a major experimental breakthrough for NFRHT studies. However, it may suffer from two drawbacks: 1) The detection of contact between the sphere and the plane relies on the deflection of the cantilever which is also used to monitor temperature changes via its deflections, and 2) bending of the cantilever due to electrostatic forces between the sphere and planar surface could also result in deflections that can be convolved with the signal arising from temperature variations. Cahill *et al.* [29] recently identified these challenges and called for experimental solutions. Recent work by Song *et al.* [2] aimed to develop a novel experimental platform that can overcome some of these challenges and is described in Chapter 3.

2.6 Concluding Remarks

The past two decades have been marked by an enormous surge in the interest in nanoscale heat conduction (via phonons) which resulted in important insights now enabling the development of nanostructured thermoelectric materials as well as interfacial engineering for thermal management in electronic and photonic devices. Although nanoscale radiative heat transfer (NFRHT) offers a broad range of unique opportunities for both intricate control of heat flow and for the creation of novel energy conversion and information storage devices, research in NFRHT has received considerably less attention. In our opinion, this is primarily due to a lack of suitable experimental tools for systematically probing NFRHT. As described in this chapter this situation is now beginning to change primarily due to the emergence of a new suite of experimental tools that have enabled both the measurement of NFRHT at the nanoscale and the characterization of the electromagnetic states that lead to enhancement of near-field heat transfer. Further, recent years have also witnessed great improvements in the computational tools required to model NFRHT in arbitrary geometries and gap sizes. These advances have led to a variety of predictions of nanoscale radiative heat transfer that hold significant technological promise if systematically understood and leveraged for future applications in thermal management, instrumentation, and energy conversion.

One of the major impediments to experimental progress is the current inability to characterize NFRHT between planar surfaces at gaps as small as a few nanometers or even tens of nanometers in the parallel-plane configuration. If the experimental techniques to probe NFRHT between surfaces can be combined with precisely micro- and nanofabricated planar dielectric, metallic and heterostructured surfaces with nanometer control of gap size, the study of NFRHT could potentially be revolutionized. In fact, such breakthroughs combined with recent advancements in instrumentation and fabrication techniques provide a unique opportunity for realizing the much-desired goal of a detailed understanding of NFRHT. In addition to the above described need for breakthroughs in instrumentation, rapid progress in understanding NFRHT also critically hinges on successfully leveraging recent advances in computational techniques and novel materials. Specifically, it is absolutely critical to create both novel materials and surfaces that are appropriately nanostructured or integrated with suitably chosen 2D materials such as graphene to understand the efficacy of near-field effects for heat transfer, spectral control and energy conver-

sion. If successful, this multi-disciplinary research area could significantly impact future technologies much as far-field radiation is now central to a range of technologies.

Chapter 3

Enhancement of Near-Field Radiative Heat Transfer Using Polar Dielectric Thin Films

Reproduced with permission from reference [2]:

Bai Song*, Yashar Ganjeh*, Seid Sadat*, Dakotah Thompson, Anthony Fiorino, Víctor Fernández-Hurtado, Johannes Feist, Francisco J. Garcia-Vidal, Juan Carlos Cuevas, Pramod Reddy and Edgar Meyhofer, Nature Nanotechnology 10, 253-258, (2015).

3.1 Abstract

Thermal radiative emission from a hot to a cold surface plays an important role in many applications, including energy conversion, thermal management, lithography, data storage, and thermal microscopy [28,41]. Recent studies [221,222,247] on bulk materials have confirmed long-standing theoretical predictions indicating that when the gap between the surfaces is reduced to tens of nanometres, well below the peak wavelength of the blackbody emission spectrum, the radiative heat flux increases by orders of magnitude. However, despite recent attempts [248], whether such enhancements can be obtained with nanoscale dielectric films thinner than the penetration depth of thermal radiation, as suggested by theory, remains experimentally unknown. Here, using a novel experimental platform that leverages picowatt resolution heat-flow calorimetry [262], we experimentally demonstrate a dramatic increase in radiative heat transfer—comparable to that obtained between bulk materials—even for very thin dielectric films (50 - 100 nm) when the spatial separation between the surfaces is comparable to the film thickness. We explain these results by analyzing the spectral characteristics and the mode shapes of surface

phonon polaritons, which dominate near-field radiative heat transport in polar dielectric thin films.

3.2 Introduction

To experimentally study near-field radiative heat transfer (NFRHT) we developed an ultra-sensitive, micro-fabricated calorimetric platform that enables quantitative studies of gap size-dependent heat currents from a spherical hot surface (called emitter) to a planar, colder surface (called receiver) for a broad range of film thicknesses (Fig. 3-1). Understanding NFRHT is key to developing novel technologies such as heat-assisted magnetic recording [45] and lithography [22] as well as near-field based thermal management [56,67,215,249,258]. Despite long-standing theoretical predictions [22,24-26,28,94], only recently measurements from bulk materials using either scanning probes with integrated thermal sensors [247] or bimaterial cantilever-based calorimeters [221,222] have provided experimental support of striking enhancements in radiative heat transfer at the nanoscale. In spite of this important progress one of the most interesting theoretical predictions, which suggests that NFRHT in nanoscale gaps is dramatically enhanced by even nanometre-thick polar dielectric films [26,156,166,188], has remained experimentally untested. Although in a recent experimental report [248] NFRHT was studied between a bare Au-surface and a second Au-surface coated with a monolayer of NaCl, the results were inconclusive and seem to defy theoretical interpretation, in part because an accurate measurement of heat currents could not be carried out.

3.3 Experiments, Results and Analysis

In this work we study the film thickness dependence of NFRHT using the platform shown in Fig. 3-1. We precisely control the gap size between the spherical emitter and the planar receiver from as small as 20 nm to as large as 10 μm using a custom-built nanopositioning platform [4], while simultaneously measuring heat currents between them to obtain the thermal conductance as a function of gap size. Further, contact between the emitter and the receiver is optically monitored (Fig. 3-1a). More specifically, the emitter device (Fig. 3-1a) consists of a suspended silicon region onto which a 53 μm diameter silica (SiO_2) sphere is attached (see Sec. 3.4). The emitter also features a platinum resistance heater-thermometer through which a sinusoidal electric current (f =1 Hz) is supplied to locally modulate the temperature of the suspended region and the sphere at $2f$ (see Fig. S3).

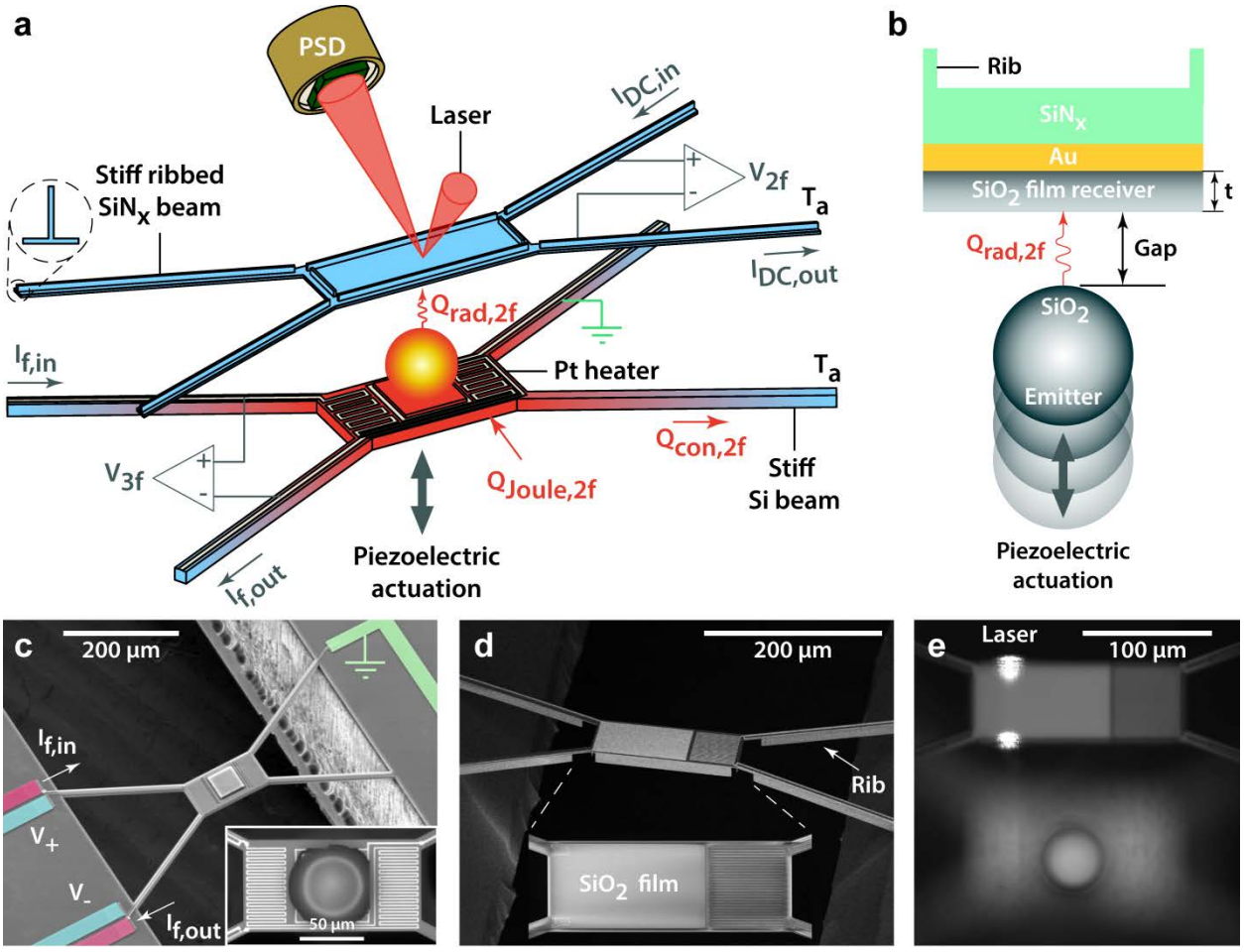

Figure 3-1. Experimental setup and devices. (a) Schematic of the experimental setup. The emitter consists of a suspended silicon platform, with an attached silica sphere, and an integrated electrical heater-thermometer. The receiver is a stiff silicon nitride platform coated with gold and a silica film of suitably chosen thickness. A laser (reflected off the receiver, see also (e)) and a position sensitive detector (PSD) enable optical detection of emitter-receiver contact formation with nanometre resolution. (b) Schematic cross section of the planar receiver region and the spherical silica emitter. The gold layer is ~100 nm thick, the thickness (t) of the SiO_2 film varies from 50 nm to 3 µm for different receiver devices. (c) Scanning electron microscope (SEM) image of the suspended platform and optical image (inset) of the spherical emitter. (d) SEM images of the receiver show ribbed beams and suspended regions. (e) An optical image of the emitter and receiver during alignment. In this image the devices were laterally displaced to enable simultaneous visualization.

The receiver (see Figs. 3-1a, 3-1d) is made from silicon nitride (SiN_x) and is suspended via thin, long beams to achieve a thermal conductance (G_{beams}) of ~2 µW/K. The planar suspended region is coated with SiO_2 layers of varying thickness (50 nm – 3 µm) deposited on a 100 nm thick gold film (Figs. 1b, 1d) and also features an integrated platinum resistance thermometer,

which can resolve small temperature changes (~50 μK, in a 5 mHz bandwidth, when modulated at 2 Hz) enabling detection of small heat currents of ~100 pW (2 μW/K × 50 μK).

This experimental technique makes several improvements for NFRHT measurements over previous bimaterial cantilever-based approaches [221,222] where the deflection of the bimaterial cantilever is potentially affected by both temperature changes and forces (e.g. electrostatic or others like Casimir) posing challenges to the interpretation of experiments [29]. In contrast, in our technique, mechanical motion (detected optically) does not affect temperature measurements that are performed independently with a resistance thermometer. Moreover, we are able to modulate the temperature of the emitter and thus employ lock-in based techniques that enhance [262] the heat flow resolution to below 100 pW.

We began measurements with receivers coated with 3 μm-thick layers of SiO_2, which we expected to behave similar to bulk devices given the comparatively large thickness. After aligning a receiver and emitter at a gap size of ~10 μm in our nanopositioning platform [4] (Fig. 3-1e) we move the nanopositioner into a vacuum chamber ($<10^{-6}$ torr, room temperature) and modulate the emitter temperature (ΔT_{emit}) sinusoidally at 2 Hz with a 10 K amplitude. The resulting radiative heat currents are quantified by measuring the temperature oscillations of the receiver (ΔT_{rec}) using the integrated resistance thermometer. To measure the gap dependence of the heat transfer we step the emitter towards the receiver with a piezoelectric actuator. Nanometre-precise displacements are achieved by monitoring the movement of the actuator with integrated strain gauge sensors under closed-loop feedback control (see Fig. S6). The top panel of Fig. 3-2a shows the displacement of the emitter towards the receiver, which starts with coarser steps (~5 nm) and continues in finer steps (~2.5 nm) close to contact. Throughout the approach the optical signal (middle panel) does not change until contact is established. Finally, the bottom panel depicts the ΔT_{rec}, which increases monotonically until contact is made. Contact is heralded by a sudden change in the optical deflection signal, which occurs concurrently (i.e. within the same 2.5 nm displacement step) with a large jump in ΔT_{rec} due to conduction of heat from the silica sphere to the receiver.

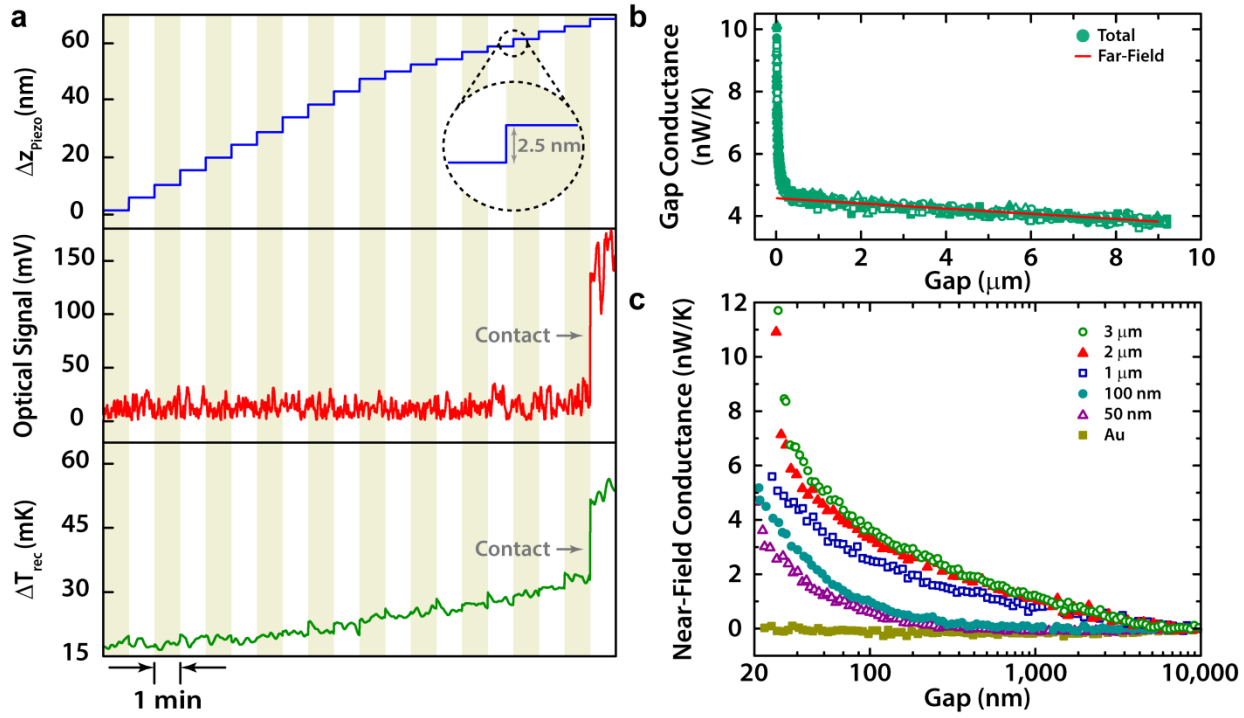

Figure 3-2. Gap dependent near-field thermal conductance of thin films. (a) Simultaneous recording of the displacement of the emitter towards the receiver (top), optical contact signal (middle) and temperature increase in the receiver (bottom). During the final approach piezo displacement steps of ~2.5 nm were used. (b) Contribution of far-field radiation to the radiative thermal conductance across the gap for a representative film (100 nm). The solid red line describes the predicted far field radiation which increases weakly (<1 nW/K) with decreasing gap size due to the associated change in view factor. As expected, the measured data (green symbols) agree well with the far-field prediction for gaps from 1 – 10 μm. **c,** Near-field thermal conductance as a function of film thicknesses. Data for each film thickness represent an average of ~10 different data sets. Please see Fig. S7 for information on the standard deviation of the data.

These experimental data allow us to determine the gap-dependent, radiative thermal conductance as $G_{gap} = G_{beams} \times \Delta T_{rec} / [\Delta T_{emit} - \Delta T_{rec}]$. We obtain the near-field thermal conductance (G_{NF}) at each gap by subtracting the gap-dependent far-field contribution, which is estimated from the thermal conductance at the largest measured gap sizes (~10 μm) and the calculated gap-dependent view factor (Fig. 3-2b and Fig. S7). The estimated G_{NF} for the 3 μm-thick layer of SiO_2 as a function of the gap size is shown in Fig. 3-2c (open circles). Clearly, G_{NF} increases rapidly from ~0 - 12 nW/K as the gap size is reduced to ~20 nm.

To investigate the effect of film thickness on NFRHT we employed receivers coated with a 100 nm-thick SiO_2 layer and measured G_{NF} (Fig. 3-2c, solid circles). Intriguingly, the thermal conductance for these devices remains largely unchanged when the gap is reduced to well below

1 μm, and only begins to increase noticeably with gaps below 300 nm. When the gap size approaches the film thickness, G_{NF} increases rapidly and becomes comparable to that obtained for 3 μm-thick SiO_2 films at gaps less than 100 nm. To better understand the dependence of G_{NF} on the SiO_2 thickness we performed additional experiments with 50 nm, 1 μm and 2 μm-thick layers (Fig. 3-2c, all data points represent an average of ~10 independent measurements). It is clear from these experiments that G_{NF} for each device depends on the thickness of the coating and begins to increase rapidly only when the gap size becomes comparable to the film thickness. We also performed a control experiment where the receiver had only a 100 nm-thick Au film and no SiO_2 coating. The results of this experiment (solid squares in Fig. 3-2c) show that there is no measurable increase in G_{NF} as the gap size is decreased. Taken together, our observations suggest that surface phonon polaritons on the SiO_2 surfaces are responsible for the observed, gap-dependent G_{NF} behaviour.

Next, we evaluated if our experimental findings of NFRHT in thin films are in (quantitative) agreement with theoretical predictions. Towards this end we combined the formalism of fluctuational electrodynamics [263] with a scattering matrix approach [204] (see Sec. 3.5 and Section IIIA of the SI) and calculated the heat transfer coefficient (thermal conductance per unit area, h) between a semi-infinite SiO_2 surface and SiO_2 thin films coated on a semi-infinite Au surface (inset Fig. 3-3a). The computed h values for multilayer structures with different coating thicknesses (50 nm – 3 μm, bulk) show that heat transfer is indeed enhanced when the gap size is reduced and converges to that between bulk SiO_2 surfaces for small (<100 nm) gap sizes (Fig. 3-3a). To establish a direct comparison with our experimental results, we computed the near-field conductance between a 53 μm diameter silica sphere and thin film-coated surfaces (Fig. 3-3b) via the Derjaguin approximation [200] (see Sec. 3.5). The predicted conductances, as a function of gap size and film thickness, are in good overall agreement with our measurements (cf. Figs. 3-2c and 3-3b), although the calculated conductances consistently overestimate the measured thermal conductance. As we demonstrate in section IIIC of the SI and Fig. S12, these deviations are not due to the use of the Derjaguin approximation, which provides accurate results for the NFRHT in our systems in spite of the nanometre scale roughness of the films. Instead, we attribute this comparatively small discrepancy to the inevitable uncertainties associated with the microstructure and optical properties of the integrated thin-films. Overall, the observed agreement between measurements and theoretical predictions suggests that fluctuational electrodynamics successful-

ly captures the key aspects of the gap-dependent NFRHT in these thin film structures and raises the key question: What is the origin of the film thickness dependence of G_{NF}?

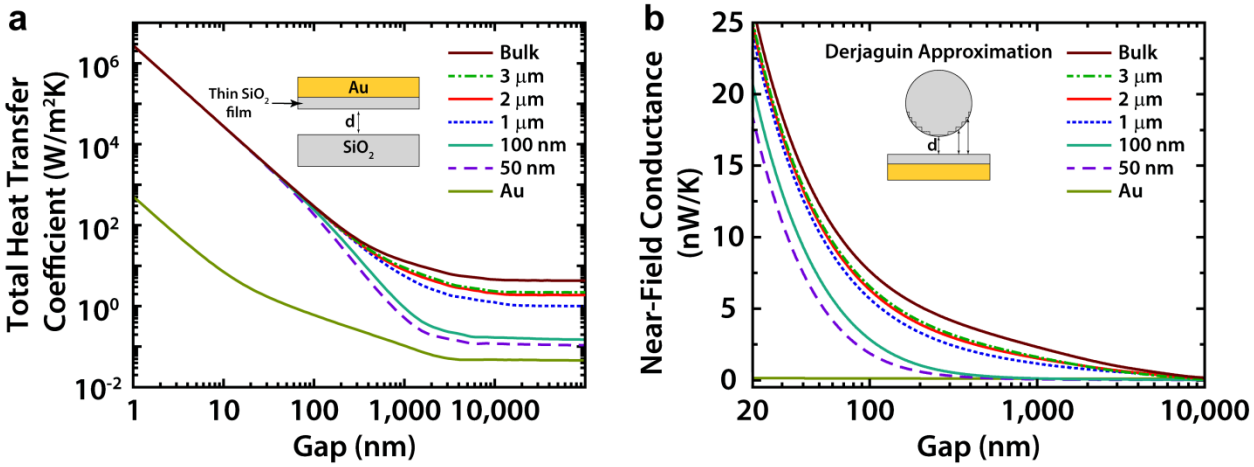

Figure 3-3. Computed heat transfer coefficients. (a) Computed total heat transfer coefficient as a function of the gap size for the multilayer system shown in the inset. This structure comprises of a thick, semi-infinite silica surface separated by a vacuum gap of size d from a silica thin film coating on a semi-infinite Au surface. The different curves correspond to different thicknesses of the silica coating. (b) Calculated near-field conductance as a function of the gap size for the sphere and coated layer system shown in the inset. The sphere has a diameter of 53 μm and SiO_2-Au structure is assumed to be infinite in the transverse directions. The different curves correspond to different values of the coating thickness. These results were obtained using the data in (a) within the Derjaguin approximation (see Sec. 3.5 and SI) and by subtracting the far-field contribution to make a direct comparison with our experiments. In all calculations the temperature was assumed to be 300 K.

In order to elucidate the origin of the thickness dependence of the NFRHT we compare, for two multilayer configurations with 100 nm and 3 μm-thick SiO_2 films and 20 nm gaps, the calculated spectral heat transfer coefficients $h_s(\omega)$ and $h_p(\omega)$ for the transverse electric (TE) and transverse magnetic (TM) modes, respectively (Fig. 3-4a and Fig. S9). It can be seen that TM modes dominate heat transfer at small gap sizes with major contributions from two narrow energy ranges centred around ~0.06 eV and ~0.14 eV. To determine which modes dominate the heat flux we plot in Fig. 3-4b the transmission probability (see Sec. 3.5) for the TM modes, which depends on both the frequency (ω) and the magnitude (k) of the parallel component of the wave vector. Further, we overlay the computed dispersion relationship for cavity surface phonon polaritons (CSPhPs, dashed line) and the light line (solid line) on this plot. It can be seen that the transmission probability is largest in the aforementioned energy ranges (Fig. 3-4b) and occurs for wave vectors that lie to the right of the light line, i.e., for evanescent waves. Further, it can be

seen that these wave vectors either overlap or lie in close vicinity of the dashed line. This strong overlap between the transmission peaks and the dashed dispersion line clearly shows that enhancements of heat transfer are primarily due to CSPhPs supported by the cavity between the SiO_2 layers.

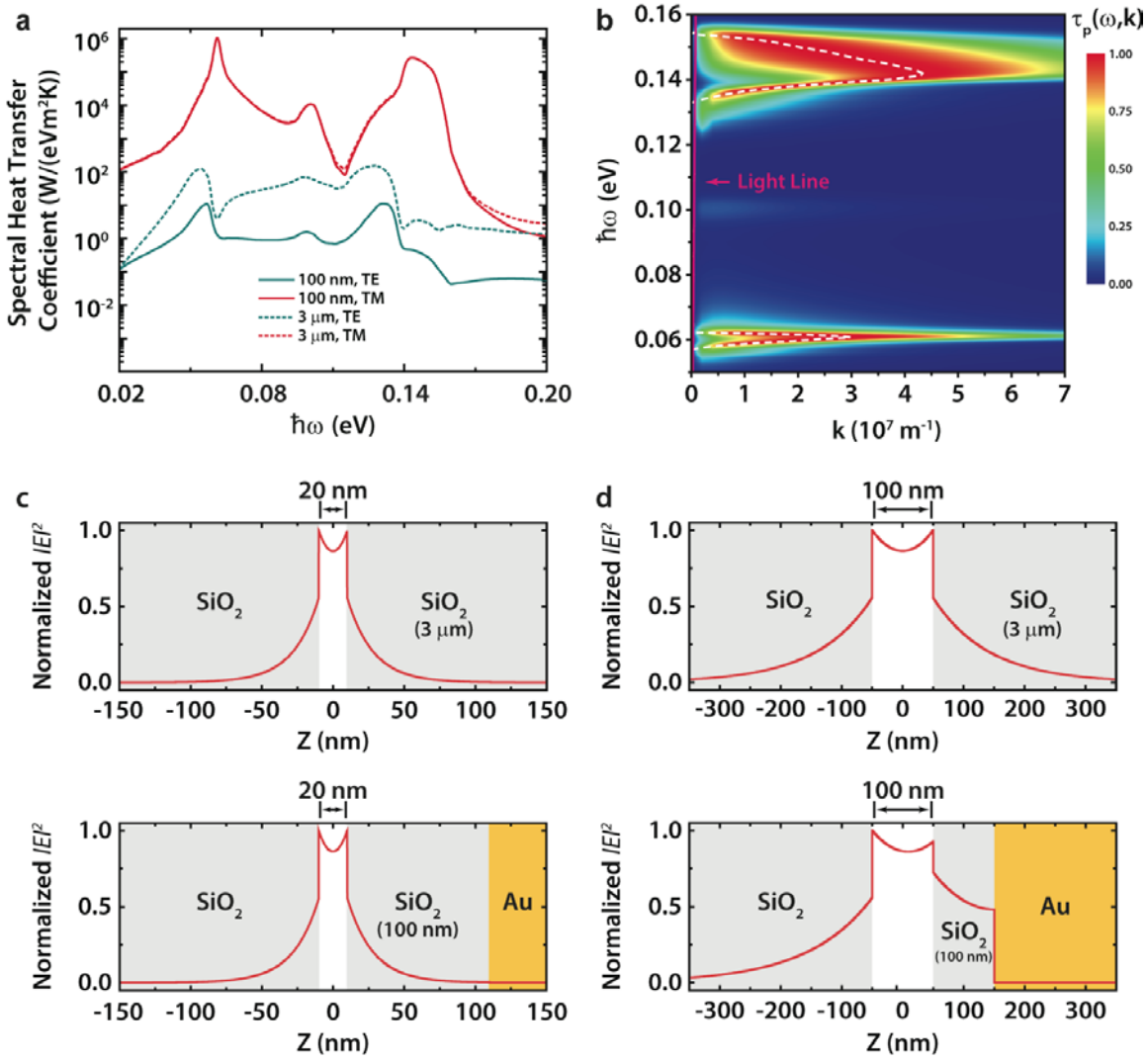

Figure 3-4. Role of surface phonon polaritons in near-field radiative heat transfer. (a) Spectral heat transfer coefficient for TE and TM modes as a function of the radiation energy for the multilayer system of Fig. 3-3a with coating thicknesses t = 100 nm (solid lines) and t = 3 μm (dashed lines) at a gap of 20 nm. The heat transfer is dominated by TM modes and their contribution is almost identical for both thicknesses. (b) The corresponding transmission probability for TM modes, $\tau_p(\omega,k)$, as a function of the radiation energy and the magnitude of the parallel wave vector for t = 100 nm and d = 20 nm. The white dashed line corresponds to the analytical dispersion relation of the cavity surface phonon polaritons (see text), while the pink solid line next to the y-axis corresponds to the light line, i.e. $\omega = kc$. The maxima of the transmission appear largely to the right of the light line and therefore correspond to evanescent waves. (c) Normalized electric field intensity

of a representative cavity surface phonon polariton (CSPhP) mode ($\hbar\omega = 61.2$ meV) for a gap of 20 nm and thicknesses of t = 3 μm (upper panel) and t = 100 nm (lower panel), normalized to peak intensity. The grey regions correspond to SiO_2 and the yellow region represents Au. (d) Same as in (c) but for a gap of 100 nm.

Finally, to clarify the origin of the convergence of NFRHT for thin and thick films at small gap sizes, we note that when the gap size (d) is smaller than the film thickness, the dispersion of CSPhPs (including the dispersions shown in Fig. 3-4b and Figure S11) can be analytically approximated by $k_C = \frac{1}{d}\ln\left(\frac{\varepsilon(\omega)-1}{\varepsilon(\omega)+1}\right)$, where k_C is the complex amplitude of the parallel component of the wave vector and $\varepsilon(\omega)$ is the dielectric function of SiO_2. For the surface modes that dominate the NFRHT, which are evanescent both in the vacuum and inside the silica, the penetration depth (l) of CSPhPs can be approximated by $[2\,\mathrm{Re}\{k_C(\omega)\}]^{-1}$. Thus, we find that $l \approx d$ confirming that the penetration depth is independent of the film thickness and it decreases with decreasing gap size. This fact is illustrated in Fig. 4c, where we compare the normalized electric field intensity of representative CSPhP modes, corresponding to an energy of ~61.2 meV, for two coating thicknesses (100 nm and 3 μm) and a gap of 20 nm. Notice that the mode shapes are almost identical due to the small penetration depths showing that NFRHT in small gaps occurs through identical modes for both thin and thick films and is hence unaffected [120] by film thickness or the presence of a gold layer. On the contrary, when the gap becomes comparable to or larger than the film thickness, the intensity of these modes decays slowly in SiO_2, but drops sharply at the SiO_2-Au interface (lower panel Fig. 3-4d), reducing their ability to contribute to heat transport and leading to a diminished transmission probability (see Fig. S10). Thus, the NFRHT enhancement for thin films, at gaps larger than the film thickness, is significantly smaller than that of thicker films at the same gap size. Finally, we observe that the large reduction in the NFRHT in the absence of a dielectric coating is mainly due to the mismatch between the spectral coefficients of SiO_2 and Au and is consistent with past work [222]. The above analysis provides an intuitive picture which relates NFRHT properties of thin films, which were previously understood [166,168,188] via the penetration depth of radiation, to the shape of the cavity modes. This shows that insights from plasmonics, which enable intricate control of mode shapes, can be employed to tune NFRHT in a variety of nanoscale systems.

3.4 Conclusion

The experimental results and analysis presented here show that NFRHT can be dramatically affected by dielectric films if the gap size is comparable to the film thickness. With our instrumentation we can carry out measurements of heat flow with ~100 pW resolution and precisely control the gap size between the hot and cold surfaces with nanometre resolution. We therefore believe that our setup can probe a variety of other nanoscale radiative heat transport phenomena that remain as yet experimentally unexplored [67,213]. Insights from such studies are critical for optimizing thermal management in future nanoscale devices, and for future near-field based lithography and thermo-photovoltaics [22,79,249].

3.5 Methods

Device geometry of the emitter and receiver: The emitter and receiver devices were fabricated using standard microfabrication processes (see Fig. S1). The suspended region of the emitter devices is connected to the surrounding substrate via beams (Fig. 3-1c) with a relatively large cross-sectional area (10 μm × 10 μm) resulting in a stiff device (~500 N/m) with a thermal conductance of ~180 μW/K. The beams as well as the suspended regions of all receivers incorporate ribs (see Fig. 3-1d) leading to stiff devices (~66 N/m, see Fig. S4 for details) with extremely flat suspended regions. Given the excellent sensitivity of the receiver we are able to resolve heat currents at emitter-receiver distances as large as 10 μm.

Characterization of emitter and receiver: Care was taken to prevent particulate contamination of the device surfaces during fabrication and preparation of the devices for experiments (see Fig. S2). Commercial silica spheres (*Corpuscular Inc.*) were integrated into the devices after cleaning them in de-ionized water to remove particulate contamination. Subsequently, spheres were manually attached to emitter devices using a micro-manipulator and an adhesive (Crystalbond 509) that provides excellent thermal contact. The topography of the devices, the cleanliness of the surfaces and the planarity of the receiver device were all quantified using atomic force mi-

croscopy, dark-field optical microscopy and confocal laser scanning imaging (see Fig. S5). The thermal conductance and the thermal time constant of the emitter and receiver devices were characterized by experiments and/or finite element modelling (see Fig. S3). Section IA of the SI presents details of the fabrication and characterization of the devices.

Optical scheme for detection of contact between emitter and receiver: Accurate detection of contact between the emitter and the receiver is critical for both interpreting our measurements of near-field thermal conductance as well as to precisely determine the gap size between the top of the spherical emitter and the planar surface of the receiver at intermediate steps before contact. We note that the emitter is rigidly mounted on a piezoactuator whose displacement was controlled with ~2.5 nm resolution using strain-gauge sensors (SGS) embedded into the piezoactuator. Please see Fig. S6 for a diagram illustrating the experimental procedure and Fig. 3-2a for experimental data of step sizes.

To accurately detect contact between the emitter and receiver, we sinusoidally modulated the position of the emitter for a short period (~5 s) after each step with an amplitude of ~4 nm at a frequency of 4 kHz. Deflections of the optical beam (at 4 kHz), reflected from the back of the receiver (Fig. 3-1a), were monitored using a photosensitive detector and a lock-in amplifier (time constant 30 ms). As can be seen from Fig. 2b when contact is made the output of the lock-in amplifier suddenly increases due to sinusoidal displacements of the reciever. We note that as the emitter approaches the receiver, there is a point where the emitter is close enough to the receiver to cause “snap-in” due to residual electrostatic charges. Such snap-in is reduced to very small values due to the large stiffness of our devices and due to the incorporation of a grounding loop and plane for the emitter and receiver, respectively, and was experimentally quantified to be <5 nm (see section IC of the SI). In all our experiments we employed a two-stage temperature con-

troller that minimized temperature drift of the nanopositioner to <10 mK over the period of the experiment.

Computational Techniques: NFRHT was computed within the framework of fluctuational electrodynamics[263]. The electromagnetic properties of the different materials were described via local frequency-dependent dielectric functions. The dielectric functions of SiO_2 and Au were obtained from previous works (Ref. 42 of the SI). The dispersion relations of the surface phonon polaritons and their electric field profiles were computed with a scattering matrix formalism [204]. The heat transfer coefficient, *h*, was computed from the following expression [166]:

$$h = \int_0^\infty \frac{d\omega}{4\pi^2} \frac{\partial[\hbar\omega / (e^{\hbar\omega/k_B T} - 1)]}{\partial T} \int_0^\infty dk k \left[\tau_s(\omega, k) + \tau_p(\omega, k) \right], \tag{3-1}$$

where *T* is the temperature, ω is the radiation frequency, *k* is the magnitude of the wave vector component parallel to the layer planes, and τ_s and τ_p are the transmission probabilities for TE and TM modes, respectively, which depend on the Fresnel coefficients of the interfaces (see section IIA of the SI). The near-field conductance between the silica sphere and the thin film-coated surface was computed via the Derjaguin approximation [200] (see inset of Fig. 3-3b and Fig. S8) in which the sphere was approximated by a series of annuli and the thermal conductance between each annulus and the corresponding region of the thin film was computed from the data in Fig. 3-3a and summed together. Further, the far-field contribution was subtracted (see section IIIA of the SI) to obtain the near-field conductance shown in Fig. 3-3b. Finally, we note that in section IIIC of the SI we demonstrate that the Derjaguin approximation provides accurate results for the NFRHT in our system.

Chapter 4

Probing Radiative Heat Transfer in the Extreme Near-Field

Reproduced with permission from reference [3]:

Kyeongtae Kim*, Bai Song*, Víctor Fernández-Hurtado*, Woochul Lee, Wonho Jeong, Longji Cui, Dakotah Thompson, Johannes Feist, M. T. Homer Reid, Francisco J. García Vidal, Juan Carlos Cuevas, Edgar Meyhofer and Pramod Reddy, Nature, in press, (2015).

4.1 Abstract

Radiative transfer of energy at the nanometer length scale is of great importance to a variety of novel technologies including heat-assisted magnetic recording [45], near-field thermophotovoltaics [26] and lithography [22]. While experimental advances have enabled elucidation of near-field radiative heat transfer in gaps as small as 20 to 30 nm [2,221,222], quantitative analysis in the extreme near-field (<10 nm) has been greatly limited by experimental challenges. Moreover, first pioneering measurements [247,248] reported results that differ from theoretical predictions by orders of magnitude. Here, we employ custom-fabricated scanning probes with embedded thermocouples [264,265], in conjunction with novel microdevices capable of periodic temperature modulation, to quantitatively examine this crucial controversy. For our experiments we deposited suitably chosen metal or dielectric layers on the scanning probes and microdevices, enabling direct study of extreme near-field radiation between silica–silica, silicon nitride–silicon nitride and gold–gold surfaces to reveal dramatic, gap size-dependent enhancements of radiative heat transfer. Furthermore, our state–of–the–art calculations of radiative heat transfer, performed within the theoretical framework of fluctuational electrodynamics, are in excellent agreement with our experimental results providing unambiguous evidence that confirms the validity of this

theory [19,24,108] for modeling radiative heat transfer in the extreme near-field. This work lays the foundations required for the rational design of novel technologies that leverage nanoscale thermal radiative heat transfer.

4.2 Introduction

Radiative heat transfer in the far-field [11], *i.e.* at gap sizes larger than Wien's wavelength (~10 μm at room temperature), is well established, while near-field radiative heat transfer (NFRHT), where the gap sizes are smaller than Wien's wavelength, remains comparatively poorly understood [2]. Over the last decade a series of technical advances have enabled experiments [2,221,222] for gap sizes as small as 20 nm to study NFRHT and broadly verify the validity of a theoretical framework called—fluctuational electrodynamics [19,20,94,257]—for modeling NFRHT. In stark contrast, recent experiments [247,248] of extreme near-field radiative heat transfer (eNFRHT) with single-digit nanometer gap sizes between gold (Au) surfaces have questioned the validity of fluctuational electrodynamics and have raised the question of whether additional mechanisms, even of non-radiative origin such as phonon tunneling [266], could dominate the heat transfer in this regime. In addition, some newer computational eNFRHT studies [267] on dielectrics have suggested that the local form of fluctuational electrodynamics, where one assumes the dielectric properties of the media to be local in space, is inadequate for modeling eNFRHT. Yet other computations [268] on dielectrics have asserted that such non-local effects are irrelevant even for gap sizes as small as 1 nm. The resulting controversy is of great concern because understanding eNFRHT is critical for the development of a range of novel technologies [22,26,45]. Here, we present experimental and computational results that both demonstrate dramatic increases in heat fluxes in the extreme near-field and establish the validity of fluctuational electrodynamics for modeling/predicting eNFRHT for dielectric as well as metal surfaces in gap sizes as small as a few nanometers.

4.3 Experiments, Results and Analysis

Experimental elucidation of radiative heat transfer across few-nanometer sized gaps is exceedingly difficult due to numerous technical challenges in creating and stably maintaining such gaps while simultaneously measuring minute (pW) heat currents across them. One key innovation used in this work to overcome the technical challenges was to leverage highly sensitive, custom-fabricated probes with embedded Au-Cr thermocouples (Fig. 4-1a, b & c), called scanning

thermal microscopy (SThM) probes [264]. The SThM probes were fabricated by deposition of multiple metal and dielectric layers to create a nanoscopically small Au-Cr thermocouple at the very end of the tip. Our probes were optimized to have both a high thermal resistance [269] (R_P ~10^6 K/W) and stiffness [264] (>4 N/m), and were coated with a desired dielectric (silica (SiO_2), silicon nitride (SiN)) or metal (Au) layer. The resulting probes have tip diameters ranging from 350 nm – 900 nm (for details see Fig. 4-1b and Figs. S1 to S3 in the supplementary information (SI)).

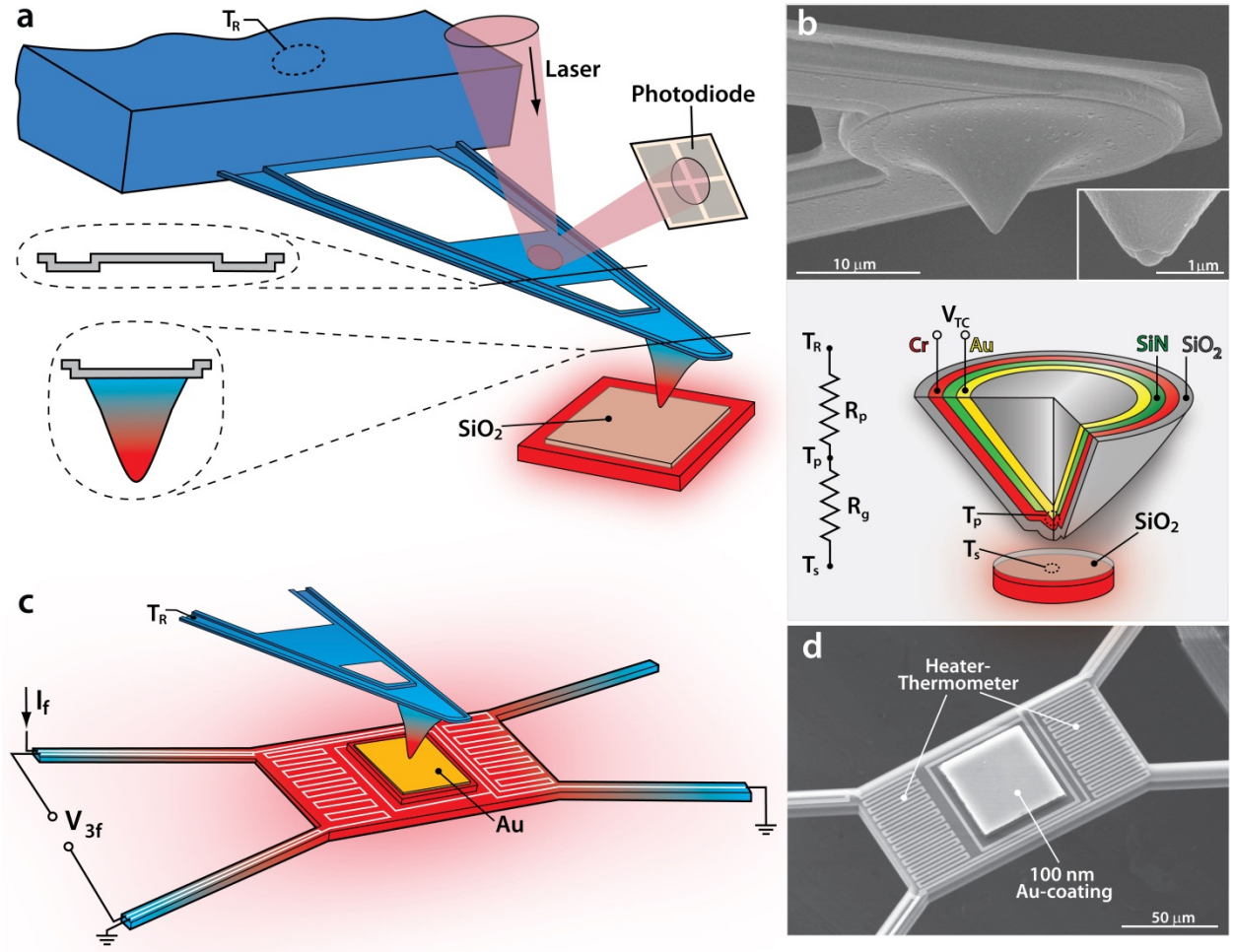

Figure 4-1. Experimental setup and Scanning Electron Microscope (SEM) images of SThM probes and suspended microdevices. (a) Schematic of the experimental setup where a SThM probe is in close proximity to a heated substrate (inset shows the cross-section of the SThM probe). The scenario for SiO_2 measurements is shown (the coating on the substrate is replaced with SiN and Au in other experiments). (b) SEM image (top panel) of a SThM probe. The inset shows a SEM image of the hemispherical probe tip, which features an embedded Au-Cr thermocouple. The bottom panel shows a schematic cross-section for a SiO_2-coated probe employed in SiO_2 measurements. For SiN and Au measurements the outer SiO_2 coating is appropriately substituted as explained in the SI. A

resistance network that describes the thermal resistance of the probe (R_P) and the vacuum gap ($R_g = (G_{eNFRHT})^{-1}$) as well as the temperatures of substrate (T_S), tip (T_P) and reservoir (T_R) is also shown. (c) Schematic showing the measurement scheme employed for high resolution eNFRHT measurements of Au-Au. The amplitude of the supplied sinusoidal electric current is I_f, the sinusoidal temperature oscillations at $2f$ are related to the voltage output V_{3f}. (d) SEM image of the suspended microdevice featuring the central region coated with Au and a serpentine Pt heater-thermometer.

The basic strategy for quantifying NFRHT is to record the tip temperature, via the embedded nanoscale thermocouple, which rises in proportion to the radiative heat flow when the tip is displaced towards a heated substrate. In order to eliminate conductive and convective heat transfer and to remove any water adsorbed to the surfaces, all measurements were performed in ultra-high vacuum (UHV) using a modified scanning probe microscope (RHK UHV 7500) housed in an ultra-low-noise facility (see SI). In performing the measurements the substrate is heated to an elevated temperature (T_S = 425 K) while the SThM probe, mounted in the scanner of the scanning probe microscope, is connected to a thermal reservoir maintained at a temperature T_R = 310 K. The spatial separation between the probe and the substrate is reduced at a constant rate of 0.5 nm/s from a gap size of 50 nm until probe-substrate contact. During this process the temperature difference between the tip (T_P) and the reservoir (T_R), $\Delta T_P = T_P - T_R$, is monitored (see Sec. 4.5) via the embedded thermocouple while the deflection of the cantilever is concurrently measured optically via an incident laser (Fig. 4-1a).

A typical deflection trace for a SiO_2-coated tip approaching a SiO_2-coated surface is shown in Fig. 4-2a. From the deflection trace it is apparent that the gap size can be controllably reduced to values as small as ~2 nm, below which the tip rapidly "snaps" towards the substrate and makes contact (see SI). This instability is created by attractive forces between the tip and the substrate that arise due to Casimir and/or electrostatic forces. Figure 4-2a shows the simultaneously measured ΔT_P, which represents the sudden increase in temperature that occurs when the tip "snaps" into the substrate. This rapid increase in tip temperature (~2 K) upon mechanical contact is due to heat conduction, via the solid-solid contact, from the hot substrate (425 K) to the tip of the SThM probe whose temperature is ~400 K (heating by the incident laser results in an elevated temperature).

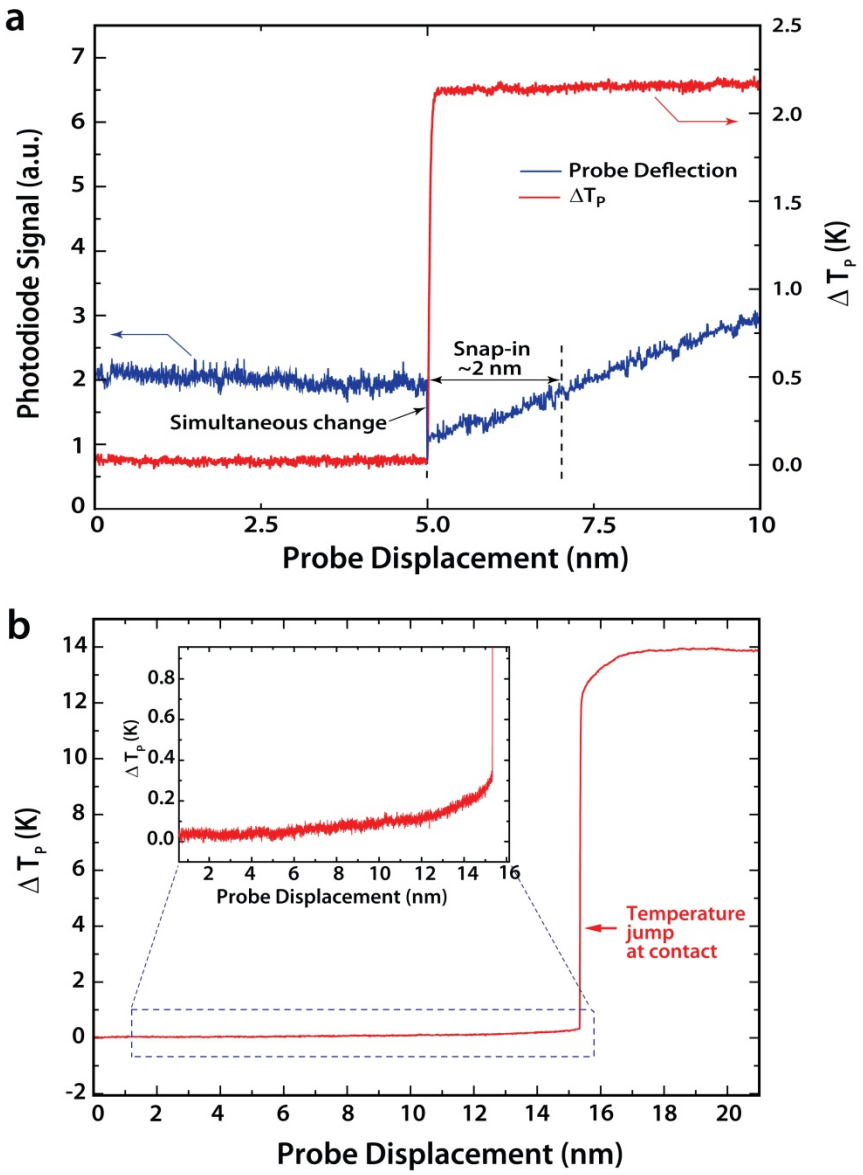

Figure 4-2. Detection of mechanical contact from deflection and temperature signals. (a) Data from an experiment where a SiO_2-coated probe at about 400 K (heated by incident laser) is displaced towards a heated SiO_2 substrate at 425 K. The deflection of the scanning probe (blue) and rise in temperature of probe, ΔT_P (red), are shown. The sudden decrease in the deflection signal due to snap-in coincides with a simultaneous increase in the tip temperature due to conduction of heat from the hot substrate to the cold tip, clearly showing that contact can be readily detected by the large temperature jump. The snap-in distance is seen to be ~2 nm. (b) Measured ΔT_P when an unheated probe (310 K, laser turned off) is displaced towards the substrate. A sudden increase in the tip temperature is seen when the cold tip contacts the substrate. Inset shows an increase in the tip temperature due to eNFRHT.

The tight temporal correlation between the mechanical snap-in and the temperature jump of the probe makes it possible to identify tip-substrate contact solely based on temperature signals.

In Fig. 4-2b the recorded tip temperature is shown as a probe approaches a heated substrate with the laser beam turned off. The recorded temperature signals with and without laser tracking are basically identical (Fig. 4-2a & b), except that the magnitude of the jump reflects the tip-substrate temperature difference with and without laser excitation. Thus, mechanical contact can be readily detected from the robust temperature jump without laser excitation, thereby avoiding probe heating and laser interference effects. Therefore, we performed all experiments by first estimating the snap-in distance using the optical scheme and subsequently turning the laser off to perform eNFRHT measurements (see SI for the measurement of gap size and snap-in distance).

To determine the gap (d) dependent near-field radiative conductance (G_{eNFRHT}) we measured ΔT_P and directly estimated G_{eNFRHT} from $G_{eNFRHT}(d) = \Delta T_P / [R_P \times (T_S - T_R - \Delta T_P)]$, where R_P is the thermal resistance of the probe, which was experimentally determined as described in the SI (Fig. S7) to be 1.6×10^6 K/W, 1.3×10^6 K/W for the SiO_2 and SiN coated probes, respectively. The measured conductance of the gaps for SiO_2 and SiN surfaces is shown in Fig. 4-3a and b, respectively. It can be seen that G_{eNFRHT} increases monotonically until the probe snaps into contact (gap size at snap-in is ~2 nm for both SiO_2 and SiN measurements, see SI, Fig. S6). Further, it can be seen that the eNFRHT is larger for experiments performed with SiO_2. These measurements represent the first observation of eNFRHT in single-digit nanometer-sized gaps between dielectric surfaces. We compared these results to our computational predictions based on fluctuational electrodynamics, assuming local-dielectric properties (see details below), and found very good agreement (solid lines in Fig. 4-3a & b).

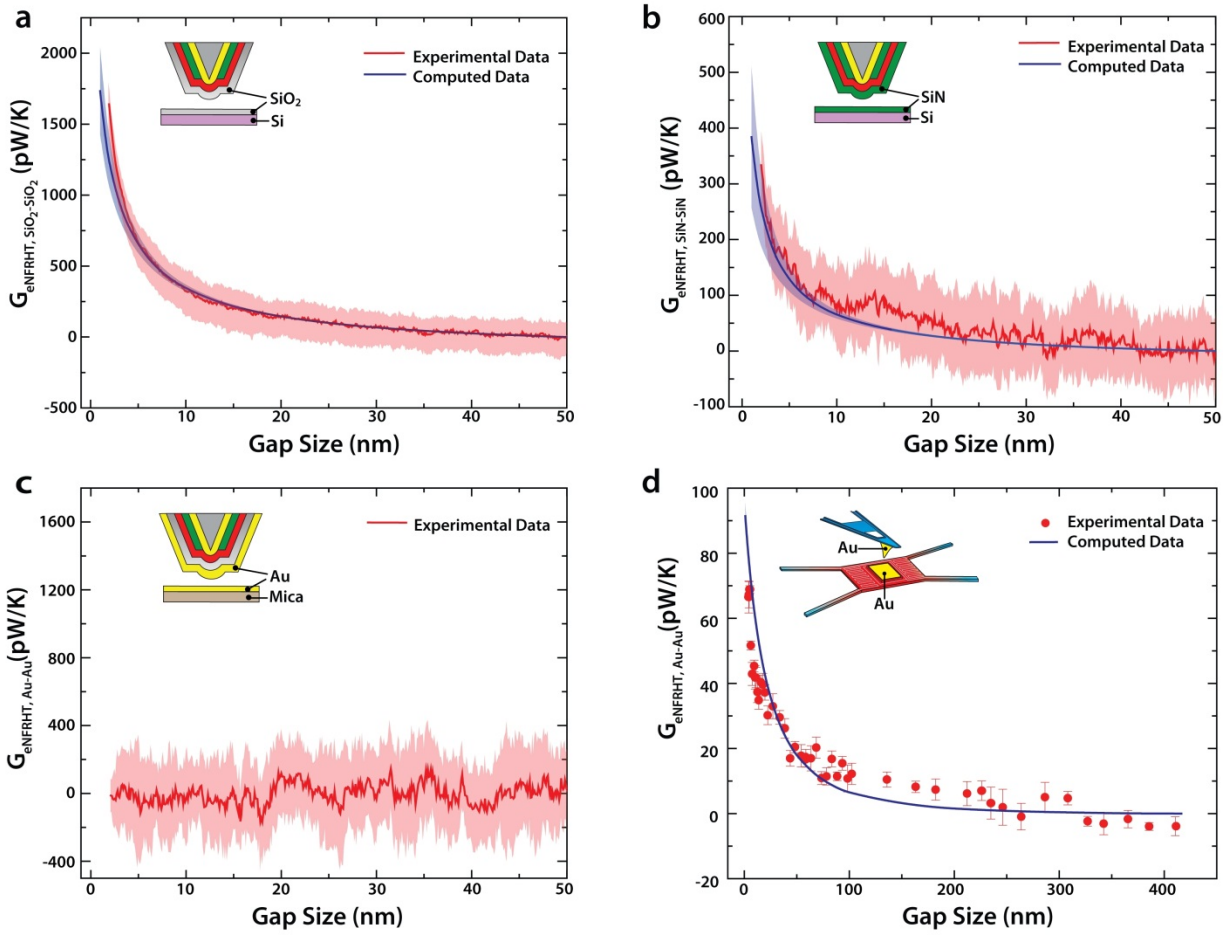

Figure 4-3. Measured extreme near-field thermal conductances for dielectric and metal surfaces. (a) Measured radiative conductance between a SiO_2-coated probe (310 K) and a SiO_2 substrate at 425 K. The red solid line shows the average conductance from 15 independent measurements, the light red band represents the standard deviation. The blue solid line shows the average of the computed radiative conductance for 15 different tips with stochastically chosen roughness profiles (RMS roughness ~10 nm) and a tip diameter (450 nm) obtained from SEM images of the probe. The blue shaded region represents the standard deviation in the calculated data. (b) & (c) same as (a), but for SiN-SiN and for Au-Au, respectively. Tip diameter is 350 nm for the SiN coated tip. Computed results not included for Au-Au. (d) Near-field conductance from experiments with a Au-coated probe and a suspended microdevice. Red dots represent the mean from 10 different measurements (temperature periodically modulated at 18 Hz), whereas the error bars represent the standard deviation. The blue solid line represents the computed conductance (tip diameter 900 nm).

The remarkable agreement between eNFRHT measurements and computational predictions raises important questions with regards to recent experiments [247] of eNFRHT between Au surfaces, which suggested strong disagreements (~500-fold) between predictions of fluctuational electrodynamics and experiments. Is the good agreement reported above unique to eNFRHT between polar dielectric materials? In order to unambiguously answer this question we performed

additional eNFRHT measurements with Au-coated probes and substrates. The measured conductance in these experiments is shown in Fig. 4-3c. It can be seen that the measured G_{eNFRHT} with decreasing gap size remains comparable to the noise floor of ~220 pW/K for Au-coated probes at an applied temperature differential of ~115 K (see SI) and is much smaller than that observed for polar dielectrics. These measurements set an upper bound of ~250 pW/K for G_{eNFRHT} in our Au-Au experiments. This result is particularly surprising because previous studies that employed probes with smaller diameters and thermal resistances [43,247] (23–54 × 10^3 K/W & 10^6 K/W, implying a lower sensitivity than our probes) reported conductances >40 nW/K, which are at least two orders of magnitude larger than conductances measured by us and predicted by theory.

To unequivocally resolve this contradiction we needed to dramatically improve the resolution of our measurements. This was accomplished by employing a novel microdevice (see Fig. 4-1c-d and Figs. S4, S5, S9 & S10 of the SI for details of device fabrication and characterization) that features a suspended island whose temperature can be readily modulated at f = 18 Hz (see Methods). Sinusoidal electric currents (9 Hz) supplied to the embedded electrical heater resulted in sinusoidal temperature oscillations at the second harmonic with amplitude ($\Delta T_{S,f=18Hz}$) that was accurately measured using a lock-in technique (see Sec. 4.5 and refs. [2,262]). To characterize eNFRHT we positioned a Au-coated SThM probe (30 nm Au thickness) in close proximity to the surface of the microfabricated device, which features a suspended region that is 50 × 50 μm large and was coated with 100 nm of Au. The amplitude of temperature modulation of the probe $\Delta T_{P,f=18Hz}$, due to eNFRHT, was measured at various gap sizes (see Sec. 4.5) in a bandwidth of 0.78 mHz. Given the low noise in this bandwidth it was possible to resolve temperature changes as small as ~20 μK, which corresponds to a conductance noise floor of ~6 pW/K, when $\Delta T_{S,f=18Hz}$ is 5 K (see SI for details of noise characterization). The measured $\Delta T_{P,f=18Hz}$ were used to estimate G_{eNFRHT} (Fig. 3d) via: $G_{eNFRHT}(d) = \Delta T_{P,f=18Hz} / [R_{P,\mathrm{Au}} \times (\Delta T_{S,f=18Hz} - \Delta T_{P,f=18Hz})]$, where $R_{P,\mathrm{Au}}$ = 0.7 × 10^6 K/W is the thermal resistance of the Au-coated probe (see SI, Fig. S7). The smallest gap size at which measurements could be accomplished is ~3 nm and is limited by both snap-in and deflections of the microdevice due to periodic thermal expansion resulting from bimaterial effects (see SI Fig. S11). The measured G_{eNFRHT} (Fig. 3d) is indeed much smaller than that obtained with SiO_2 (Fig. 4-3a) and SiN (Fig. 4-3b) films. In contrast to previous experi-

ments[247], our measured G_{eNFRHT} for Au-Au surfaces is in excellent agreement with the predictions of fluctuational electrodynamics (solid line in Fig. 4-3d).

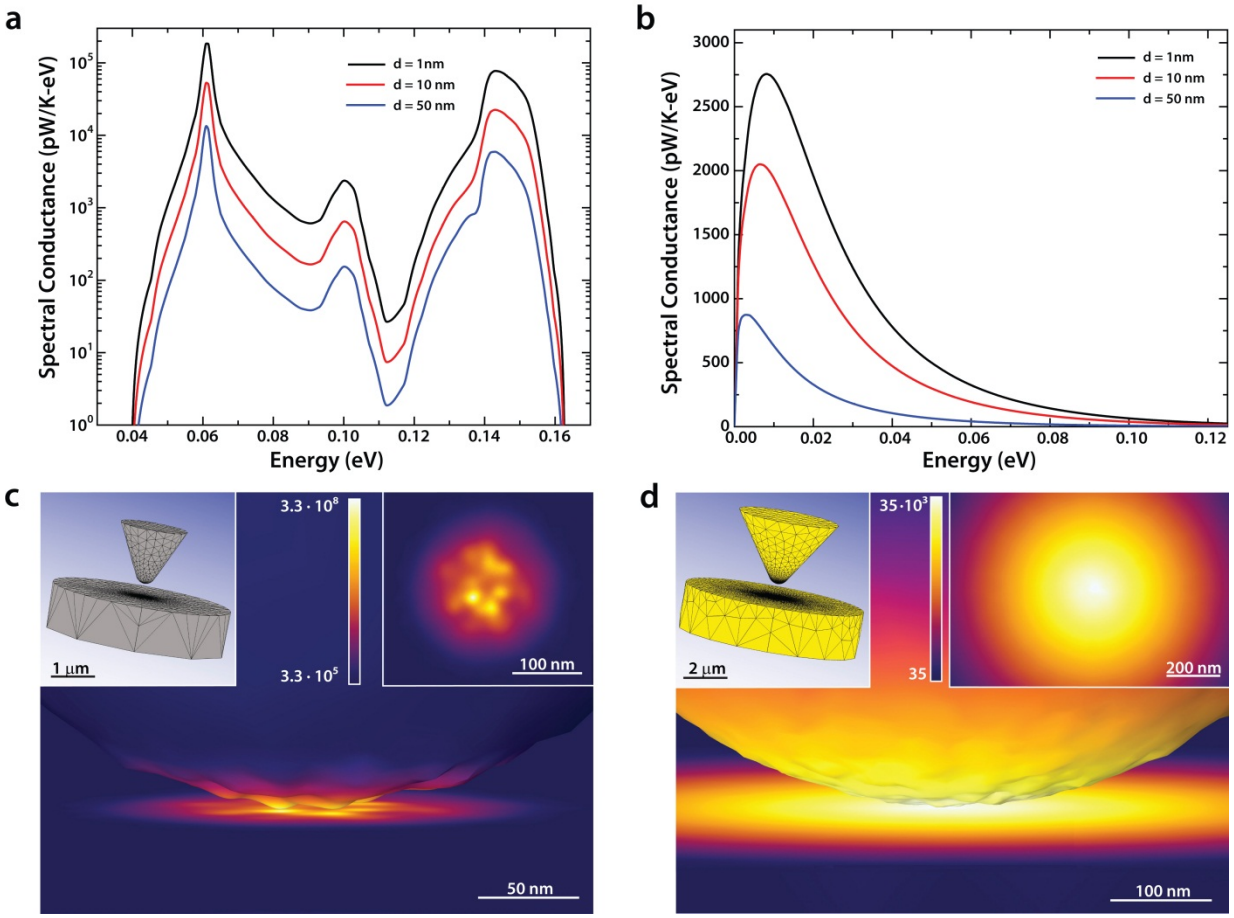

Figure 4-4. Spectral conductance and spatial distribution of the Poynting flux. (a) Spectral conductance as a function of energy for a SiO_2 tip-sample geometry for three different gap sizes. The tip diameter is 450 nm, and the reservoir temperatures are 310 K for the tip and 425 K for the substrate. Notice the logarithmic scale in the vertical axis. (b) The same as in panel **a**, but for Au. In this case, the tip radius is 450 nm, and the tip and substrate temperatures are 300 K and 301 K, respectively. (c) Surface-contour plot showing the spatial distribution of Poynting-flux pattern on the surface of the bodies for the SiO_2 tip-substrate geometry of panel (a) with a gap of 1 nm. The colour scale is in units of $W/(K \cdot eV \cdot m^2)$ and the plot was computed at an energy of 61 meV, which corresponds to the maximum of the spectral conductance. The right inset shows the corresponding surface heat flux on the substrate, while the left inset displays the whole tip-sample geometry simulated including the mesh used in the calculations. (d) The same as in panel (c), but for Au. In this case the surface-contour plot was computed at 9 meV, the maximum of the spectral conductance.

To obtain insight into our experimental results we employed a fluctuating-surface-current formulation of the radiative heat transfer problem [108,212] combined with the boundary element method, as implemented by us in the SCUFF-EM solver [270]. This allows NFRHT calcu-

lations between bodies of arbitrary shape and provides numerically exact results within the framework of fluctuational electrodynamics in the local approximation [108,212]. To accurately simulate our experiments, we considered the tip-substrate geometries shown in the left insets of Figs. 4-4c-d. Here, the tip has a conical shape and ends in a spherical cap whose radius was obtained from SEM images of the probes (see Figs. S1 to S3). In our simulations, the dimensions of both the conical part of the probe and the substrate were chosen sufficiently large to avoid finite-size effects. In order to maintain high fidelity to the experimental conditions, we also accounted for the small roughness of our probes by including random Gaussian-correlated noise in the tip profile (Fig. 4-4c-d). More precisely, the maximum protrusion height on the tip and the correlation length between protrusions were chosen to be 10 nm and 17 nm, respectively, based on the surface characteristics observed in the SEM images (Figs. S1-S3). We investigated the effect of surface roughness by computing G_{eNFRHT} for every material from 15 different tip-substrate ensembles with roughness profiles generated as described above. The computational results for the different materials are presented in Figs. 4-3a, b & d. As pointed out earlier we indeed find very good agreement between computation and experiment without any adjustable parameters.

To elucidate the underlying physical mechanism and explain the differences in eNFRHT between different material combinations, we computed the spectral conductance (heat conductance per unit of energy) for several gap sizes as shown in Figs. 4-4a-b for SiO_2 and Au, respectively (see Fig. S14 for SiN results). In Fig. 4-4a, one can see that the dominant contributions to the spectral conductance of SiO_2 come from two narrow energy ranges centred around ~0.06 eV and ~0.14 eV, which correspond to the energies of the transverse optical phonons of SiO_2. This strongly suggests that for SiO_2 eNFRHT is dominated by surface phonon polaritons (SPhPs), as previously found for larger gaps [2]. In turn, this explains the dramatic decrease in heat transfer as the gap size increases, which is a consequence of the rapid decrease in the number of available surface electromagnetic modes for radiation to tunnel across the vacuum gap. In contrast, eNFRHT for Au exhibits a rather broad spectral conductance that decays more slowly with the gap size (Fig. 4-4b). This slow decay is reminiscent of the situation encountered in a plate-plate geometry [164] where NFRHT is dominated by frustrated internal reflection modes, *i.e.* by modes that are evanescent in the vacuum gap but are propagating inside the Au tip and substrate whose contribution saturates for gaps below the skin depth [164], which for Au is around 25 nm. This naturally explains the weaker dependence of eNFRHT on gap size observed in our Au-Au meas-

urements. The fundamental difference in eNFRHT between dielectrics and metals is also apparent from the computed Poynting-flux patterns on the surfaces, see Fig. 4-4c-d, which show that eNFRHT in the SiO_2 case is much more concentrated in the tip apex than in the Au case. This difference reflects the fact that in a polar dielectric, like SiO_2, eNFRHT has a very strong distance dependence due to the excitation of SPhPs with a penetration depth comparable to the gap size [2]. Given these differences between metals and dielectrics, it is not surprising that Au-Au eNFRHT is relatively insensitive to small surface roughness (see Fig. S15), eliminating any doubts that the large differences between our results and that of previous work [247,248], which disagrees with the prediction of fluctuational electrodynamics, are due to variations in roughness. Our computational results, when compared to our experimental data, provide unambiguous evidence that fluctuational electrodynamics accurately describes eNFRHT.

4.4 Conclusion

We note that the results presented here provide first experimental evidence for extremely large enhancements of radiative heat transfer in the extreme near-field between both dielectric and metal surfaces. Further, our results resolve a long-standing controversy and establish the fundamental validity of fluctuational electrodynamics in modelling extreme near-field and near-field radiative heat transfer. The technical advances described in this work are key to systematically investigating eNFRHT phenomena in a variety of materials and nanostructures and provide critical information that complements insights, which can be obtained by other near-field techniques [41,251]. Knowledge gained from such studies will be critical to the development of future technologies that leverage nanoscale radiative heat transfer [56,80].

4.5 Methods

Substrate and probe preparation: Au substrates were fabricated by e-beam evaporation of Au on mica (see SI). The dielectric surfaces were created by depositing 100 nm of silica (SiO_2) or non-stoichiometric silicon nitride (SiN) on silicon (see SI). The RMS roughness of Au, SiO_2 and SiN surfaces was found to be 0.5 nm, 0.15 nm and 0.4 nm, respectively (see Fig. S5). The surface roughness of Au on the microdevice was determined to be 0.9 nm (see Fig. S5). SThM probes with embedded thermocouples were prepared as described in the SI. All probes and samples were oxygen-plasma cleaned before measurements.

Displacement of the SThM probe towards heated substrate and measurement of thermoelectric voltage output: In unmodulated experiments the SThM probe was displaced towards the heated substrate at a rate of 0.5 nm/s, and the thermoelectric voltage output from the SThM probe was measured in a bandwidth of 5 Hz. In modulated measurements the temperature of the microdevice was modulated by 5 K at 18 Hz when the gap size was larger than 6 nm. At smaller gap sizes the amplitude was reduced to 2.5 K to attenuate mechanical deflections from bimaterial effects to <0.3 nm (see SI). The gap size in the unmodulated measurements was referenced to the point at which snap-in occurs. This was found to be adequate for accurately quantifying gap size as the mechanical drift in the experiments during the time of the measurement (100 s) was negligibly small (~0.1 nm). However, in the modulated experiments it took ~1000 s to acquire each data point in Fig. 4-3d, necessitating measurements that lasted over 12 hours in total during which drift is significant. Therefore, we performed individual gap size calibrations for each data point (*i.e.* every 1000 s period) by displacing the probe towards the microdevice until contact was made. This enabled direct measurements of the gap size for each data point shown in Fig. 4-3d. In all experiments, the measured thermoelectric voltages were related to the temperature rise via the calibrated [264] Seebeck coefficient (16.3 μV/K) of the Au-Cr junction.

Modulation of the temperature of the microdevice and measurement of the amplitude of temperature modulation: The microdevice temperature was modulated sinusoidally (18 Hz) at an amplitude of 5 K by supplying a sinusoidal electric current (amplitude 0.49 mA, frequency 9 Hz) into the serpentine Pt line integrated into the microdevice. A correspondingly smaller current (0.35 mA) was applied in measurements at smaller gaps, which employed a 2.5 K temperature differential. All temperature oscillations were quantified by measuring the voltage oscillations at $3f = 27$ Hz across the Pt line as described in our previous work [262].

Computational techniques: All the simulations of the radiative heat transfer were performed with the open-source software package SCUFF-EM [270] developed by some of us. This code includes a practical implementation of the theory of fluctuational electrodynamics based on a combination of the fluctuating-surface-current formulation of the radiative heat transfer problem [108,212] with the boundary element method (BEM). In this approach, the electromagnetic fields generated by the thermal radiation are computed in terms of fictitious surface currents on the bodies. In SCUFF-EM these surface currents are determined via the BEM by discretizing the body surfaces into a mesh of triangular panels and employing a basis of vector-valued polynomi-

al functions defined on these panels (see SI). This allows us to describe bodies of arbitrary shape and achieve convergence upon decreasing the size of the triangles (see Fig. S13). SCUFF-EM makes use of the local approximation [24]. The frequency-dependent dielectric functions used in this study were obtained either from the literature (SiO_2 and Au) or from ellipsometry analysis (SiN), see Fig. S12 in the SI for details. The analysis of the effect of the tip roughness on near-field heat transfer is discussed in the SI, see Fig. S15.

Chapter 5

A Platform to Parallelize Planar Surfaces and Control Their Spatial Separation with Nanometer Resolution

Reproduced with permission from reference [4]:

Yashar Ganjeh*, Bai Song*, Krishna Pagadala, Kyeongtae Kim, Seid Sadat, Wonho Jeong, Katsuo. Kurabayashi, Edgar Meyhofer and Pramod Reddy,

Review of Scientific Instruments 83, 105101, (2012).

5.1 Abstract

Parallelizing planar surfaces and manipulating them into close proximity with spatial separation of nanoscale dimensions is critical for probing phenomena such as near-field radiative heat transport (NFRHT) and Casimir forces. Here, we report on a novel platform, with an integrated reflected light microscope, that is capable of parallelizing two planar surfaces such that the angular deviation is <6 μrad, while simultaneously allowing control of the gap from 15 μm down to contact with ~0.15 nm resolution. The capabilities of this platform were verified by using two custom-fabricated micro-devices with planar surfaces, 60 × 60 μm^2 each, whose flatness and surface roughness were experimentally quantified. We first parallelized the two micro-devices by using the developed platform in conjunction with a simple optical approach that relies on the shallow depth of field (~2 μm) of a long working distance microscope objective. Subsequently, we experimentally tested the parallelism achieved via the optical alignment procedure by taking advantage of electrodes integrated into the micro-devices. Our measurements unambiguously show that the simple depth-of-field based optical approach enables parallelization such that the angular deviation between the two surfaces is within ~500 μrad. This ensures that the separation

between any two corresponding points on the parallel surfaces deviate by ~30 nm or less from the expected value. Further, we show that improved parallelization can be achieved using the integrated micro-electrodes which enable surface roughness limited parallelization with deviations of ~5 nm from parallelism.

5.2 Introduction

The parallel-plane configuration, which refers to a geometrical setup where two planar surfaces are aligned parallel to each other, is widely used in theoretical and computational studies of near-field radiative heat transfer (NFRHT) and Casimir forces [24-26]. In fact, computational studies of NFRHT between parallel surfaces with nanoscale separation (~100 – 1000 nm) have predicted several interesting effects such as a dramatic increase—by orders of magnitude—in the radiative heat flux between planar surfaces [24-26] (in comparison to surfaces separated by macroscale gaps), and rectification of radiative heat currents [56]. Recent work has succeeded in experimentally probing NFRHT between parallel surfaces separated by micrometer sized gaps [235-237] as well as between a sphere and a plane separated by nanoscale gaps [221,222]. The sphere-plane geometry, while experimentally convenient, is not easily amenable to direct theoretical/computational analysis [201]. Further, most novel materials of interest [48,121,125] in NFRHT cannot be readily fabricated in the form of spheres—highlighting the need for an experimental platform to probe NFRHT between parallel surfaces separated by nanoscale gaps. However, such measurement capabilities are nonexistent due to the experimental challenges in parallelizing planar surfaces and controlling their separation with nanoscale resolution.

In order to overcome this experimental challenge, we have developed a novel instrument—a nanopositioner—that is capable of controlling both the relative angular alignment between planar surfaces (to parallelize them) and the spatial separation between them. This is accomplished by integrating linear stages and a high-precision piezoelectric actuator with a custom-built goniometer capable of controlling the rotation of one of the planar surfaces about two mutually perpendicular axes with ~6 μrad resolution. In this work, we first describe the rationale and design of the instrument and estimate the parallelism achievable by it. Subsequently, we report parallelization experiments performed by using micro-fabricated devices, which have a planar surface area of ~60 × 60 μm^2, in conjunction with a reflected light dark field microscope equipped with a long working distance objective. This objective features a large magnification (50X) and a rela-

tively large numerical aperture (0.55), therefore, has a shallow depth of field (~2 μm). From these experiments, we unambiguously demonstrate that it is possible to parallelize ~60 × 60 μm^2 sized planar surfaces such that the separation between corresponding points on the surfaces deviate—at most—by ~30 nm from the expected gap size. Finally, by making use of gold electrodes deposited on the micro-devices the parallelism is further improved to achieve gap sizes as low as ~5 nm, limited only by the roughness of the surfaces.

5.3 Design of the Nanopositioner

In order to parallelize two finite-area planar surfaces of equal size it is necessary to have excellent control on the relative tilt angles (θ_x, θ_y) between the two planes (see Fig. 5-1 for the definition of the coordinate system). Further, to ensure that the corresponding points of the top and bottom planes (Fig. 5-1) can be aligned precisely with respect to each other it is necessary to control both their relative alignment along the *x*, *y* directions and the angular orientation about the *z* axis (θ_z) (Fig. 5-1). Finally, in order to control the spatial separation between them it is necessary to have fine control on relative positioning of the two planes along the *z* axis. In this section, we describe the design of a custom-built nanopositioning instrument that enables control of all the relevant relative degrees-of-freedom (*x*, *y*, *z*, θ_x, θ_y, θ_z) to accomplish the desired parallelization.

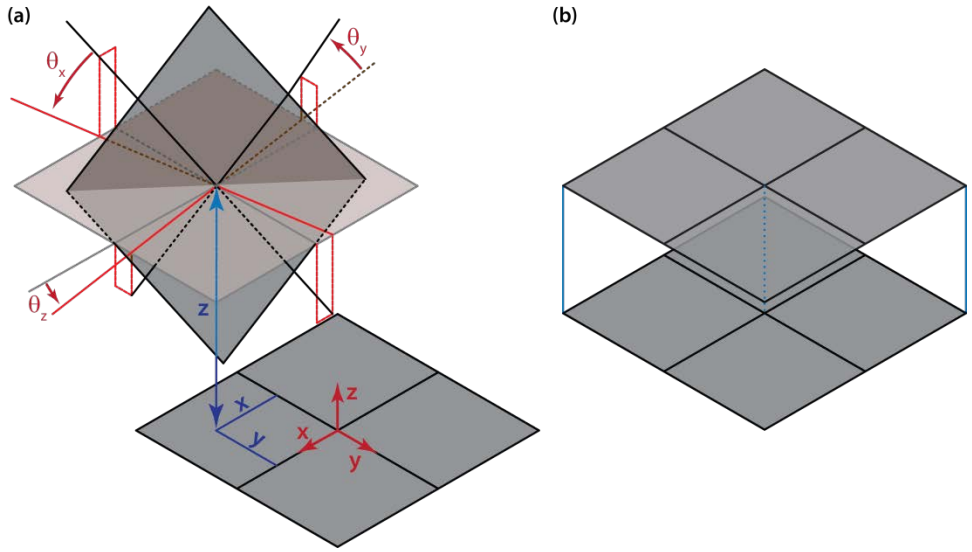

Figure 5-1. Schematic of two finite-area planar surfaces to be made parallel to each other. Control of the relative alignment along the x, y, z directions, and the relative angular alignment θ_x, θ_y, θ_z, is required to accomplish the desired parallelization. The Cartesian coordinate system is attached to the laboratory reference frame.

The basic design of the nanopositioner (Figure 2) comprises of two major subassemblies: the top and bottom subassemblies. The top subassembly (Fig. 5-2a) houses the top plane and enables fine control of θ_x, θ_y as well as coarse positioning along the x and y directions. The bottom subassembly (Fig. 5-2b) houses the bottom plane and enables coarse alignment along the x, y directions and the θ_x, θ_y angles. Further, it also enables rotation along the θ_z direction along with both coarse and fine approaches in the z direction. Figure 2c shows a cross-sectional view of the assembled nanopositioner where the top and bottom subassemblies are connected by four columns (two of the columns are not shown for visual clarity).

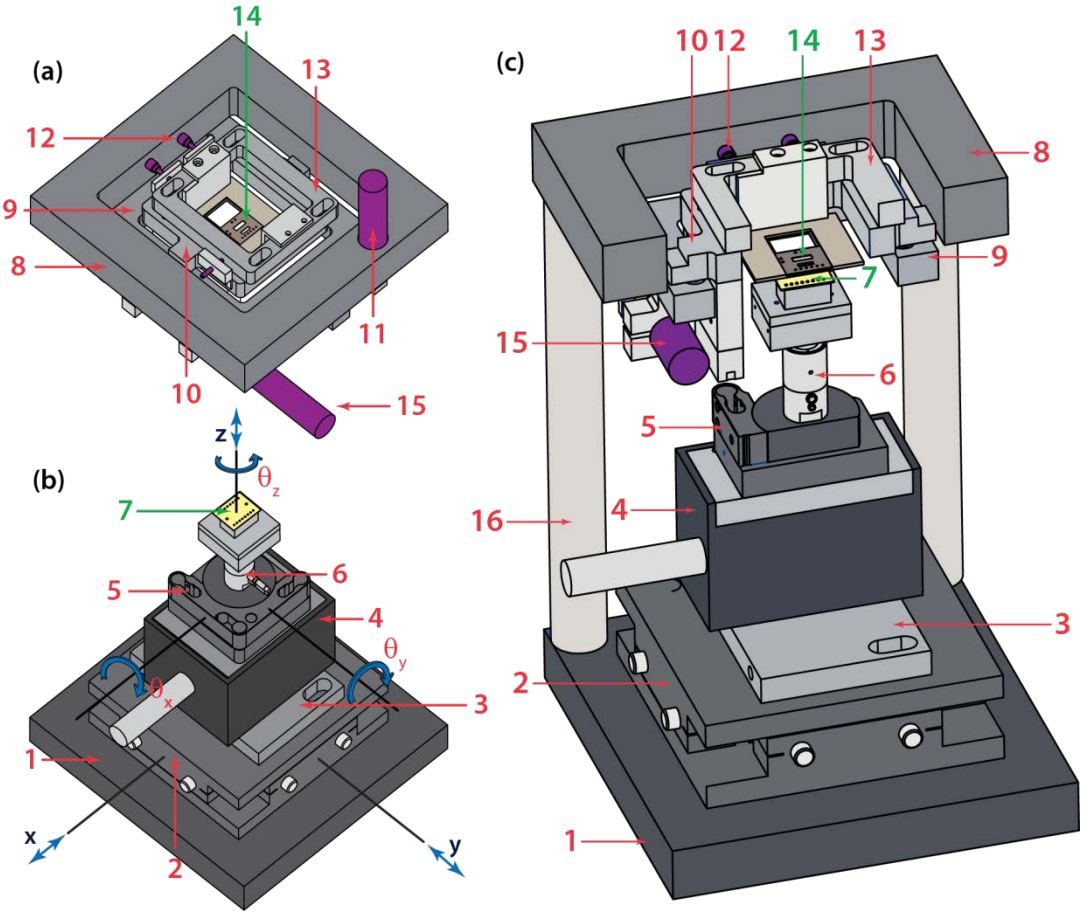

Figure 5-2. Schematic design of the nanopositioner with the major parts labeled. (a) the top subassembly is used to control the relative angular alignments θ_x, θ_y as well as to enable control of the relative alignment of the two planes along the *x, y* directions, (b) the bottom subassembly controls the relative alignment of the bottom plane along the *x, y* directions as well as the angular rotations about *x, y,* and *z* directions. The spatial separation is controlled using a *z*-linear stage and a piezoelectric actuator to control the position in *z* direction. (c) Sectional view of the top and bottom subassemblies assembled together by four columns (two of the columns are not shown for visual clarity).

Description of the Top Subassembly: In order to control the relative angular positions θ_x and θ_y, a custom-built goniometer was integrated into the top subassembly. The goniometer consists of three rigid frames: the outer frame, the middle frame and the inner frame (parts 8 - 10 of Fig. 5-2, respectively). All parts are made of Aluminum 6061, unless otherwise noted. The outer frame serves to attach the top subassembly to the bottom subassembly via four rigid columns (part 16 of Fig. 5-2c) and houses two fixed sockets of the spherical joints for θ_y -rotation (see below). The middle frame enables control of the relative rotation θ_y as it is designed to rotate about the *y* axis (see Figs. 3a and b) via two spherical joints that use precision ground stainless steel spheres. Figures 3a and b show the outer and middle frames and one such joint. The rotation of the middle frame is accomplished by using a stepper motor (part 15,Fig. 5-2a, PI M-224.27), which exerts a torque about the *y* axis. The motor has a stainless steel sphere on its head and pushes on a stainless steel attachment that is rigidly connected to the frame; these parts were made from steel to reduce surface abrasions. Further, an opposing torque is provided by a preloaded spring that pulls the middle frame against the outer frame. Thus, the motor along with the spring controls the angular position.

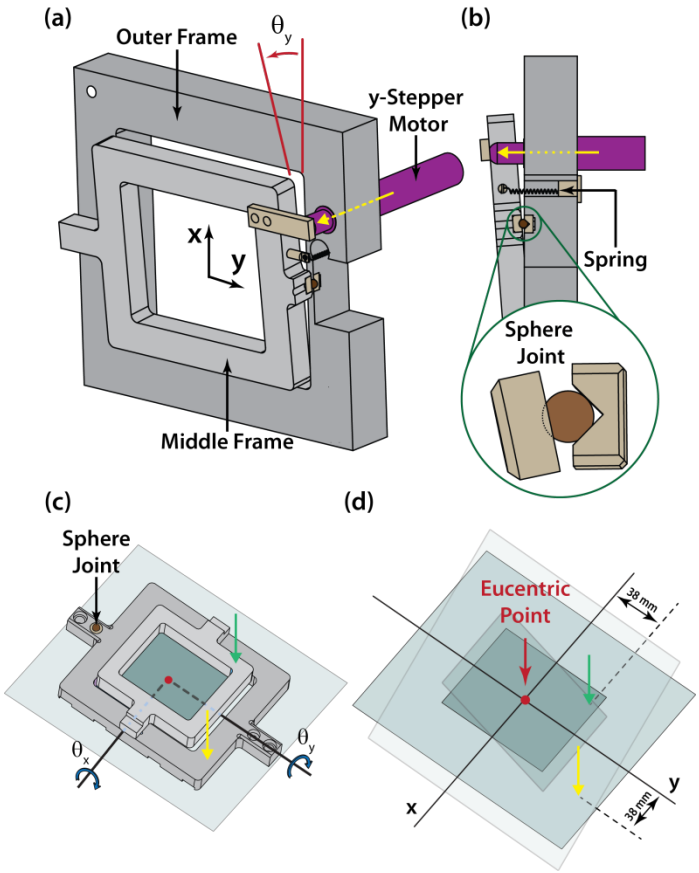

Figure 5-3. Angular control of the top plane with the custom-built goniometer. (a) isometric view showing how rotation about *y* axis is controlled; (b) side view showing the preloaded spring and one of the sphere joints; (c) schematic view of the middle and inner frames and the extended top plane (shaded blue), with arrows showing equivalently where the motors push for the *x* (green) and *y* (yellow) axes; (d) schematic drawing demonstrating how the location of eucentric point remains unchanged during rotation of the two frames and hence the importance of placing the top plane as close to it as possible. The arm lengths where each stepper applies its equivalent force are also shown.

The inner frame of the top subassembly is connected to the middle frame, via an identical design, to enable rotations about the *x* axis. Ideally, the inner and middle frames should be mounted such that the *x* and *y* axes of rotations intersect each other. However, due to inevitable tolerances in machining we estimate that the two axes are separated from each other by ~10 µm. Our analysis and experimental observations show that this small deviation from ideality does not pose significant limitations for our nanopositioning scheme; hence, we neglect it and assume that the axes intersect. The point of intersection of the axes is called the eucentric point, which represents the center of rotation (Figs. 5-3c and d).

In order to accomplish parallelization to within our experimental requirements, it is necessary to ensure that the centroid of the top plane is located in close proximity (~10 μm) to the eucentric point. If this condition is not met, rotations about the *x* and *y* axes lead to appreciable translational motion of the centroid, which is detrimental to the parallelization process. In order to position the centroid at the eucentric point, we have integrated into the inner frame an additional translational positioner (part 13 of Fig. 5-2a) that has the top plane rigidly attached to it. The *x* and *y* locations of this positioner (with respect to the inner frame) are adjusted by three micrometer screws (M3×0.25) as shown in Figure 4. After positioning the centroid of the top plane to the eucentric point the translational frame is tightly fixed to the inner frame with four M3 screws to prevent mechanical drift. The separation between the centroid and the eucentric point along the *z* axis is carefully adjusted with shim stock to reduce deviation to ~10 μm.

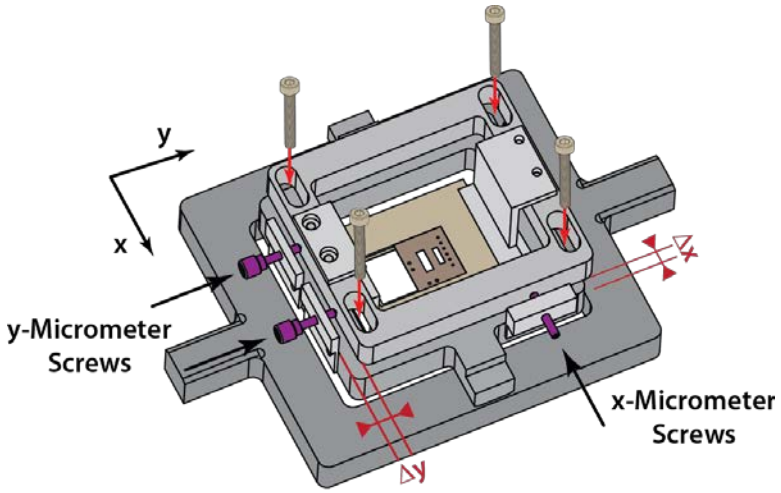

Figure 5-4. Control of the position of the top carrier in *x* and *y* directions. Three micrometer screws are used for this purpose: one for *x* direction and the other two for *y* direction adjustments. Upon reaching the final desired position of the top carrier, the location of the positioner is fixed by holding it rigidly against the inner frame using four screws as shown.

Description of the Bottom Subassembly: In order to control the relative position of the two planes along the *x*, *y*, and *z* directions as well as to control the angular rotation about the *z* axis (θ_z) we integrated a commercial *xy* linear stage (part 2 of Fig. 5-2, Newport M401), a *z* stage (part 4 of Fig. 5-2, Klinger Scientific MVD-50), a piezoelectric linear actuator along *z* direction (part 6 of Fig. 5-2, Physik Instrumente 845.10(V)), and a custom-designed *z* axis rotation element (part 3 of Fig. 5-2). Additionally, a coarse tip-tilt mechanism for controlling the angular

rotation of the bottom plane was also added (part 5 of Fig. 5-2, Newport U200-P) to further facilitate overall control of θ_x and θ_y.

The commercial *xy*-stage has an adjustment resolution of ~1 μm and a range of 12 mm in both *x* and *y* directions and supports all the components of the bottom subassembly. The *xy* linear stage is coupled to a coarse *z*-stage through the rotation element. Minor adjustment in the relative rotation of the two planes about the *z* axis is possible by rotating this element with a micrometer screw (Thorlabs DAS110, not shown in Fig. 5-2). The *z* stage has an adjustment resolution and range of 5 μm and 12 mm, respectively. This stage can be used to coarsely control the spatial separation between the top and bottom planes. For high resolution adjustments of the gap size, which is an important requirement for future NFRHT experiments, a piezoelectric actuator with a range of ~15 μm and a resolution of ~0.15 nm (limit set by our electronics) is used.

In addition to controlling translation in the *x*, *y*, and *z* directions, it is also convenient to control the angular rotation of the bottom plane using a kinematic mount (part 5 of Fig. 5-2), which is sandwiched between the *z* stage and the piezoelectric actuator. Although this alignment is in-principle not necessary for parallelization, it facilitates the particular optical approach that we implemented in this work to enable parallelization of surfaces (described in detail in Sec. 5.6). Finally, a carrier (part 7 of Fig. 5-2) that houses the bottom plane is mounted on the actuator.

Estimation of the Achievable Parallelism: We estimate the relative angular positioning that is achievable using the nanopositioner described above. The stepper motors have a step size of 200 nm. The effective arm length of the inner frame for rotation about the *x* axis is ~38 mm (Fig. 5-3d) suggesting that the angular resolution $\theta_{x,\,res}$ is ~6 μrad (200 nm/38 mm). A similar resolution is expected for rotations about the *y* axis as the arm length is the same.

To determine the degree of parallelism achievable by the platform described above, we first define as a metric for the parallelism of any two finite-area planar surfaces the spatial deviation from parallelism *p*, which is given by $p = \left|\Delta z_{\max} - \Delta z_{\min}\right|$. Here, $\Delta z_{\max}$ ($\Delta z_{\min}$) represents the maximum (minimum) separation along the *z* direction between any two points of the planes. Given the estimated angular resolution, *p* is estimated to have values ranging from 0.4 nm to 5 nm for ideal surfaces of various areas as shown in Table 5-1. In practice, a lower limit of ~5 nm is more reasonable since the inherent roughness of the real surfaces does not allow the realization of the ideal value.

Table 5-1. Estimates of the achievable spatial deviation from parallelism for ideal planar surfaces of different areas, using the custom-built nanopositioner.

Area of Parallel Surfaces	$60 \times 60\ \mu m^2$	$200 \times 200\ \mu m^2$	$1000 \times 1000\ \mu m^2$
Estimate of achievable spatial deviation from parallelism (p)	0.36 nm	1.2 nm	6 nm

5.4 Description of Micro-Devices

In order to leverage the nanopositioner and reduce the separation between two parallel planar surfaces down to the nanometer scale, both surfaces must be extremely flat, smooth, and free of particulate contamination. In other words, if either surface has an appreciable curvature, a roughness of tens of nanometers, or if there are particles of considerable size (e.g. >10 nm) on the surface, nanoscale separation with a p value smaller than the characteristic dimensions of these imperfections cannot be achieved. Creation of macroscopic surfaces that satisfy these conditions is extremely challenging due to difficulties associated with both creating such surfaces and keeping them free of particulate contamination. Further, characterization of macroscopic surfaces to ensure that they indeed meet the desired conditions is also very difficult.

In order to overcome these problems, we chose to fabricate two micro-devices each of which enclose planar regions which are ~$60 \times 60\ \mu m^2$ in size (see Fig. 5-5). The first device (see schematic in Fig. 5-5a), represents the top plane and is called the top device. It has four integrated metallic electrodes, which play an important role in our experiments (explained in detail below). The second device (Fig. 5-5b), represents the bottom plane and is a mesa-shaped structure with a planar area of ~$60 \times 60\ \mu m^2$, on its top. Further, this entire mesa-shaped structure is coated with a metal to enable the experiments (explained in detail below). These micro-devices are desirable because it is possible to directly quantify their surface characteristics using atomic force microscopy (AFM), dark field optical microscopy (DFOM), and scanning electron microscopy (SEM). We now describe our approach to practically realizing the desired devices using standard microfabrication techniques as well as our approach to characterize their surfaces.

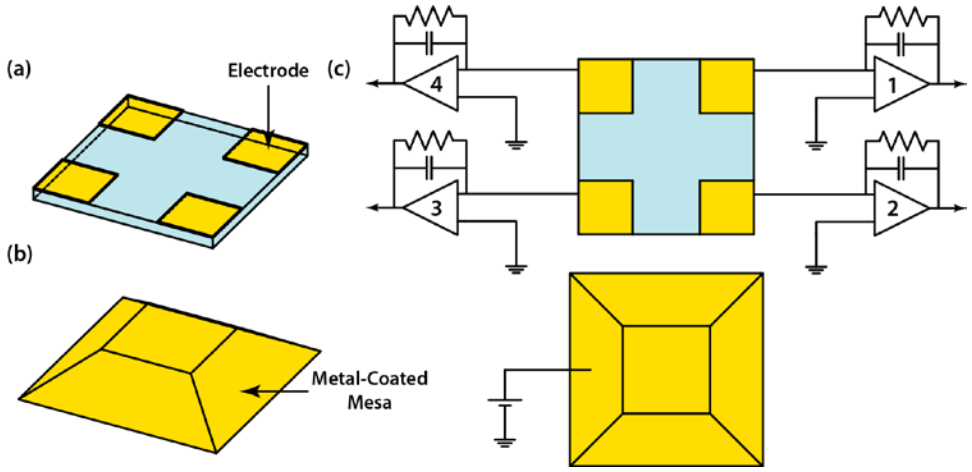

Figure 5.5 Schematic of the micro-devices. (a) top device representing the top planar surface; (b) bottom mesa device representing the bottom planar surface (shown upside-down); (c) schematic drawing showing the current amplifiers connected to the top electrodes and a voltage bias applied to the bottom electrode.

Fabrication of the Top Plane Micro-device: The fabrication of the top device is relatively simple. We fabricate the top device on a 4-inch Plan Optik Borofloat 33® glass wafer. The choice of a glass substrate is not essential but simplifies the process of optically aligning the bottom plane to the top plane due to its optical transparency (described in detail in Sec. 5.6). Fabrication of the top chip requires only a one-step lithographic patterning process using Microchem LOR lift-off resist and subsequent evaporative deposition of a 100 nm thick gold film. The lift-off photoresist is necessary to ensure that the edges of all the electrodes have no spikes or burrs. After fabrication, the wafer is diced to create chips of desired dimensions and subsequently cleaned to ensure the creation of good devices. Figures 5-6a and b show respectively the SEM and dark field optical images of one such fabricated micro-device.

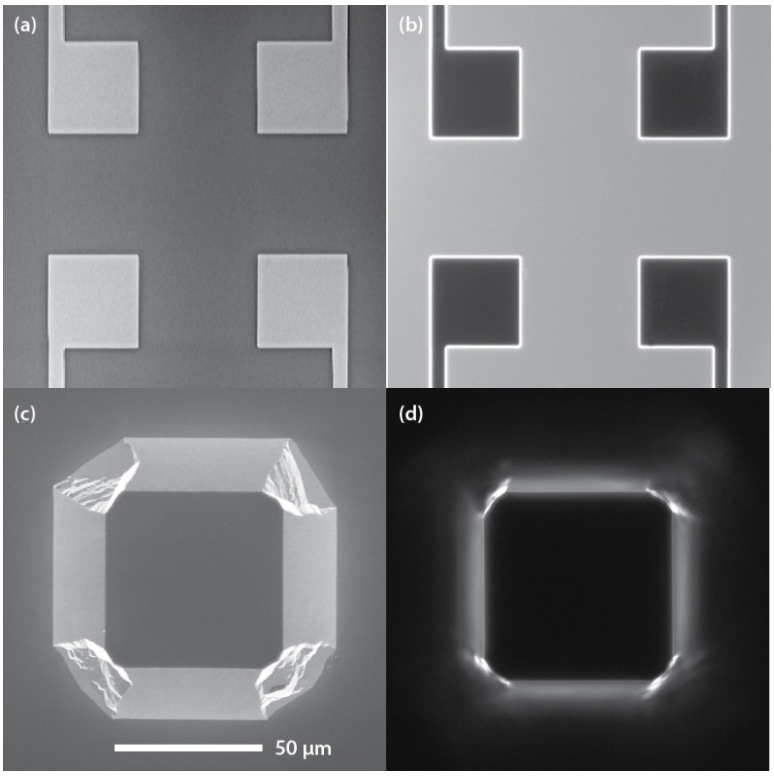

Figure 5-6. Dark field optical microscope (DFOM) and scanning electron microscope (SEM) images of the micro-devices. (a) SEM and (b) DFOM images of the top micro-device (with four gold contact pads); (c) and (d) are SEM and DFOM images of the bottom mesa device, respectively.

Fabrication of the Bottom Plane Micro-device: The mesa-shaped bottom device is made from a silicon wafer. As shown in Figure 5-7, fabrication of the mesa chip begins with the thermal growth of a ~1 µm thick silicon dioxide (SiO_2) film on top of a 4-inch (100)-oriented silicon wafer, followed by lithographic patterning of a ~60 × 60 μm^2 square SiO_2 region with ribs at the corners (Fig. 5-7) to allow for convex corner compensation [271]. Subsequently, a KOH wet, anisotropic etching step is performed to create the desired mesa structure with a square region on the top. The etching process is continuously monitored and stopped when the height of the silicon mesa is ~20 µm and an essentially square top mesa surface is formed. Without the ribs at the corners in the mask, the top surface would be more circular. After fabrication of the mesa structure, the wafer is diced into small chips under the protection of a thick layer of photoresist and cleaned with hot Baker PRS-2000 and piranha. Once the oxide mask on top of the mesa is etched away with buffered hydrofluoric acid, an ideal planar silicon surface appears. By carefully controlling the etching conditions, the etched area on the chip is essentially parallel to the mesa surface. Finally, a 5 nm thick Cr adhesion layer and a 100 nm thick Au film are sequentially depos-

ited all over the chip, which serves as an electrode in later experiments (details in Sec. 5.6). Figure 5-6c and d show an SEM and a DFOM image of the fabricated device, respectively. We note that in order to increase the yield of chips with desirable surface characteristics, it is necessary to take great care to ensure that the entire process is as clean as possible.

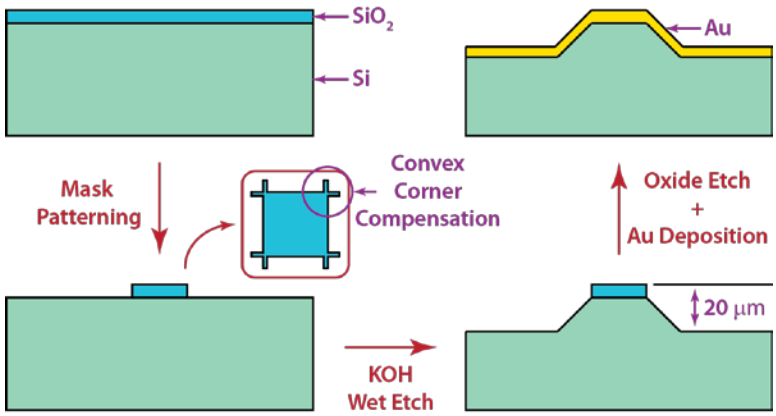

Figure 5-7. Schematic of the fabrication procedure used to create the mesa micro-device. The ribs at the corners of the square mask ensure that the final top surface of the mesa structure resembles a square.

Characterization of the Micro-Devices and Precautions during Handling: After the chips were fabricated, the surface quality was examined using an AFM (Veeco, NanoMan VS). These studies, performed on multiple devices, suggest that the curvatures of both the top and bottom surfaces are essentially zero (see Fig. 5-8a, b). Further, it was ascertained from AFM measurements that the root-mean-square roughness of both the gold-electrode patterned glass surface (top device) and the gold-coated mesa surface (bottom device) is at most ~3 nm and is <1 nm for a majority of devices (Fig. 5-8b). The AFM scans could also easily identify chips with particulate contamination. However, it was not necessary to perform AFM scans on devices to detect particulate contamination as DFOM was found to be equally effective in detecting particles as small as a few nanometers in height. This was confirmed by characterizing the same chips using both AFM (Fig. 5-8c) and DFOM (Fig. 5-8d). By carefully characterizing the top and bottom micro-devices using AFM and DFOM, we ensure that all the devices used in the current study have a negligible curvature, and a surface roughness <3 nm. Further, we ensure that no particulate contaminants of appreciable size (larger than the surface roughness) are present on the surface.

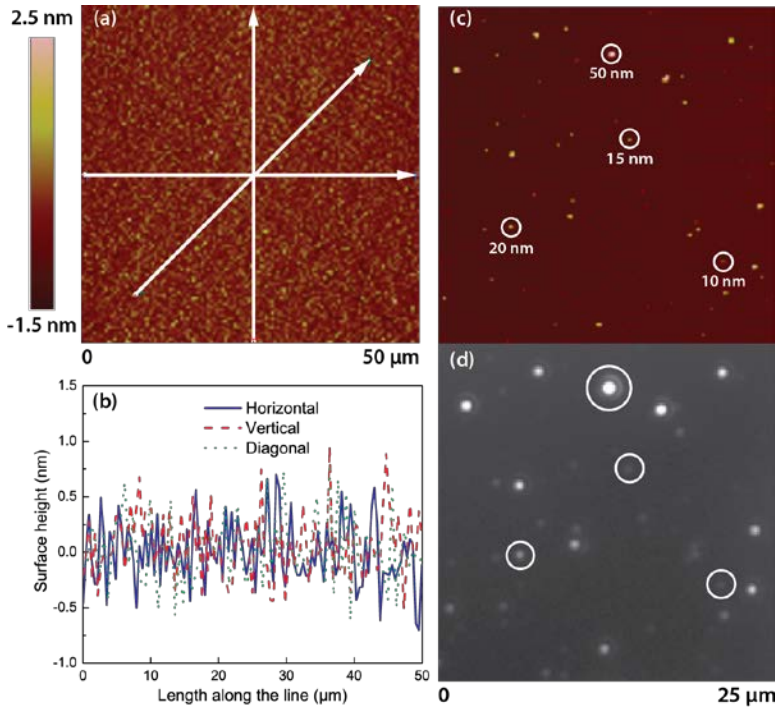

Figure 5-8. Characterization of planarity, surface roughness and particle contamination. (a) AFM images of the top of a smooth and clean mesa surface and (b) line profiles of the mesa surface. These data show that the mesa surface has no appreciable deviations from planarity and a very small surface roughness (< 1 nm rms). Similar results were obtained for the top surface (not shown). (c) An AFM image of a mesa surface with particulate contamination and the corresponding (d) A DFOM image (d). A comparison of the AFM and DFOM images shows that particles as small as 10 nm in size can be readily detected using DFOM with our microscope system (20 ms exposure with the CCD camera) and the describe device surfaces.

Once clean chips are prepared, it is of paramount importance to ensure that they remain clean for the experiments. To accomplish this, we used portable vacuum containers (Control Company 3163) for carrying the chips from cleanroom to the lab. Further, the nanopositioner was placed inside a custom-built laminar flow chamber (HEPA-filtered air) so that all the entire alignment procedure and experiments are conducted in a particle-free environment. Our tests show that once placed inside the chamber, clean chips remain free of particulate contaminations for periods as long as a week, i.e. no additional particles are introduced onto the device surface.

5.5 Optical Approach to Facilitate Parallelization

In order to effectively parallelize the surfaces it is necessary to incorporate a tool that is capable of quantitatively detecting deviations from the desired parallelism. A variety of approaches can be used to this end, including capacitive sensing [235] and interferometry [272]. Here, we

have implemented a simple optical approach (illustrated in Fig. 5-9), that uses a Zeiss microscope (Axiotech Vario) equipped with a long working distance (9 mm) and large magnification objective (Zeiss LD EC Epiplan-Neofluar 50×/0.55 HD). The long working distance objective is chosen as it provides the required spatial clearance for easy optical access to the planar surfaces of interest. At the same time, the numerical aperture (0.55) of the objective is sufficiently large to yield a shallow depth of field (~2 μm), which is essential for the optical alignment process as described below. The depth of field was confirmed experimentally by recording how the image of a point or a line changes during a through-focus imaging process (data not included).

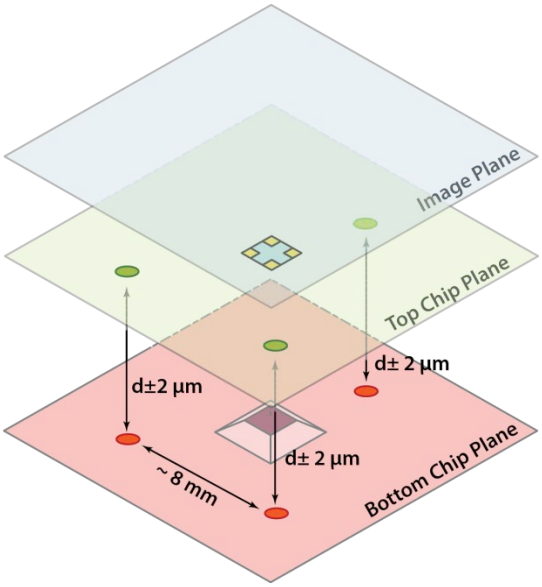

Figure 5-9. Description of the scheme used to parallelize the top and bottom surfaces. The optical alignment scheme ensures that corresponding points on the top chip plane and the bottom chip plane are at almost identical distances from each other ($d \pm 2\,\mu m$). The microfabricated devices and not drawn to scale.

Alignment Approach: In the optical alignment approach (Fig. 5-9), the microscope objective is fixed rigidly while the bottom mesa chip is oriented using the kinematic mount (part 5 of Fig. 5-2) of the bottom subassembly to place the micrometer-sized mesa surface parallel to the image plane. This is done by sequentially translating three points on the chip surface, spatially separated by ~8 mm from each other, to the center of the field of view using the *xy* linear stage; and subsequently bringing each of them into focus using the tip-tilt mechanism so that the images of all three points are contained in the same image plane. This ensures that the vertical (*z*) separation of all the three points from the image plane differs at most by the depth of field of the objec-

tive, which is ~2 μm. As a result, the corresponding angular deviation between the mesa chip surface and the image plane would be less than 250 μrad (2μm / 8mm). This completes the alignment of the bottom surface.

Subsequently, a similar approach is used to tip and tilt the top glass chip using the custom-built goniometer of the top subassembly. This enables us to place the three points on the chip surface, spatially separated from each other by ~8 mm, into a single focal plane, with a small error set by the depth of field of the microscope objective. Again, the deviation in the vertical (z) position of the three points is within ~2 μm. Together, these simple alignment procedures ensure that, without any further corrections, the maximum angular deviation would be <500 μrad. Thus, for a 60 × 60 μm^2 planar surface that meets the requirements described in section III, the spatial deviation from parallelism (p) is expected to be at most ~30 nm (500 μrad × 60 μm). We note that the use of transparent top device simplifies the alignment process, however, the capability of our platform is by no means limited to transparent surfaces. For example, for parallelizing opaque devices with thin-films deposited on a silicon wafer, one can employ a through-wafer etch. Such etching can be used to create holes at the corners of the 60 × 60 μm^2 region of interest in the top device to facilitate optical access of the bottom device. Finally, we note that the alignment approach described above does not enable us to achieve the parallelism that is, in-principle, achievable using the nanopositioner (see Table 5-1). However, if successful, the relatively simple optical approach described above enables superior parallelization without any other complicated devices such as capacitive sensors/interferometers or modification of device surfaces of interest. In the next section, we first independently quantify the parallelism achieved by the optical approach described here. Subsequently, we show that, by taking advantage of the electrodes integrated into the devices, it is possible to obtain improved parallelism with p values of ~5 nm.

5.6 Improvement and Quantification of Parallelization

In order to quantify the parallelism achieved by the optical approach we implemented a procedure that took advantage of the electrodes integrated into the top and bottom devices. In this procedure, a small voltage bias (~50 mV) was applied to the gold layer coating the bottom device (mesa structure), while each of the four electrodes of the top device was grounded and connected to four individual current amplifiers (see Fig. 5-5c). The current amplifiers serve to detect a contact between the top electrodes and the electrode on the mesa structure.

To quantify the parallelism between the surfaces, we begin by first laterally (*x*, *y* directions) aligning the top and bottom surfaces. After this alignment is accomplished, the four pads of the top devices are located directly above the four corners of the mesa structure as shown in Fig. 5-10. Subsequently, the bottom surface (mesa) is first displaced towards the top surface using the coarse *z* positioner integrated into the bottom subassembly to reduce the separation between the two surfaces to within 15 μm: the travel range of the PI piezo actuator. After this is accomplished, the piezoelectric actuator is used to gradually reduce the gap between the top and bottom surfaces by moving the bottom surface towards the top surface at a very low speed (~2 nm/s). This is continued until the bottom surface momentarily touches one of the four gold pads integrated into the top surface (see Fig. 5-10). Upon contact, an electrical current flows through the bottom electrode and the top electrode involved in the contact. As soon as a contact is detected the piezoelectric actuator is immediately withdrawn using a simple control loop implemented on a computer with an A/D converter.

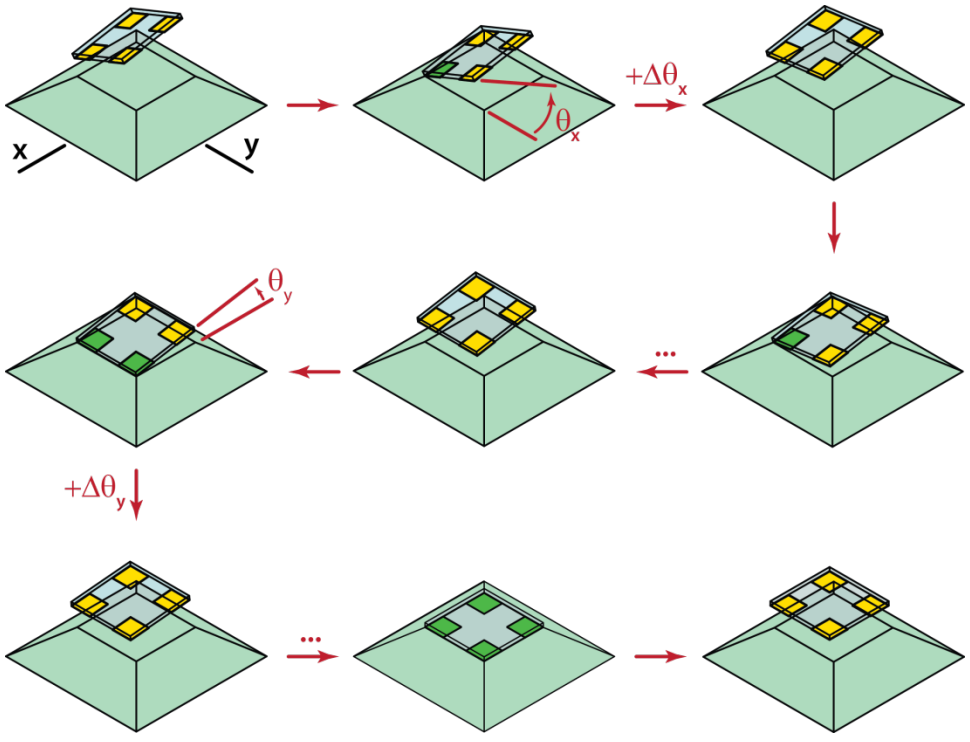

Figure 5-10. Schematic drawing of the experimental process to quantify the parallelism achieved with depth-of-field based optical alignment. In this procedure, the electrodes integrated into the top device and bottom devices are used to identify when a contact (indicated by green color) is made.

After withdrawing for a sufficiently large distance, the orientation of the top surface about the x axis is adjusted by a very small angle $\Delta\theta_x$ (typically ~25 μrad) using the motorized goniometer. The direction of rotation is chosen so that the pad which made the contact would be raised higher while the pad on the other side of x axis will be lowered. After reorienting the top surface, the bottom surface is brought up again to make a contact. If the same top electrode makes contact again the above process is repeated. This process is continued until at least one of the pads located on the other side of x axis makes contact with the mesa (instead of the top electrode that made the initial contact). The total angular rotation θ_x required to accomplish this change in contact electrodes is recorded. This represents an upper bound to the angular deviation, from parallelism, around x axis.

After the above procedure is completed, the same procedure is then used to tune the angular position about y axis. The total angle tilted about y axis, θ_y, which is the upper bound of the angular deviation around y axis, is also recorded. After the fine-tuning around both axes is completed, in almost all the experiments performed, four virtually simultaneous contacts (~2 seconds) are formed between the bottom electrode and each of the top electrodes as the bottom microdevice is driven into the top device at a slow speed (~2 nm/s). Figure 5-11 shows a typical example of contact during the piezo-driven approach of the two surfaces. As can be seen, the relative displacement of the piezo actuator from the first to the last contact is ~5 nm, which represents the maximum deviation from parallelism between the top and bottom electrodes after fine parallelization. This number is consistent with the observed surface roughness of the devices and the angular alignment accuracy of our nanopositioning system. The values of θ_x and θ_y recorded in a total of eight experiments with eight different pairs of devices with desired surface roughness are listed in Table 5-2.

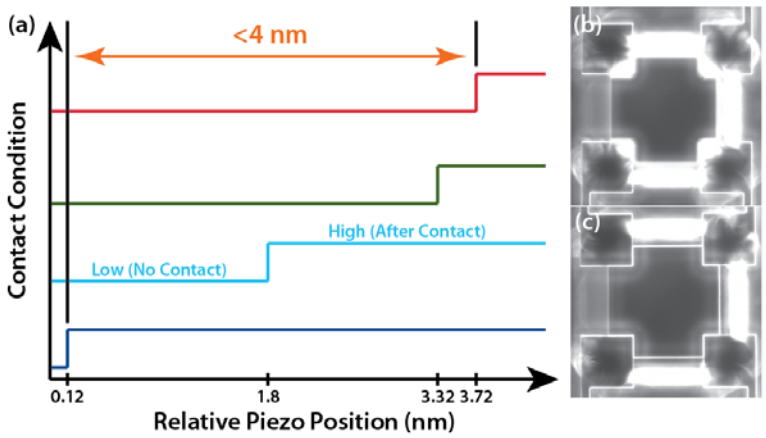

Figure 5-11. Parallelization using integrated electrodes. (a) A representative trace displaying the sequence of contact formation between the electrodes of the top and bottom device for an approach speed of 2 nm/s. Here, a low signal level indicates an open contact, whereas a high level is a sign of contact. After the first contact is made, the remaining three electrodes contact the bottom device within a displacement of <4 nm. The displacement range over which the contacts are made is independent of the approach speed (0.2 – 10 nm/s, N = 8) and is consistently smaller than 5 nm. However, the sequence in which the pads make contact may differ between experiments. (b) A dark-field optical microscope (DFOM) image of the top and bottom devices that are spatially separated by a few microns (after optical alignment). (c) A DFOM image when all four top device's electrodes make electrical contact with the electrode of the bottom device.

The measured angles θ_x and θ_y are sufficient to calculate the spatial deviation from parallelism p, achievable by the optical alignment approach as described in section 5.6. To understand this, we begin by noting that the effect of rotations about the x and y axes can be represented by rotation operators R_x and R_y that have the following form in the Cartesian coordinate system:

$$R_x = \begin{bmatrix} 1 & 0 & 0 \\ 0 & \cos\theta_x & -\sin\theta_x \\ 0 & \sin\theta_x & \cos\theta_x \end{bmatrix}, \quad R_y = \begin{bmatrix} \cos\theta_y & 0 & \sin\theta_y \\ 0 & 1 & 0 \\ -\sin\theta_y & 0 & \cos\theta_y \end{bmatrix} \tag{5-1}$$

Given an arbitrary 3D vector $\mathbf{r}_i$ representing a point on the top planar surface before fine tuning, the corresponding vector after the final tip and tilt adjustment, $\tilde{\mathbf{r}}_i$, is simply

$$\tilde{\mathbf{r}}_i = R_y R_x \mathbf{r}_i \tag{5-2}$$

Consequently, the formula for calculating $\mathbf{r}_i$ from $\tilde{\mathbf{r}}_i$ would be

$$\mathbf{r}_i = R_x^{-1} R_y^{-1} \tilde{\mathbf{r}}_i \tag{3}$$

From this expression, it is easy to see that the position vectors of the corners of the top plane ($\mathbf{r}_1, \mathbf{r}_2, \mathbf{r}_3, \mathbf{r}_4$, see Fig. 5-12) after the optical alignment, can be related to the positions of the corners ($\tilde{\mathbf{r}}_1 = (a,a,0)$, $\tilde{\mathbf{r}}_2 = (-a,a,0)$, $\tilde{\mathbf{r}}_3 = (-a,-a,0)$, $\tilde{\mathbf{r}}_4 = (a,-a,0)$) after establishing four simultaneous contacts, where *a* is half the length of the square (see Fig. 5-12). Further it can be seen that the spatial deviation from parallelism (*p*) can be obtained as:

$$p = \max\left[\left|(\mathbf{r}_1 - \mathbf{r}_3)\cdot\hat{k}\right|, \left|(\mathbf{r}_2 - \mathbf{r}_4)\cdot\hat{k}\right|\right] \tag{4}$$

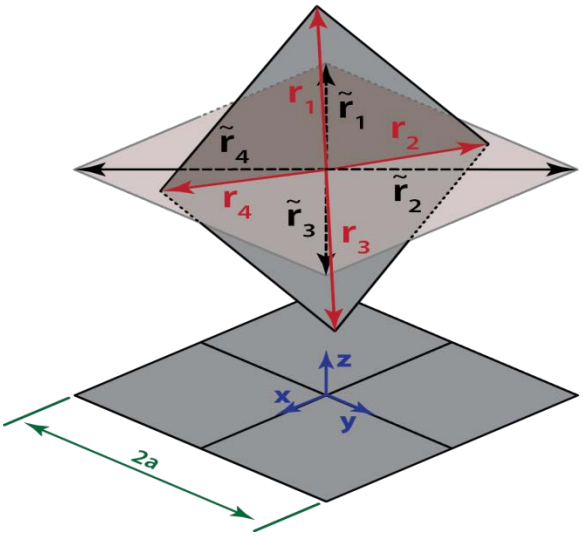

Figure 5-12. Schematic describing the analysis of parallelization.

The values of *p* corresponding to each of the experiments performed above are listed in Table 5-2 and show that the deviations achieved in seven out of the eight experiments are within the estimated value of 30 nm, while one is slightly larger (32 nm). This unequivocally shows that the nanopositioner, which we built and described in section 5.6, combined with the depth-of-field based optical approach, has the capability to parallelize two planar surfaces of the area ~60 × 60 μm^2 with a spatial deviation from parallelism *p* as low as ~30 nm. In addition, this parallelism can be further improved by using the contact-based adjustment approach described above to reach values of $p \approx 5$ nm.

Table 5-2. The angular rotations about the *x* and *y* axes to obtain four simultaneous contacts between the top electrodes and the bottom electrode. The measured spatial deviation from parallelism, in eight independent measurements, right after optical alignment is also provided.

No.	1	2	3	4	5	6	7	8
θ_x (μrad)	180	360	-120	540	60	360	150	210
θ_y (μrad)	0	0	0	0	-250	-90	240	-210
Estimated spatial deviation from parallelism, *p*, after optical alignment (nm)	11	22	7	32	20	27	23	25

5.7 Conclusion

To summarize, we have described a nanopositioner that has the ability to parallelize two finite-area planar surfaces with respect to each other with angular resolutions of ~6 μrad about the *x* and *y* axes. This excellent angular resolution is achieved by using a goniometer that is controlled via the use of high resolution stepper motors. Further, the nanopositioner is also capable of controlling the spatial separation between the planes along the *z* direction with nanometer resolution. This is accomplished by the use of a coarse *z* positioner in conjunction with a high resolution piezoelectric actuator. Further, we have unambiguously demonstrated that using solely a simple optical approach, that relies on the shallow depth of field (~2 μm) of a microscope objective, it is possible to obtain very good parallelization ($p \approx 30$ nm) of micrometer sized surfaces (~60 × 60 μm^2). We also demonstrated that this parallelization could be further improved ($p \approx 5$ nm) by a contact-based approach taking advantage of the electrodes integrated into the microdevices. We expect that important new insights into NFRHT will be obtained by combining this nanopositioning system with ultra-high resolution heat flow calorimetric techniques [273] recently developed us.

Bibliography

[1] Song, B., Fiorino, A., Meyhofer, E. & Reddy, P. Near-field radiative thermal transport: From theory to experiment. *AIP Advances* **5**, (2015).

[2] Song, B. *et al.* Enhancement of near-field radiative heat transfer using polar dielectric thin films. *Nature Nanotechnology* **10**, 253-258, (2015).

[3] Kim, K. *et al.* Radiative heat transfer in the extreme near-field. *Nature* **In Press**, (2015).

[4] Ganjeh, Y. *et al.* A platform to parallelize planar surfaces and control their spatial separation with nanometer resolution. *Review of Scientific Instruments* **83**, 105101, (2012).

[5] Barr, E. S. Historical Survey of the Early Development of the Infrared Spectral Region. *American Journal of Physics* **28**, 42-54, (1960).

[6] Herschel, W. Experiments on the refrangibility of the invisible rays of the Sun. *Philosophical Transactions of Royal Society of London* **90**, 284-292, (1800).

[7] Herschel, W. Experiments on the solar, and on the terrestrial rays that occasion heat; with a comparative view of the laws to which light and heat, or rather rays which occasion them, are subject, in order to determine whether they are the same, or different. Part I. *Philosophical Transactions of Royal Society of London* **90**, 293-326, (1800).

[8] Herschel, W. Experiments on the solar, and on the terrestrial rays that occasion heat; with a comparative view of the laws to which light and heat, or rather rays which occasion them, are subject, in order to determine whether they are the same, or different. Part II. *Philosophical Transactions of Royal Society of London* **90**, 437-538, (1800).

[9] Planck, M. Über eine Verbesserung der Wien'schen Spectralgleichung. *Verhandlungen der Deutschen Physikalischen Gesellschaft* **2**, 202-204, (1900).

[10] Planck, M. Zur Theorie des Gesetzes der Energieverteilung im Normalspectrum. *Verhandlungen der Deutschen Physikalischen Gesellschaft* **2**, 237-245, (1900).

[11] Planck, M. *The theory of heat radiation*. 2nd edn, (P. Blakiston's Son & Co., 1914).

[12] ter Haar, D. *The old quantum theory*. 1st edn, (Pergamon Press, 1967).

[13] Bohm, D. *Quantum theory*. (Dover Publications, 1989).

[14] Kragh, H. Max Planck: the reluctant revolutionary. *Phys World* **13**, 31-35, (2000).

[15] Callen, H. B. & Welton, T. A. Irreversibility and Generalized Noise. *Phys Rev* **83**, 34-40, (1951).

[16] Kubo, R. Fluctuation-Dissipation Theorem. *Rep Prog Phys* **29**, 255-284, (1966).

[17] Landau, L. D., Lifshitz, E. M. & Pitaevskii, L. P. *Statistical physics*. 3rd, rev. and enl. edn, (Pergamon Press, 1980).

[18] Eckhardt, W. Macroscopic Theory of Electromagnetic Fluctuations and Stationary Radiative Heat-Transfer. *Physical Review A* **29**, 1991-2003, (1984).

[19] Rytov, S. M. *Theory of electric fluctuations and thermal radiation*. (Air Force Cambrige Research Center, 1953).
[20] Rytov, S. M., Kravtsov, Y. A. & Tatarskii, V. I. *Principles of statistical radiophysics*. (Springer-Verlag, 1989).
[21] Emslie, A. G. in *Aerodynamically Heated Structures* (ed P. E. Glaser) (Prentice-Hall, 1962).
[22] Pendry, J. B. Radiative exchange of heat between nanostructures. *Journal of Physics-Condensed Matter* **11**, 6621-6633, (1999).
[23] Zhang, Z. M. *Nano/microscale heat transfer*. (McGraw-Hill, 2007).
[24] Joulain, K., Mulet, J. P., Marquier, F., Carminati, R. & Greffet, J. J. Surface electromagnetic waves thermally excited: Radiative heat transfer, coherence properties and Casimir forces revisited in the near field. *Surface Science Reports* **57**, 59-112, (2005).
[25] Volokitin, A. I. & Persson, B. N. J. Near-field radiative heat transfer and noncontact friction. *Reviews of Modern Physics* **79**, 1291-1329, (2007).
[26] Basu, S., Zhang, Z. M. & Fu, C. J. Review of near-field thermal radiation and its application to energy conversion. *International Journal of Energy Research* **33**, 1203-1232, (2009).
[27] Dorofeyev, I. A. & Vinogradov, E. A. Fluctuating electromagnetic fields of solids. *Phys Rep* **504**, 75-143, (2011).
[28] Jones, A. C., O'Callahan, B. T., Yang, H. U. & Raschke, M. B. The thermal near-field: Coherence, spectroscopy, heat-transfer, and optical forces. *Prog Surf Sci* **88**, 349-392, (2013).
[29] Cahill, D. G. *et al.* Nanoscale thermal transport. II. 2003-2012. *Appl Phys Rev* **1**, (2014).
[30] Xuan, Y. M. An overview of micro/nanoscaled thermal radiation and its applications. *Photonic Nanostruct* **12**, 93-113, (2014).
[31] Volokitin, A. I. & Persson, B. N. J. Radiative heat transfer and noncontact friction between nanostructures. *Physics-Uspekhi* **50**, 879-906, (2007).
[32] Girard, C., Joachim, C. & Gauthier, S. The physics of the near-field. *Rep Prog Phys* **63**, 893-938, (2000).
[33] Carminati, R. & Greffet, J. J. Near-field effects in spatial coherence of thermal sources. *Physical Review Letters* **82**, 1660-1663, (1999).
[34] Greffet, J. J. *et al.* Coherent emission of light by thermal sources. *Nature* **416**, 61-64, (2002).
[35] Marquier, F. *et al.* Coherent spontaneous emission of light by thermal sources. *Physical Review B* **69**, (2004).
[36] Laroche, M. *et al.* Highly directional radiation generated by a tungsten thermal source. *Optics Letters* **30**, 2623-2625, (2005).
[37] Laroche, M., Carminati, R. & Greffet, J. J. Coherent thermal antenna using a photonic crystal slab. *Physical Review Letters* **96**, (2006).
[38] Greffet, J. J. & Henkel, C. Coherent thermal radiation. *Contemp Phys* **48**, 183-194, (2007).
[39] Henkel, C., Joulain, K., Carminati, R. & Greffet, J. J. Spatial coherence of thermal near fields. *Optics Communications* **186**, 57-67, (2000).
[40] Shchegrov, A. V., Joulain, K., Carminati, R. & Greffet, J. J. Near-field spectral effects due to electromagnetic surface excitations. *Physical Review Letters* **85**, 1548-1551, (2000).

[41] De Wilde, Y. *et al.* Thermal radiation scanning tunnelling microscopy. *Nature* **444**, 740-743, (2006).
[42] Kittel, A. *et al.* Near-field thermal imaging of nanostructured surfaces. *Applied Physics Letters* **93**, (2008).
[43] Wischnath, U. F., Welker, J., Munzel, M. & Kittel, A. The near-field scanning thermal microscope. *Rev Sci Instrum* **79**, (2008).
[44] Kryder, M. H. *et al.* Heat Assisted Magnetic Recording. *P Ieee* **96**, 1810-1835, (2008).
[45] Challener, W. A. *et al.* Heat-assisted magnetic recording by a near-field transducer with efficient optical energy transfer. *Nature Photonics* **3**, 220-224, (2009).
[46] Stipe, B. C. *et al.* Magnetic recording at 1.5 Pb m(-2) using an integrated plasmonic antenna. *Nature Photonics* **4**, 484-488, (2010).
[47] van Zwol, P. J., Joulain, K., Ben-Abdallah, P. & Chevrier, J. Phonon polaritons enhance near-field thermal transfer across the phase transition of VO2. *Physical Review B* **84**, (2011).
[48] van Zwol, P. J., Joulain, K., Ben-Abdallah, P., Greffet, J. J. & Chevrier, J. Fast nanoscale heat-flux modulation with phase-change materials. *Physical Review B* **83**, (2011).
[49] Svetovoy, V. B., van Zwol, P. J. & Chevrier, J. Plasmon enhanced near-field radiative heat transfer for graphene covered dielectrics. *Physical Review B* **85**, (2012).
[50] Cui, L. J., Huang, Y., Wang, J. & Zhu, K. Y. Ultrafast modulation of near-field heat transfer with tunable metamaterials. *Applied Physics Letters* **102**, (2013).
[51] Vassant, S. *et al.* Electrical modulation of emissivity. *Applied Physics Letters* **102**, (2013).
[52] Huang, Y., Boriskina, S. V. & Chen, G. Electrically tunable near-field radiative heat transfer via ferroelectric materials. *Applied Physics Letters* **105**, (2014).
[53] Incardone, R., Emig, T. & Kruger, M. Heat transfer between anisotropic nanoparticles: Enhancement and switching. *Europhys Lett* **106**, (2014).
[54] Inoue, T., De Zoysa, M., Asano, T. & Noda, S. Realization of dynamic thermal emission control. *Nature Materials* **13**, 928-931, (2014).
[55] Nikbakht, M. Radiative heat transfer in anisotropic many-body systems: Tuning and enhancement. *Journal of Applied Physics* **116**, (2014).
[56] Otey, C. R., Lau, W. T. & Fan, S. H. Thermal rectification through vacuum. *Physical Review Letters* **104**, 154301, (2010).
[57] Basu, S. & Francoeur, M. Near-field radiative transfer based thermal rectification using doped silicon. *Applied Physics Letters* **98**, (2011).
[58] Iizuka, H. & Fan, S. H. Rectification of evanescent heat transfer between dielectric-coated and uncoated silicon carbide plates. *Journal of Applied Physics* **112**, (2012).
[59] Ben-Abdallah, P. & Biehs, S. A. Phase-change radiative thermal diode. *Applied Physics Letters* **103**, (2013).
[60] Huang, J. G., Li, Q., Zheng, Z. H. & Xuan, Y. M. Thermal rectification based on thermochromic materials. *International Journal of Heat and Mass Transfer* **67**, 575-580, (2013).
[61] Wang, L. P. & Zhang, Z. M. Thermal rectification enabled by near field radiative heat transfer between instrinsic silicon and a dissimilar material

Nanoscale and Microscale Thermophysical Engineering **17**, 337-348, (2013).
[62] Zhu, L. X., Otey, C. R. & Fan, S. H. Ultrahigh-contrast and large-bandwidth thermal rectification in near-field electromagnetic thermal transfer between nanoparticles. *Physical Review B* **88**, (2013).

[63] Chen, Z. *et al.* A photon thermal diode. *Nat Commun* **5**, (2014).
[64] Iizuka, H. & Fan, S. H. Consideration of enhancement of thermal rectification using metamaterial models. *Journal of Quantitative Spectroscopy & Radiative Transfer* **148**, 156-164, (2014).
[65] Nefzaoui, E., Drevillon, J., Ezzahri, Y. & Joulain, K. Simple far-field radiative thermal rectifier using Fabry-Perot cavities based infrared selective emitters. *Appl Optics* **53**, 3479-3485, (2014).
[66] Messina, R., Antezza, M. & Ben-Abdallah, P. Three-Body Amplification of Photon Heat Tunneling. *Physical Review Letters* **109**, (2012).
[67] Ben-Abdallah, P. & Biehs, S. A. Near-field thermal transistor. *Physical Review Letters* **112**, 044301, (2014).
[68] Elzouka, M. & Ndao, S. Near-field NanoThermoMechanical memory. *Applied Physics Letters* **105**, (2014).
[69] Kubytskyi, V., Biehs, S. A. & Ben-Abdallah, P. Radiative bistability and thermal memory. *Physical Review Letters* **113**, (2014).
[70] DiMatteo, R. S. *et al.* Enhanced photogeneration of carriers in a semiconductor via coupling across a nonisothermal nanoscale vacuum gap. *Applied Physics Letters* **79**, 1894-1896, (2001).
[71] Narayanaswamy, A. & Chen, G. Surface modes for near field thermophotovoltaics. *Applied Physics Letters* **82**, 3544-3546, (2003).
[72] Laroche, M., Carminati, R. & Greffet, J. J. Near-field thermophotovoltaic energy conversion. *Journal of Applied Physics* **100**, (2006).
[73] Park, K., Basu, S., King, W. P. & Zhang, Z. M. Performance analysis of near-field thermophotovoltaic devices considering absorption distribution. *Journal of Quantitative Spectroscopy & Radiative Transfer* **109**, 305-316, (2008).
[74] Dillner, U. Can Thermotunneling Improve the Currently Realized Thermoelectric Conversion Efficiency? *J Electron Mater* **39**, 1645-1649, (2010).
[75] Francoeur, M., Vaillon, R. & Mengüç, M. P. Thermal Impacts on the Performance of Nanoscale-Gap Thermophotovoltaic Power Generators. *Ieee Transactions on Energy Conversion* **26**, 686-698, (2011).
[76] Messina, R. & Ben-Abdallah, P. Graphene-based photovoltaic cells for near-field thermal energy conversion. *Sci Rep-Uk* **3**, (2013).
[77] Zhao, B., Wang, L. P., Shuai, Y. & Zhang, Z. M. Thermophotovoltaic emitters based on a two-dimensional grating/thin-film nanostructure. *International Journal of Heat and Mass Transfer* **67**, 637-645, (2013).
[78] Guo, Y., Molesky, S., Hu, H., Cortes, C. L. & Jacob, Z. Thermal excitation of plasmons for near-field thermophotovoltaics. *Applied Physics Letters* **105**, (2014).
[79] Lenert, A. *et al.* A nanophotonic solar thermophotovoltaic device. *Nat Nanotechnol* **9**, 126-130, (2014).
[80] Svetovoy, V. B. & Palasantzas, G. Graphene-on-Silicon Near-Field Thermophotovoltaic Cell. *Phys Rev Appl* **2**, (2014).
[81] Whale, M. D. & Cravalho, E. G. Modeling and performance of microscale thermophotovoltaic energy conversion devices. *Ieee Transactions on Energy Conversion* **17**, 130-142, (2002).
[82] Basu, S., Chen, Y. B. & Zhang, Z. M. Microscale radiation in thermophotovoltaic devices - A review. *International Journal of Energy Research* **31**, 689-716, (2007).

[83] Yang, R. G., Narayanaswamy, A. & Chen, G. Surface-plasmon coupled nonequilibrium thermoelectric refrigerators and power generators. *J Comput Theor Nanos* **2**, 75-87, (2005).
[84] Fang, J., Frederich, H. & Pilon, L. Harvesting Nanoscale Thermal Radiation Using Pyroelectric Materials. *Journal of Heat Transfer-Transactions of the Asme* **132**, (2010).
[85] Schwede, J. W. *et al.* Photon-enhanced thermionic emission for solar concentrator systems. *Nature Materials* **9**, 762-767, (2010).
[86] Hiller, D. *et al.* Low temperature silicon dioxide by thermal atomic layer deposition: Investigation of material properties. *Journal of Applied Physics* **107**, (2010).
[87] Svetovoy, V. B., van Zwol, P. J., Palasantzas, G. & De Hosson, J. T. M. Optical properties of gold films and the Casimir force. *Physical Review B* **77**, (2008).
[88] Siegel, R. & R.Howell, J. *Thermal radiation heat transfer*. 4th edn, (Taylor & Francis, 2002).
[89] Bijl, D. Note on thermal radiation at low temperatures. *Philosophical Magazine* **43**, 1342-1344, (1952).
[90] Dalvit, D., Milonni, P., Roberts, D. & da Rosa, F. *Casimir Physics*. (Springer-Verlag, 2011).
[91] Cravalho, E. G., Tien, C. L. & Caren, R. P. Effect of Small Spacings on Radiative Transfer between 2 Dielectrics. *Journal of Heat Transfer* **89**, 351-358, (1967).
[92] Olivei, A. Transfert d'energie thermique rayonnante entre deux delectriques aux tres basses temperatures. *Revue de Physique Appliquee* **3**, 225-230, (1968).
[93] Boehm, R. F. & Tien, C. L. Small Spacing Analysis of Radiative Parallel Metallic Surfaces. *Mech Eng* **92**, 405-411, (1970).
[94] Polder, D. & Van Hove, M. A. Theory of Radiative Heat Transfer between Closely Spaced Bodies. *Physical Review B* **4**, 3303-3314, (1971).
[95] Caren, R. P. Radiation Energy Density and Radiation Heat-Flux in Small Rectangular Cavities. *Journal of Heat Transfer* **94**, 289-294, (1972).
[96] Caren, R. P. Radiation Heat-Transfer between Closely Spaced Metal-Surfaces at Low-Temperature - Impact of Discrete Modes of Radiation Field. *Journal of Heat Transfer* **94**, 295-299, (1972).
[97] Caren, R. P. Thermal-Radiation between Closely Spaced Metal-Surfaces at Low-Temperature Due to Travelling and Quasi-Stationary Components of Radiation-Field. *International Journal of Heat and Mass Transfer* **17**, 755-765, (1974).
[98] Levin, M. L., Polevoi, V. G. & Rytov, S. M. Contribution to the theory of heat exchange due to a fluctuating electromagnetic field. *Soviet Physics, JETP* **52**, 1054-1063, (1980).
[99] Loomis, J. J. & Maris, H. J. Theory of Heat-Transfer by Evanescent Electromagnetic-Waves. *Physical Review B* **50**, 18517-18524, (1994).
[100] Hargreaves, C. M. Radiative Transfer between Closely Spaced Bodies. *Philips Research Reports*, 1-80, (1973).
[101] Cravalho, E. G., Domoto, G. A. & Tien, C. L. in *AIAA 3rd Thermophysics Conference* (Los Angeles, CA, 1968).
[102] Hargreaves, C. M. Anomalous Radiative Transfer between Closely-Spaced Bodies. *Physics Letters A* **30**, 491-492, (1969).
[103] Domoto, G. A., Boehm, R. F. & Tien, C. L. Experimental Investigation of Radiative Transfer between Metallic Surfaces at Cryogenic Temperatures. *Journal of Heat Transfer* **92**, 412-416, (1970).

[104] Kutateladze, S. S., Rubtsov, N. A. & Baltsevich, Y. A. Effect of magnitude of gap between metal plates on their thermal interaction at cryogenic temperatures. *Soviet Physics Doklady* **23**, 577-578, (1978).
[105] Baltsevich, Y. A. & Rubtsov, N. A. Experimental investigation of low-temperature radiative transfer between parallel metallic surfaces as function of the spacing between these surfaces. *Heat Transfer-Soviet Research* **12**, 117-133, (1980).
[106] Messina, R. & Antezza, M. Scattering-matrix approach to Casimir-Lifshitz force and heat transfer out of thermal equilibrium between arbitrary bodies. *Physical Review A* **84**, (2011).
[107] Kruger, M., Bimonte, G., Emig, T. & Kardar, M. Trace formulas for nonequilibrium Casimir interactions, heat radiation, and heat transfer for arbitrary objects. *Physical Review B* **86**, (2012).
[108] Rodriguez, A. W., Reid, M. T. H. & Johnson, S. G. Fluctuating-surface-current formulation of radiative heat transfer: Theory and applications. *Physical Review B* **88**, (2013).
[109] Narayanaswamy, A. & Zheng, Y. A Green's function formalism of energy and momentum transfer in fluctuational electrodynamics. *Journal of Quantitative Spectroscopy & Radiative Transfer* **132**, 12-21, (2014).
[110] Otey, C. R., Zhu, L. X., Sandhu, S. & Fan, S. H. Fluctuational electrodynamics calculations of near-field heat transfer in non-planar geometries: A brief overview. *Journal of Quantitative Spectroscopy & Radiative Transfer* **132**, 3-11, (2014).
[111] Budaev, B. V. & Bogy, D. B. On the mechanisms of heat transport across vacuum gaps. *Z Angew Math Phys* **62**, 1143-1158, (2011).
[112] Budaev, B. V. & Bogy, D. B. Extension of Planck's law to steady heat flux across nanoscale gaps. *Applied Physics a-Materials Science & Processing* **103**, 971-975, (2011).
[113] Budaev, B. V. & Bogy, D. B. Computation of radiative heat transport across a nanoscale vacuum gap. *Applied Physics Letters* **104**, (2014).
[114] Jackson, J. D. *Classical electrodynamics*. 3rd edn, (Wiley, 1999).
[115] Kong, J. A. *Electromagnetic wave theory*. (EMW Publishing, 2008).
[116] Joulain, K., Drevillon, J. & Ben-Abdallah, P. Noncontact heat transfer between two metamaterials. *Physical Review B* **81**, (2010).
[117] Zheng, Z. H. & Xuan, Y. M. Theory of near-field radiative heat transfer for stratified magnetic media. *International Journal of Heat and Mass Transfer* **54**, 1101-1110, (2011).
[118] Tai, C. T. *Dyadic green functions in electromagnetic theory*. 2nd edn, (IEEE Press, 1994).
[119] Sipe, J. E. New Green-Function Formalism for Surface Optics. *J Opt Soc Am B* **4**, 481-489, (1987).
[120] Biehs, S. A., Rousseau, E. & Greffet, J. J. Mesoscopic Description of Radiative Heat Transfer at the Nanoscale. *Physical Review Letters* **105**, (2010).
[121] Ben-Abdallah, P., Joulain, K. & Pryamikov, A. Surface Bloch waves mediated heat transfer between two photonic crystals. *Applied Physics Letters* **96**, (2010).
[122] Narayanaswamy, A. & Chen, G. Thermal emission control with one-dimensional metallodielectric photonic crystals. *Physical Review B* **70**, (2004).
[123] Narayanaswamy, A. & Chen, G. Thermal radiation in 1D photonic crystals. *Journal of Quantitative Spectroscopy & Radiative Transfer* **93**, 175-183, (2005).

[124] Pryamikov, A., Joulain, K., Ben-Abdallah, P. & Drevillon, J. Role of confined Bloch waves in the near field heat transfer between two photonic crystals. *Journal of Quantitative Spectroscopy & Radiative Transfer* **112**, 1314-1322, (2011).
[125] Biehs, S. A., Ben-Abdallah, P., da Rosa, F., Joulain, K. & Greffet, J. J. Nanoscale heat flux between nanoporous materials. *Optics Express* **19**, A1088-A1103, (2011).
[126] Nefedov, I. S. & Simovski, C. R. Giant radiation heat transfer through micron gaps. *Physical Review B* **84**, (2011).
[127] Bai, Y., Jiang, Y. Y. & Liu, L. H. Role of surface plasmon polaritons on the enhancement of the near-field thermal radiation from fishnet metamaterial. *Journal of Physics D-Applied Physics* **47**, (2014).
[128] Liu, X. L., Zhang, R. Z. & Zhang, Z. M. Near-field radiative heat transfer with doped-silicon nanostructured metamaterials. *International Journal of Heat and Mass Transfer* **73**, 389-398, (2014).
[129] Cui, L. J., Huang, Y. & Wang, J. Near-field radiative heat transfer between chiral metamaterials. *Journal of Applied Physics* **112**, (2012).
[130] Francoeur, M., Basu, S. & Petersen, S. J. Electric and magnetic surface polariton mediated near-field radiative heat transfer between metamaterials made of silicon carbide particles. *Optics Express* **19**, 18774-18788, (2011).
[131] Volokitin, A. I. & Persson, B. N. J. Radiative heat transfer between nanostructures. *Physical Review B* **63**, (2001).
[132] Francoeur, M. & Menguc, M. P. Role of fluctuational electrodynamics in near-field radiative heat transfer. *Journal of Quantitative Spectroscopy & Radiative Transfer* **109**, 280-293, (2008).
[133] Basu, S. & Wang, L. P. Near-field radiative heat transfer between doped silicon nanowire arrays. *Applied Physics Letters* **102**, (2013).
[134] Dyakov, S. A., Dai, J., Yan, M. & Qiu, M. Thermal radiation dynamics in two parallel plates: The role of near field. *Physical Review B* **90**, (2014).
[135] Volokitin, A. I. & Persson, B. N. J. Near-field radiative heat transfer between closely spaced graphene and amorphous SiO2. *Physical Review B* **83**, (2011).
[136] Ilic, O. *et al.* Near-field thermal radiation transfer controlled by plasmons in graphene. *Physical Review B* **85**, (2012).
[137] Lim, M., Lee, S. S. & Lee, B. J. Near-field thermal radiation between graphene-covered doped silicon plates. *Optics Express* **21**, 22173-22185, (2013).
[138] Drosdoff, D., Phan, A. D. & Woods, L. M. Transverse Electric Mode for Near-Field Radiative Heat Transfer in Graphene-Metamaterial Systems. *Adv Opt Mater* **2**, 1038-1042, (2014).
[139] Biehs, S. A., Rosa, F. S. S. & Ben-Abdallah, P. Modulation of near-field heat transfer between two gratings. *Applied Physics Letters* **98**, (2011).
[140] Biehs, S. A., Tschikin, M. & Ben-Abdallah, P. Hyperbolic metamaterials as an analog of a blackbody in the near field. *Physical Review Letters* **109**, (2012).
[141] Guo, Y., Cortes, C. L., Molesky, S. & Jacob, Z. Broadband super-Planckian thermal emission from hyperbolic metamaterials. *Applied Physics Letters* **101**, (2012).
[142] Biehs, S. A., Tschikin, M., Messina, R. & Ben-Abdallah, P. Super-Planckian near-field thermal emission with phonon-polaritonic hyperbolic metamaterials. *Applied Physics Letters* **102**, (2013).

[143] Guo, Y. & Jacob, Z. B. Thermal hyperbolic metamaterials. *Optics Express* **21**, 15014-15019, (2013).
[144] Liu, X. L., Zhang, R. Z. & Zhang, Z. M. Near-field thermal radiation between hyperbolic metamaterials: Graphite and carbon nanotubes. *Applied Physics Letters* **103**, (2013).
[145] Guo, Y. & Jacob, Z. Fluctuational electrodynamics of hyperbolic metamaterials. *Journal of Applied Physics* **115**, (2014).
[146] Miller, O. D., Johnson, S. G. & Rodriguez, A. W. Effectiveness of Thin Films in Lieu of Hyperbolic Metamaterials in the Near Field. *Physical Review Letters* **112**, (2014).
[147] Nefedov, I. S. & Melnikov, L. A. Super-Planckian far-zone thermal emission from asymmetric hyperbolic metamaterials. *Applied Physics Letters* **105**, (2014).
[148] Basu, S. & Zhang, Z. M. Maximum energy transfer in near-field thermal radiation at nanometer distances. *Journal of Applied Physics* **105**, (2009).
[149] Wang, X. J., Basu, S. & Zhang, Z. M. Parametric optimization of dielectric functions for maximizing nanoscale radiative transfer. *Journal of Physics D-Applied Physics* **42**, (2009).
[150] Ben-Abdallah, P. & Joulain, K. Fundamental limits for noncontact transfers between two bodies. *Physical Review B* **82**, (2010).
[151] Basu, S. & Francoeur, M. Maximum near-field radiative heat transfer between thin films. *Applied Physics Letters* **98**, (2011).
[152] Zhao, Y., Tang, G. H. & Li, Z. Y. Parametric investigation for suppressing near-field thermal radiation between two spherical nanoparticles. *Int Commun Heat Mass* **39**, 918-922, (2012).
[153] Nefzaoui, E., Ezzahri, Y., Drevillon, J. & Joulain, K. Maximal near-field radiative heat transfer between two plates. *Eur. Phys. J. Appl. Phys.* **63**, 30902, (2013).
[154] Simovski, C., Maslovski, S., Nefedov, I. & Tretyakov, S. Optimization of radiative heat transfer in hyperbolic metamaterials for thermophotovoltaic applications. *Optics Express* **21**, 14988-15013, (2013).
[155] Francoeur, M., Menguc, M. P. & Vaillon, R. Solution of near-field thermal radiation in one-dimensional layered media using dyadic Green's functions and the scattering matrix method. *Journal of Quantitative Spectroscopy & Radiative Transfer* **110**, 2002-2018, (2009).
[156] Francoeur, M., Mengüç, M. P. & Vaillon, R. Coexistence of multiple regimes for near-field thermal radiation between two layers supporting surface phonon polaritons in the infrared. *Physical Review B* **84**, (2011).
[157] Zheng, Z. H. & Xuan, Y. M. Near-field radiative heat transfer between general materials and metamaterials. *Chinese Sci Bull* **56**, 2312-2319, (2011).
[158] Mulet, J. P., Joulain, K., Carminati, R. & Greffet, J. J. Enhanced radiative heat transfer at nanometric distances. *Microscale Thermophysical Engineering* **6**, 209-222, (2002).
[159] Biehs, S. A. & Greffet, J. J. Influence of roughness on near-field heat transfer between two plates. *Physical Review B* **82**, (2010).
[160] Fu, C. J. & Zhang, Z. M. Nanoscale radiation heat transfer for silicon at different doping levels. *International Journal of Heat and Mass Transfer* **49**, 1703-1718, (2006).
[161] Rousseau, E., Laroche, M. & Greffet, J. J. Radiative heat transfer at nanoscale mediated by surface plasmons for highly doped silicon. *Applied Physics Letters* **95**, (2009).

[162] Rousseau, E., Laroche, M. & Greffet, J. J. Radiative heat transfer at nanoscale: Closed-form expression for silicon at different doping levels. *Journal of Quantitative Spectroscopy & Radiative Transfer* **111**, 1005-1014, (2010).
[163] Liu, B. A., Shi, J. W., Liew, K. & Shen, S. Near-field radiative heat transfer for Si based metamaterials. *Optics Communications* **314**, 57-65, (2014).
[164] Chapuis, P. O., Volz, S., Henkel, C., Joulain, K. & Greffet, J. J. Effects of spatial dispersion in near-field radiative heat transfer between two parallel metallic surfaces. *Physical Review B* **77**, 9, (2008).
[165] Zheng, Y. & Narayanaswamy, A. Patch contribution to near-field radiative energy transfer and van der Waals pressure between two half-spaces. *Physical Review A* **89**, (2014).
[166] Biehs, S. A. Thermal heat radiation, near-field energy density and near-field radiative heat transfer of coated materials. *Eur Phys J B* **58**, 423-431, (2007).
[167] Biehs, S. A., Reddig, D. & Holthaus, M. Thermal radiation and near-field energy density of thin metallic films. *Eur Phys J B* **55**, 237-251, (2007).
[168] Francoeur, M., Menguc, M. P. & Vaillon, R. Near-field radiative heat transfer enhancement via surface phonon polaritons coupling in thin films. *Applied Physics Letters* **93**, 089901, (2008).
[169] Ben-Abdallah, P., Joulain, K., Drevillon, J. & Domingues, G. Near-field heat transfer mediated by surface wave hybridization between two films. *Journal of Applied Physics* **106**, (2009).
[170] Fu, C. J. & Tan, W. C. Near-field radiative heat transfer between two plane surfaces with one having a dielectric coating. *Journal of Quantitative Spectroscopy & Radiative Transfer* **110**, 1027-1036, (2009).
[171] Francoeur, M., Menguc, M. P. & Vaillon, R. Spectral tuning of near-field radiative heat flux between two thin silicon carbide films. *Journal of Physics D-Applied Physics* **43**, (2010).
[172] Francoeur, M., Menguc, M. P. & Vaillon, R. Control of near-field radiative heat transfer via surface phonon-polariton coupling in thin films. *Applied Physics A-Materials Science & Processing* **103**, 547-550, (2011).
[173] Wang, L. P., Basu, S. & Zhang, Z. M. Direct and Indirect Methods for Calculating Thermal Emission From Layered Structures With Nonuniform Temperatures. *Journal of Heat Transfer-Transactions of the Asme* **133**, (2011).
[174] Carrillo, L. Y. & Bayazitoglu, Y. Nanorod near-field radiative heat exchange analysis. *Journal of Quantitative Spectroscopy & Radiative Transfer* **112**, 412-419, (2011).
[175] Carrillo, L. Y. & Bayazitoglu, Y. Sphere Approximation for Nanorod near-Field Radiative Heat Exchange Analysis. *Nanoscale and Microscale Thermophysical Engineering* **15**, 195-208, (2011).
[176] Mulet, J. P., Joulain, K., Carminati, R. & Greffet, J. J. Nanoscale radiative heat transfer between a small particle and a plane surface. *Applied Physics Letters* **78**, 2931-2933, (2001).
[177] Chapuis, P. O., Greffet, J. J., Joulain, K. & Volz, S. Heat transfer between a nano-tip and a surface. *Nanotechnology* **17**, 2978-2981, (2006).
[178] Biehs, S. A., Huth, O. & Ruting, F. Near-field radiative heat transfer for structured surfaces. *Physical Review B* **78**, (2008).

[179] Chapuis, P. O., Laroche, M., Volz, S. & Greffet, J. J. Near-field induction heating of metallic nanoparticles due to infrared magnetic dipole contribution. *Physical Review B* **77**, (2008).
[180] Biehs, S. A. & Greffet, J. J. Near-field heat transfer between a nanoparticle and a rough surface. *Physical Review B* **81**, (2010).
[181] Narayanaswamy, A. & Chen, G. Thermal near-field radiative transfer between two spheres. *Physical Review B* **77**, (2008).
[182] Carrillo, L. Y. & Bayazitoglu, Y. Nanosphere Near-Field Radiative Heat-Exchange Analysis. *J Thermophys Heat Tr* **24**, 309-315, (2010).
[183] Sasihithlu, K. & Narayanaswamy, A. Convergence of vector spherical wave expansion method applied to near-field radiative transfer. *Optics Express* **19**, A772-A785, (2011).
[184] Sasihithlu, K. & Narayanaswamy, A. Proximity effects in radiative heat transfer. *Physical Review B* **83**, (2011).
[185] Zhang, Z. M. & Lee, B. J. Lateral shift in photon tunneling studied by the energy streamline method. *Optics Express* **14**, 9963-9970, (2006).
[186] Lee, B. J., Park, K. & Zhang, Z. M. Energy pathways in nanoscale thermal radiation. *Applied Physics Letters* **91**, (2007).
[187] Basu, S., Wang, L. P. & Zhang, Z. M. Direct calculation of energy streamlines in near-field thermal radiation. *Journal of Quantitative Spectroscopy & Radiative Transfer* **112**, 1149-1155, (2011).
[188] Basu, S. & Zhang, Z. M. Ultrasmall penetration depth in nanoscale thermal radiation. *Applied Physics Letters* **95**, 133104, (2009).
[189] Basu, S. & Francoeur, M. Penetration depth in near-field radiative heat transfer between metamaterials. *Applied Physics Letters* **99**, (2011).
[190] Lang, S., Tschikin, M., Biehs, S. A., Petrov, A. Y. & Eich, M. Large penetration depth of near-field heat flux in hyperbolic media. *Applied Physics Letters* **104**, (2014).
[191] Joulain, K., Carminati, R., Mulet, J. P. & Greffet, J. J. Definition and measurement of the local density of electromagnetic states close to an interface. *Physical Review B* **68**, (2003).
[192] Ben-Abdallah, P., Joulain, K., Drevillon, J. & Domingues, G. Tailoring the local density of states of nonradiative field at the surface of nanolayered materials. *Applied Physics Letters* **94**, (2009).
[193] Francoeur, M., Menguc, M. P. & Vaillon, R. Local density of electromagnetic states within a nanometric gap formed between two thin films supporting surface phonon polaritons. *Journal of Applied Physics* **107**, (2010).
[194] Narayanaswamy, A. & Chen, G. Dyadic Green's functions and electromagnetic local density of states. *Journal of Quantitative Spectroscopy & Radiative Transfer* **111**, 1877-1884, (2010).
[195] Ruting, F., Biehs, S. A., Huth, O. & Holthaus, M. Second-order calculation of the local density of states above a nanostructured surface. *Physical Review B* **82**, (2010).
[196] Zhang, Z. M. & Basu, S. Entropy flow and generation in radiative transfer between surfaces. *International Journal of Heat and Mass Transfer* **50**, 702-712, (2007).
[197] Dorofeyev, I. Thermodynamic functions of fluctuating electromagnetic fields within a heterogeneous system. *Phys Scripta* **84**, (2011).
[198] Narayanaswamy, A. & Zheng, Y. Theory of thermal nonequilibrium entropy in near-field thermal radiation. *Physical Review B* **88**, (2013).

[199] Latella, I., Perez-Madrid, A., Lapas, L. C. & Rubi, J. M. Near-field thermodynamics: Useful work, efficiency, and energy harvesting. *Journal of Applied Physics* **115**, (2014).
[200] Derjaguin, B. V., Abrikosova, I. I. & Lifshitz, E. M. Direct Measurement of Molecular Attraction between Solids Separated by a Narrow Gap. *Quarterly Reviews* **10**, 295-329, (1956).
[201] Otey, C. & Fan, S. H. Numerically exact calculation of electromagnetic heat transfer between a dielectric sphere and plate. *Physical Review B* **84**, (2011).
[202] Zhao, B. & Zhang, Z. M. Study of magnetic polaritons in deep gratings for thermal emission control. *Journal of Quantitative Spectroscopy & Radiative Transfer* **135**, 81-89, (2014).
[203] Johnson, S. G. in *Casimir Physics* (eds Diego Dalvit, Peter Milonni, David Roberts, & Felipe da Rosa) (Springer-Verlag, 2011).
[204] Whittaker, D. M. & Culshaw, I. S. Scattering-matrix treatment of patterned multilayer photonic structures. *Physical Review B* **60**, 2610-2618, (1999).
[205] Bimonte, G. Scattering approach to Casimir forces and radiative heat transfer for nanostructured surfaces out of thermal equilibrium. *Physical Review A* **80**, (2009).
[206] Rahi, S. J., Emig, T., Graham, N., Jaffe, R. L. & Kardar, M. Scattering theory approach to electrodynamic Casimir forces. *Phys Rev D* **80**, (2009).
[207] Kruger, M., Emig, T. & Kardar, M. Nonequilibrium Electromagnetic Fluctuations: Heat Transfer and Interactions. *Physical Review Letters* **106**, (2011).
[208] Messina, R. & Antezza, M. Casimir-Lifshitz force out of thermal equilibrium and heat transfer between arbitrary bodies. *Epl-Europhys Lett* **95**, (2011).
[209] McCauley, A. P., Reid, M. T. H., Kruger, M. & Johnson, S. G. Modeling near-field radiative heat transfer from sharp objects using a general three-dimensional numerical scattering technique. *Physical Review B* **85**, (2012).
[210] Guerout, R. *et al.* Enhanced radiative heat transfer between nanostructured gold plates. *Physical Review B* **85**, (2012).
[211] Lussange, J. *et al.* Radiative heat transfer between two dielectric nanogratings in the scattering approach. *Physical Review B* **86**, (2012).
[212] Rodriguez, A. W., Reid, M. T. H. & Johnson, S. G. Fluctuating-surface-current formulation of radiative heat transfer for arbitrary geometries. *Physical Review B* **86**, (2012).
[213] Rodriguez, A. W. *et al.* Anomalous Near-Field Heat Transfer between a Cylinder and a Perforated Surface. *Physical Review Letters* **110**, 014301, (2013).
[214] Luo, C., Narayanaswamy, A., Chen, G. & Joannopoulos, J. D. Thermal radiation from photonic crystals: A direct calculation. *Physical Review Letters* **93**, (2004).
[215] Rodriguez, A. W. *et al.* Frequency-Selective Near-Field Radiative Heat Transfer between Photonic Crystal Slabs: A Computational Approach for Arbitrary Geometries and Materials. *Physical Review Letters* **107**, 114302, (2011).
[216] Datas, A., Hirashima, D. & Hanamura, K. FDTD Simulation of Near-Field Radiative Heat Transfer between Thin Films Supporting Surface Phonon Polaritons: Lessons Learned. *J Therm Sci Tech-Jpn* **8**, 91-105, (2013).
[217] Didari, A. & Menguc, M. P. Analysis of near-field radiation transfer within nano-gaps using FDTD method. *Journal of Quantitative Spectroscopy & Radiative Transfer* **146**, 214-226, (2014).

[218] Wen, S. B. Direct Numerical Simulation of Near Field Thermal Radiation Based on Wiener Chaos Expansion of Thermal Fluctuating Current. *Journal of Heat Transfer-Transactions of the Asme* **132**, (2010).
[219] Liu, B. A. & Shen, S. Broadband near-field radiative thermal emitter/absorber based on hyperbolic metamaterials: Direct numerical simulation by the Wiener chaos expansion method. *Physical Review B* **87**, (2013).
[220] Edalatpour, S. & Francoeur, M. The Thermal Discrete Dipole Approximation (T-DDA) for near-field radiative heat transfer simulations in three-dimensional arbitrary geometries. *Journal of Quantitative Spectroscopy & Radiative Transfer* **133**, 364-373, (2014).
[221] Rousseau, E. *et al.* Radiative heat transfer at the nanoscale. *Nature Photonics* **3**, 514-517, (2009).
[222] Shen, S., Narayanaswamy, A. & Chen, G. Surface phonon polaritons mediated energy transfer between nanoscale gaps. *Nano Letters* **9**, 2909-2913, (2009).
[223] Harrington, R. F. Boundary Integral Formulations for Homogeneous Material Bodies. *Journal of Electromagnetic Waves and Applications* **3**, 1-15, (1989).
[224] Rengarajan, S. R. & Rahmat-Samii, Y. The field equivalence principle: Illustration of the establishment of the non-intuitive null fields. *Ieee Antenn Propag M* **42**, 122-128, (2000).
[225] Rao, S. M., Wilton, D. R. & Glisson, A. W. Electromagnetic Scattering by Surfaces of Arbitrary Shape. *Ieee T Antenn Propag* **30**, 409-418, (1982).
[226] Homer Reid, M. T. *http://homerreid.dyndns.org/scuff-EM/*.
[227] Taflove, A. & Hagness, S. C. *Computational electrodynamics : the finite-difference time-domain method*. 3rd edn, (Artech House, 2005).
[228] Hou, T. Y., Luo, W., Rozovskii, B. & Zhou, H. M. Wiener Chaos expansions and numerical solutions of randomly forced equations of fluid mechanics. *J Comput Phys* **216**, 687-706, (2006).
[229] Draine, B. T. & Flatau, P. J. Discrete-Dipole Approximation for Scattering Calculations. *J Opt Soc Am A* **11**, 1491-1499, (1994).
[230] Roberts, N. A. & Walker, D. G. A review of thermal rectification observations and models in solid materials. *Int J Therm Sci* **50**, 648-662, (2011).
[231] Li, N. B. *et al.* Colloquium: Phononics: Manipulating heat flow with electronic analogs and beyond. *Reviews of Modern Physics* **84**, 1045-1066, (2012).
[232] Chang, C. W., Okawa, D., Majumdar, A. & Zettl, A. Solid-state thermal rectifier. *Science* **314**, 1121-1124, (2006).
[233] Qazilbash, M. M. *et al.* Mott transition in VO2 revealed by infrared spectroscopy and nano-imaging. *Science* **318**, 1750-1753, (2007).
[234] Zhu, L. X., Otey, C. R. & Fan, S. H. Negative differential thermal conductance through vacuum. *Applied Physics Letters* **100**, (2012).
[235] Ottens, R. S. *et al.* Near-Field Radiative Heat Transfer between Macroscopic Planar Surfaces. *Physical Review Letters* **107**, (2011).
[236] Hu, L., Narayanaswamy, A., Chen, X. Y. & Chen, G. Near-field thermal radiation between two closely spaced glass plates exceeding Planck's blackbody radiation law. *Applied Physics Letters* **92**, (2008).
[237] Kralik, T., Hanzelka, P., Musilova, V., Srnka, A. & Zobac, M. Cryogenic apparatus for study of near-field heat transfer. *Rev Sci Instrum* **82**, (2011).
[238] Kralik, T. *et al.* Strong Near-Field Enhancement of Radiative Heat Transfer between Metallic Surfaces. *Physical Review Letters* **109**, (2012).

[239] Feng, C., Tang, Z. A. & Yu, J. A Novel CMOS Device Capable of Measuring Near-Field Thermal Radiation. *Chinese Phys Lett* **29**, (2012).
[240] Feng, C., Tang, Z. A., Yu, J. & Sun, C. Y. A MEMS Device Capable of Measuring Near-Field Thermal Radiation between Membranes. *Sensors-Basel* **13**, 1998-2010, (2013).
[241] St-Gelais, R., Guha, B., Zhu, L. X., Fan, S. H. & Lipson, M. Demonstration of Strong Near-Field Radiative Heat Transfer between Integrated Nanostructures. *Nano Letters* **14**, 6971-6975, (2014).
[242] Williams, C. C. & Wickramasinghe, H. K. Scanning Thermal Profiler. *Applied Physics Letters* **49**, 1587-1589, (1986).
[243] Dransfeld, K. & Xu, J. B. The Heat-Transfer between a Heated Tip and a Substrate - Fast Thermal Microscopy. *J Microsc-Oxford* **152**, 35-42, (1988).
[244] Xu, J. B., Lauger, K., Dransfeld, K. & Wilson, I. H. Thermal Sensors for Investigation of Heat-Transfer in Scanning Probe Microscopy. *Rev Sci Instrum* **65**, 2262-2266, (1994).
[245] Xu, J. B., Lauger, K., Moller, R., Dransfeld, K. & Wilson, I. H. Heat transfer between two Metallic Surfaces at Small Distances. *Journal of Applied Physics* **76**, 7209-7216, (1994).
[246] Muller-Hirsch, W., Kraft, A., Hirsch, M. T., Parisi, J. & Kittel, A. Heat transfer in ultrahigh vacuum scanning thermal microscopy. *Journal of Vacuum Science & Technology a-Vacuum Surfaces and Films* **17**, 1205-1210, (1999).
[247] Kittel, A. *et al.* Near-field heat transfer in a scanning thermal microscope. *Physical Review Letters* **95**, 224301, (2005).
[248] Worbes, L., Hellmann, D. & Kittel, A. Enhanced Near-Field Heat Flow of a Monolayer Dielectric Island. *Physical Review Letters* **110**, (2013).
[249] Guha, B., Otey, C., Poitras, C. B., Fan, S. H. & Lipson, M. Near-Field Radiative Cooling of Nanostructures. *Nano Letters* **12**, 4546-4550, (2012).
[250] Babuty, A., Joulain, K., Chapuis, P. O., Greffet, J. J. & De Wilde, Y. Blackbody Spectrum Revisited in the Near Field. *Physical Review Letters* **110**, (2013).
[251] Jones, A. C. & Raschke, M. B. Thermal Infrared Near-Field Spectroscopy. *Nano Letters* **12**, 1475-1481, (2012).
[252] O'Callahan, B. T., Lewis, W. E., Jones, A. C. & Raschke, M. B. Spectral frustration and spatial coherence in thermal near-field spectroscopy. *Physical Review B* **89**, (2014).
[253] Joulain, K. *et al.* Strong tip-sample coupling in thermal radiation scanning tunneling microscopy. *Journal of Quantitative Spectroscopy & Radiative Transfer* **136**, 1-15, (2014).
[254] Peragut, F., Brubach, J. B., Roy, P. & De Wilde, Y. Infrared near-field imaging and spectroscopy based on thermal or synchrotron radiation. *Applied Physics Letters* **104**, (2014).
[255] Zhang, L. M. *et al.* Near-field spectroscopy of silicon dioxide thin films. *Physical Review B* **85**, (2012).
[256] Narayanaswamy, A., Shen, S. & Chen, G. Near-field radiative heat transfer between a sphere and a substrate. *Physical Review B* **78**, 115303, (2008).
[257] Shen, S., Mavrokefalos, A., Sambegoro, P. & Chen, G. Nanoscale thermal radiation between two gold surfaces. *Applied Physics Letters* **100**, (2012).
[258] van Zwol, P. J., Ranno, L. & Chevrier, J. Tuning Near Field Radiative Heat Flux through Surface Excitations with a Metal Insulator Transition. *Physical Review Letters* **108**, 234301, (2012).

[259] van Zwol, P. J., Thiele, S., Berger, C., de Heer, W. A. & Chevrier, J. Nanoscale Radiative Heat Flow due to Surface Plasmons in Graphene and Doped Silicon. *Physical Review Letters* **109**, (2012).
[260] Shi, J. W., Li, P. F., Liu, B. A. & Shen, S. Tuning near field radiation by doped silicon. *Applied Physics Letters* **102**, (2013).
[261] Francoeur, M. Near-field radiative energy transfer: Nanostructures feel the heat. *Nat Nanotechnol* **10**, 206-208, (2015).
[262] Sadat, S., Meyhofer, E. & Reddy, P. Resistance thermometry-based picowatt-resolution heat-flow calorimeter. *Applied Physics Letters* **102**, 163110, (2013).
[263] Rytov, S. M., Kravtsov, I. A. & Tatarskii, V. I. *Principles of statistical radiophysics*. 2. rev. and enl. edn, (Springer-Verlag, 1987).
[264] Kim, K., Jeong, W., Lee, W. & Reddy, P. Ultra-high vacuum scanning thermal microscopy for nanometer resolution quantitative thermometry. *ACS Nano* **6**, 4248-4257, (2012).
[265] Lee, W. *et al.* Heat dissipation in atomic-scale junctions. *Nature* **498**, 209-212, (2013).
[266] Altfeder, I., Voevodin, A. A. & Roy, A. K. Vacuum phonon tunneling. *Physical Review Letters* **105**, 166101, (2010).
[267] Singer, F., Ezzahri, Y. & Joulain, K. Near field radiative heat transfer between two nonlocal dielectrics. *Journal of Quantitative Spectroscopy and Radiative Transfer* **154**, 55-62, (2015).
[268] Chiloyan, V., Garg, J., Esfarjani, K. & Chen, G. Transition from near-field thermal radiation to phonon heat conduction at sub-nanometre gaps. *Nat. Commun.* **6**, (2015).
[269] Kim, K. *et al.* Quantification of thermal and contact resistances of scanning thermal probes. *Applied Physics Letters* **105**, 203107, (2014).
[270] Reid, M. T. H. & Johnson, S. G. Efficient computation of power, force and torque in BEM scattering calculations. *arXiv:1307.2966*, (2013).
[271] Madou, M. J. *Fundamentals of microfabrication and nanotechnology*. 3rd edn, Vol. II 299-303 (CRC Press, 2012).
[272] Hariharan, P. *Optical interferometry*. 2nd edn, (Academic Press, 2003).
[273] Sadat, S. *et al.* Room temperature picowatt-resolution calorimetry. *Applied Physics Letters* **99**, (2011).